Alma Mater Studiorum · Università di Bologna

School of Science
Department of Physics and Astronomy
Master Degree in Physics

# *Printed organic semiconductors for ionizing radiation detection*

**Supervisor:**

Prof. Beatrice Fraboni

**Submitted by:**

Alessandro Galeazzi

**Co-supervisors:**

Dr. Laura Basiricò

Dr. Ilaria Fratelli

Academic Year 2022/2023

# *Abstract*

In the last years, Organic Field-Effect Transistors (OFETs) have shown a great potential in the field of X-rays direct detection, thanks to the possibility of fabricating flexible devices with low toxicity and cost-effective deposition processes. In this thesis, the composition of the active layer of OFETs based on an organic small molecule (TMTES) blended with an insulating polymer (polystyrene) was studied as a function of the ratio between the two components, of the molecular weight of the polymer and considering the effects of the addition of a Parylene-C encapsulation layer. The study of the TMTES:PS ratio confirmed the results of previous works reported in literature for different materials that indicated a lower amount of polystyrene as preferable, while the analysis of the role of polystyrene molecular weight showed no significant impact caused by the variation of this parameter. On the other hand, the addition of an encapsulating layer was associated with a higher sensitivity ($S=(13.7\pm0.9)\cdot10^3\ \mu C\cdot Gy^{-1}cm^{-2}$) and with a tendency to retain the electrical parameters after electrical and radiative stress. These results open new possibilities to tune the features of blended materials as active layers of OFETs for ionizing radiation detection and to better understand the role and potential of the use of encapsulation layers in this kind of devices.

# *Contents*

# *Introduction*

The detection and measurement of ionizing radiation play a critical role in various fields, including industrial plants security, medical imaging, environmental monitoring and radiation-based therapies. Traditional ionizing radiation detectors rely on inorganic materials, such as silicon or germanium, exhibiting impressive performances. However, the emerging field of organic electronics has shown promising potential for ionizing radiation detection, thanks to electronic devices that employ organic semiconductors as their active material. These materials can be divided into small molecules and polymers, showing slightly different features that are particularly suitable for distinct applications. The main advantages of organic compounds are their mechanical flexibility, the possibility to cover large areas, the low toxicity and the fact that, being made mainly of carbon and hydrogen, they are human tissue equivalent. In addition, their X-ray sensitivities are becoming higher and higher, thanks to the huge efforts that researchers have been putting into the study of this new class of devices. Also, a common feature of organic-based transistors is their fabrication process, which is performed employing affordable deposition techniques requiring low temperatures and small amount of energy, compatible with polymeric and large area substrates. On the other hand, organic materials do show some drawbacks when compared to their inorganic counterparts: indeed, they are made of elements with low atomic number Z that provide a way lower stopping power with respect to silicon, germanium or Cadmium-Zinc-Telluride (CZT). This strongly hinders their quantum efficiency, so that various techniques have been investigated to improve their performances, among which it is worth mentioning the tuning of the photoconductive gain effect by tuning the morphology of the active layer and the transport properties of the devices. On the other hand, the use of blended active layers has been deeply investigated in recent years, since it allows to reach better electrical performances and to employ molecules that crystallize in molecular packings that produce high-mobility devices.

Besides, another important research line that has been investigated is the addition of an encapsulation on top of the active layer of electronic devices in order to prevent their degradation over time and provide better stability. The scope of this work is to study the impact of the variation of the blend composition both in the case of the small molecule:polymer ratio and in the case of the molecular weight of said polymer, and to evaluate the effects produced by the addition of a parylene-C encapsulation layer.

In the first chapter, the main X-ray sources are pointed out, together with the principal X-ray – matter interaction phenomena on which ionizing radiation detection is based. In section 1.3, a brief description of the main types of X-ray detectors is provided, with a particular focus on direct detectors and their figures of merit. Then, an analysis of the semiconductors used in the active layers of said detectors is presented, ranging from traditional inorganic ones to novel alternatives such as perovskites and hybrid compounds. Organic materials are discussed in detail in section 1.5, with a review of the state-of-the-art, a description of the photoconductive gain effect and of the deposition techniques of said organic materials.

The second chapter covers the topic of the organic field effect transistors (OFETs), from their main components and architectures (2.1) to their working principles and the analysis of their two operating regimes (2.2). In section 2.3, the figures of merit that are used to describe their performances will be discussed, together with the main techniques to extract them. Section 2.4 covers the main non-idealities that can be found in OFETs, together with their causes and possible solutions. Eventually, section 2.5 contains a short review of OFETs employed as ionizing radiation detection.

The third chapter describes, in its first two sections, the fabrication steps (3.1) of the devices studied in this thesis, with a particular emphasis on the deposition technique and on the organic compound that were employed (3.2). In section 3.3, we describe the encapsulation

layer material and deposition technique, while in section 3.4 the experimental setup for the electric and X.-ray characterizations are presented. In section 3.5, the main principle and experimental apparatus of the ToF-SIMS technique are depicted, and in section 3.6 the data analysis is described, with a reference to the steps that were used to perform the preprocessing of X-ray measurements and the scripts that provide the parameters of the characterizations.

In the last chapter of this work, all results are presented and discussed. In particular, in section 4.1, a global resume of the characterized sample with their parameters is provided, while section 4.2 and 4.3 discuss the result of the analyses of TMTES:PS ratio and PS molecular weight, respectively. In section 4.4, the outcomes of the ToF-SIMS analyses of the TMTES:PS blends are shown and discussed in light of the findings of this work, and in section 4.5 the results of the encapsulation layer study are described.

Finally, the conclusion of this thesis work summarizes previous results.

# Chapter 1:
# Ionizing Radiation Detection

Ionizing radiation is defined as the part of the electromagnetic spectrum that has enough energy to ionize atoms and molecules, causing the ejection of their electrons. The only parts of the electromagnetic radiation that possess sufficient energy to ionize matter are gamma rays, X-rays and extreme ultraviolet, although a clear threshold is not fixed since different elements have different ionization energies. In particular, X-rays (defined as the electromagnetic waves whose wavelengths are between 0.1Å and 10 Å) are employed in different applications, ranging from medical ones (diagnostics and radiotherapy) to industry and research activities: indeed, their wavelength is in the same order of magnitude of lattice spacings in crystals, so that it is possible to use X-rays to study materials properties. Anyway, every possible use of X-rays could not be employed without a device able to detect them, meaning that ionizing radiation detection plays a fundamental role in every existing X-ray application, and the development of the devices that can fulfill this task is crucial[1].

### *1.1. X-ray sources*

X-rays were discovered and initially employed due to the natural radioactivity of some heavy elements. A good example is barium, which is still used nowadays as a source of X-rays thanks to its decay process into Cesium ($^{133}Ba \rightarrow {}^{133}Cs$). However, the need for a better control of the radiation beam and for higher intensity led to new classes of devices, among which it is worth mentioning X-ray tubes and synchrotron radiation facilities.

X-ray tubes are the most widely used source of X-rays in ordinary applications, since they are a compact instrument that represents a good compromise between high intensity radiation and affordable requirements. It is possible to see a schematic representation of the main internal components of an X-ray tube in Fig. 1.

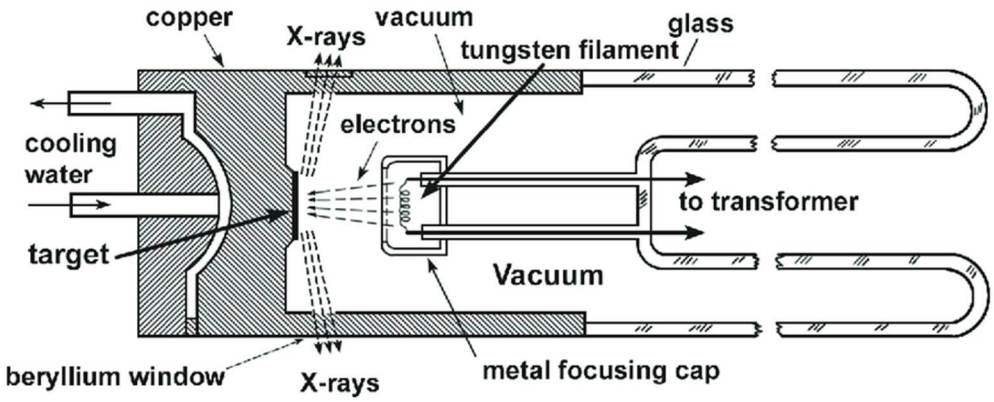


*Fig. 1: A scheme of the internal structure of an X-ray tube. In this case, the cooling system that avoids the overheating of the target employs water[2].*

The first step in the production of ionizing radiation in this kind of devices is the thermoionic emission of electrons from a filament heated by a current flow. As they are ejected from the filament, they get accelerated by a very high bias in the order of kV towards a target made of a specific material (e.g. Mo, W). Here, two different kinds of radiation are generated (Fig. 2).

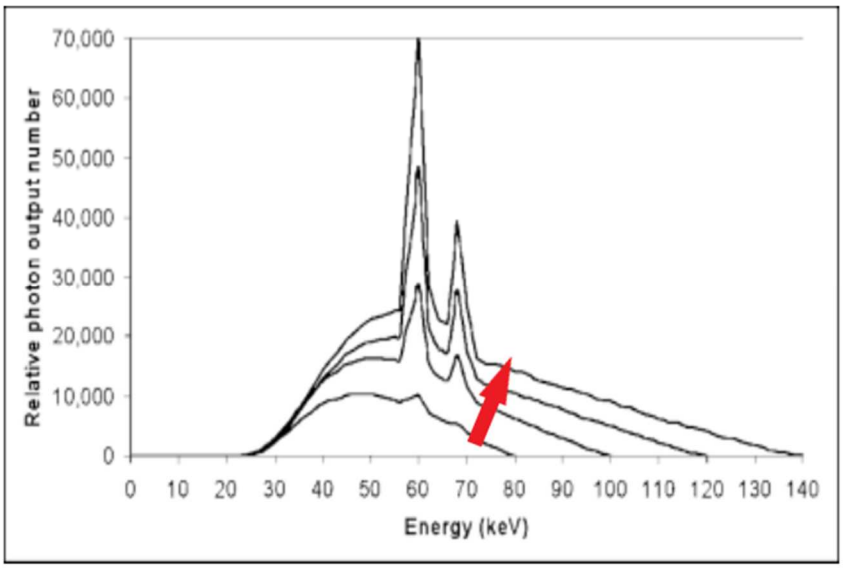


*Fig. 2: Example of output radiation from an X-ray tube. The peaks between 60keV and 70keV represent the two characteristic X-rays lines. The different lines refer to different tube voltages: it is possible to see that higher voltages (in the direction of the red arrow) increase the intensity of the radiation and shift the maximum energy to higher values*[3].

As electrons are decelerated by the Coulomb field of the target nuclei, they lose energy in form of ionizing radiation (named *Bremsstrahlung* radiation), producing a continuous spectrum up to a maximum energy that depends on the accelerating voltage. Just a fraction of the energy coming from the deceleration of electrons is transferred to radiation, and most of it will be converted into kinetic energy: this is the reason why an X-ray tube requires a cooling system that avoids the overheating of the target.

On the other hand, characteristic X-rays lines are produced in the target atoms when accelerated electrons hit the core electrons of the atoms: incoming electrons can eject core ones out of the atomic shells, leaving a hole behind. At this point, a cascade effect takes place, with a relaxation of electrons that occupy upper levels. This process involves the emission of X-ray photons at fixed and characteristic energy (which depends on the element that make up the target) and causes the intensity peaks that is always observed in the emission spectrum of X-ray tubes. Here, these two processes with very different origins are merged but they can still be easily distinguished since the radiation that they produce is very distinct. In general, this kind of instrument has important advantages as the low cost, the small size and the suitability for laboratory use. On the other hand, although the characteristic lines of the tube show a rather good intensity, this X-ray source offers a broad spectrum and the peak intensity is fixed to specific wavelengths. Besides, it has a poor intensity in the continuous spectrum.

In case a more intense radiation beam is needed, a larger X-ray facility (Fig. 3, higher image) is required able to produce the so-called “synchrotron radiation”. This kind of radiation is the result of the radial acceleration of charged particles (electrons) operated using magnetic fields. In these facilities, magnets are used in different configurations (from just bending magnets to more complicated ones, as wigglers and undulators) so that it is possible to tune the features of the radiation emitted. This kind of plant offers many advantages with respect to X-ray tubes, such as the possibility of concentrate the beam into a very narrow area and with a very high brightness (the number of photons flowing per unit of area and time). Another important difference with X-ray tubes is the possibility to tune the peak intensity of emitted radiation in a very wide range (up to high energy X-rays).

The use of synchrotron radiation facilities is becoming more and more popular in recent years, due to the need for higher and higher brightness and to the great capabilities of this structures (Fig. 3, lower image).

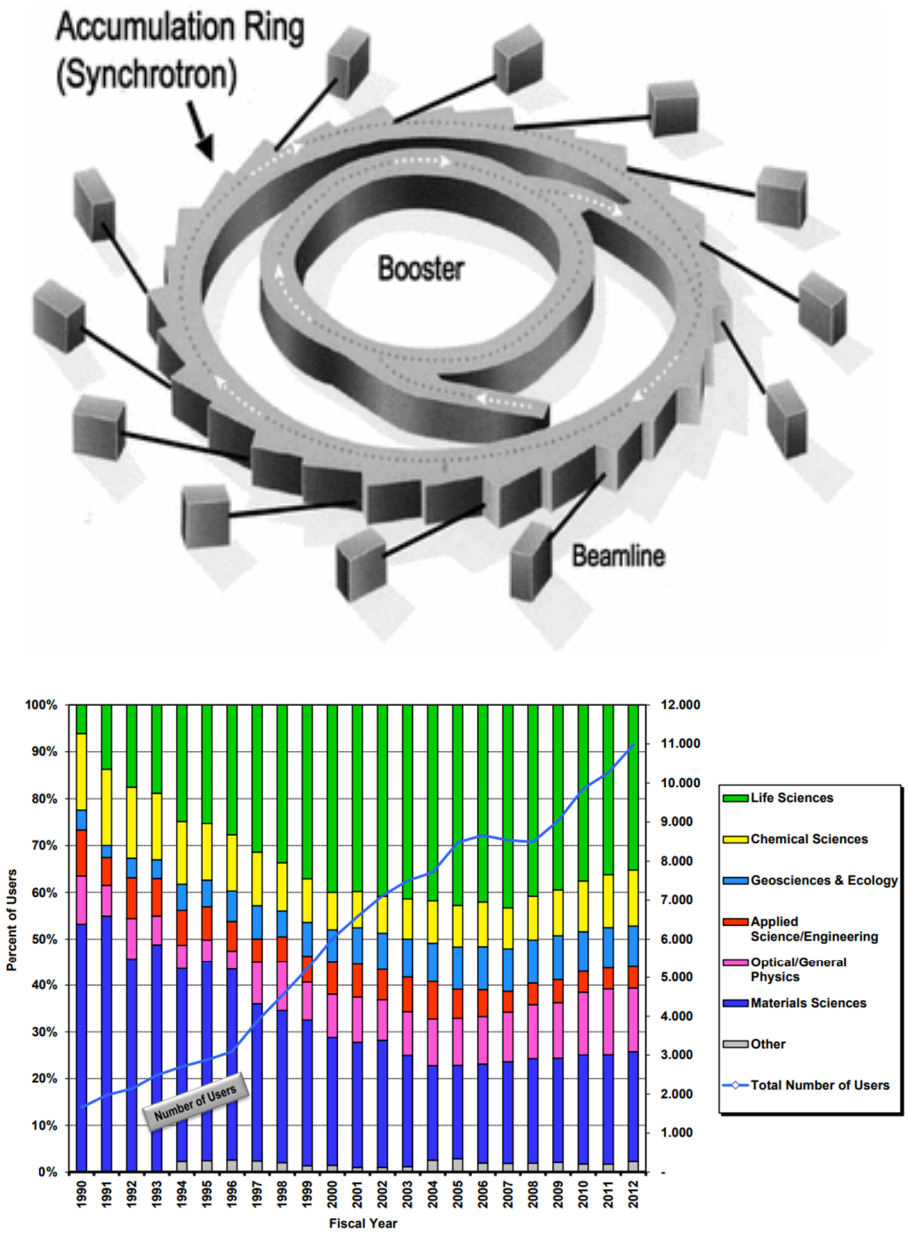


*Fig. 3: Scheme of a synchrotron radiation facility (upper image)[4] and number of users of synchrotron radiation facilities in the US and kind of application since 1990[5](lower image).*

### *1.2. X-ray – matter interaction*

The interaction between X-rays and matter can be explained considering three phenomena: photoelectric absorption, Compton scattering and electron-positron pair production. The importance of these three contributions depends on the atomic number of the absorbing material and on the energy of the impinging radiation (Fig. 4)[6].

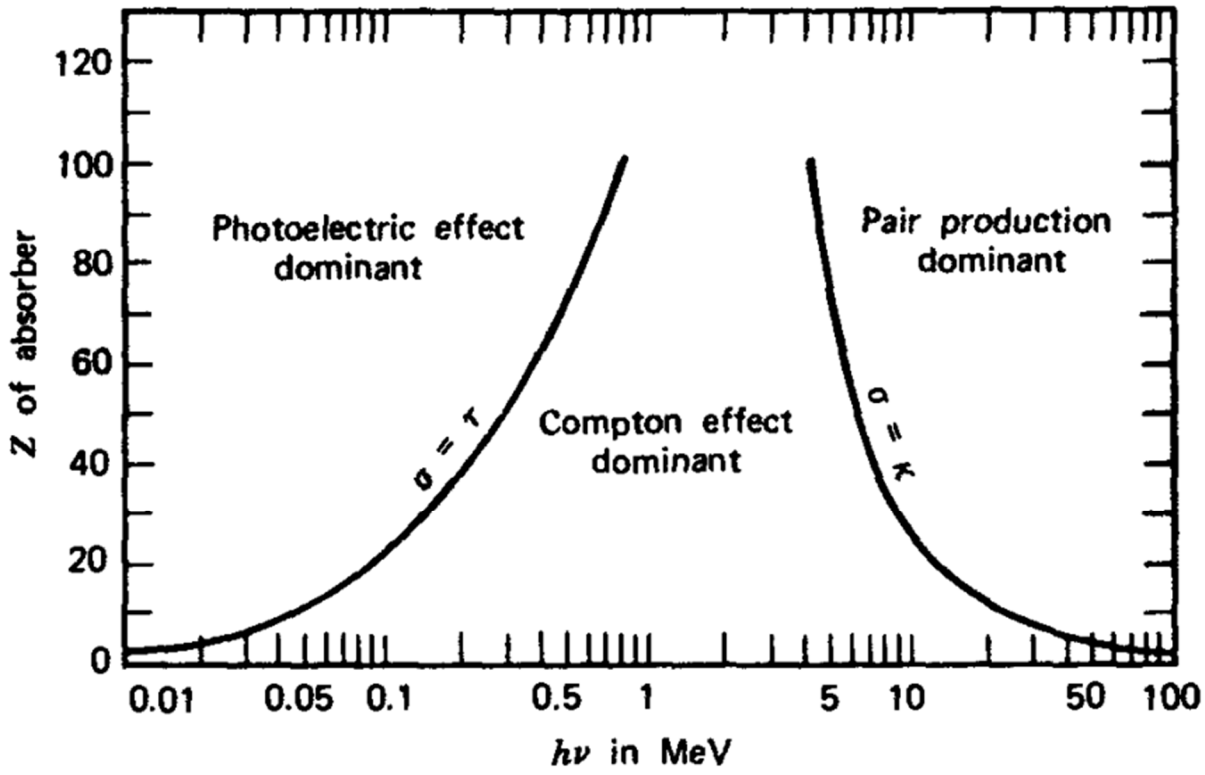


*Fig. 4: relative importance of the three main contributions to X-ray - matter interaction*[6].

- ***Photoelectric Absorption***

*Photoelectric effect* is the name given to the emission of electrons (in this case, called "photoelectrons") caused by the interaction between matter and incoming radiation. When the radiation is in the X-ray range, the energy of the photon is transferred to a core electron that gets ejected out of the atom, with an energy that depends on the frequency of the radiation and on the binding energy of the electron. As the core electron leaves the atom, a hole is left behind so that an electron from the higher shells will be able to jump down and occupy the state, with

the production of characteristic x-rays lines (as explained in the previous section) or the emission of an *Auger* electron. In general, the possibility to have this kind of interaction is determined by the energy of the incoming photon and by the atomic number of the atoms that are hit by radiation, so that higher Z and lower energies will result in a more significant probability of photoelectric absorption (Fig. 4).

- ***Compton Effect***

The Compton effect is an inelastic collision between the photons and the atoms forming the irradiated material. When a photon hits an electron, the former will be scattered losing part of its energy, that will be acquired by the latter in the form of kinetic energy (i.e. recoil electron). It is also possible to measure the angle θ considering the energy variation during the scattering event in terms of wavelength difference (Eq. 1):

$$\lambda_f - \lambda_i = \frac{h}{m_0 c}(1 - \cos\theta) \qquad [1]$$

Where $m_0$ is the rest mass of the electron. The probability of this process depends on the two quantities shown in Fig. 4 and is strongly dependent on the material the radiation interacts with, just like the other interaction phenomena.

- ***Pair production***

Pair production is the main interaction phenomenon at high energies (indeed, it is particular important for γ-rays), since in this case it is possible to find a minimum energy threshold under which this process cannot happen due to lack of energy: in fact, a photon needs to have two times the energy of an electron at rest in order to trigger the pair reaction. If this condition is satisfied, an electron and a positron can be generated in pair according to the laws of quantum electrodynamics (the explanation of which would go far beyond the purposes of this work). If

the incoming photon has more energy that the minimum needed for the formation of the pair, the excess will be transferred to the final particles as kinetic energy.

Since all these processes are present when radiation interacts with matter (Fig. 5), the total attenuation factor will be the sum of all contributions, namely (Eq. 2):

$$\mu_{tot} = \mu_{photo} + \mu_{Compton} + \mu_{pair} \quad [2]$$

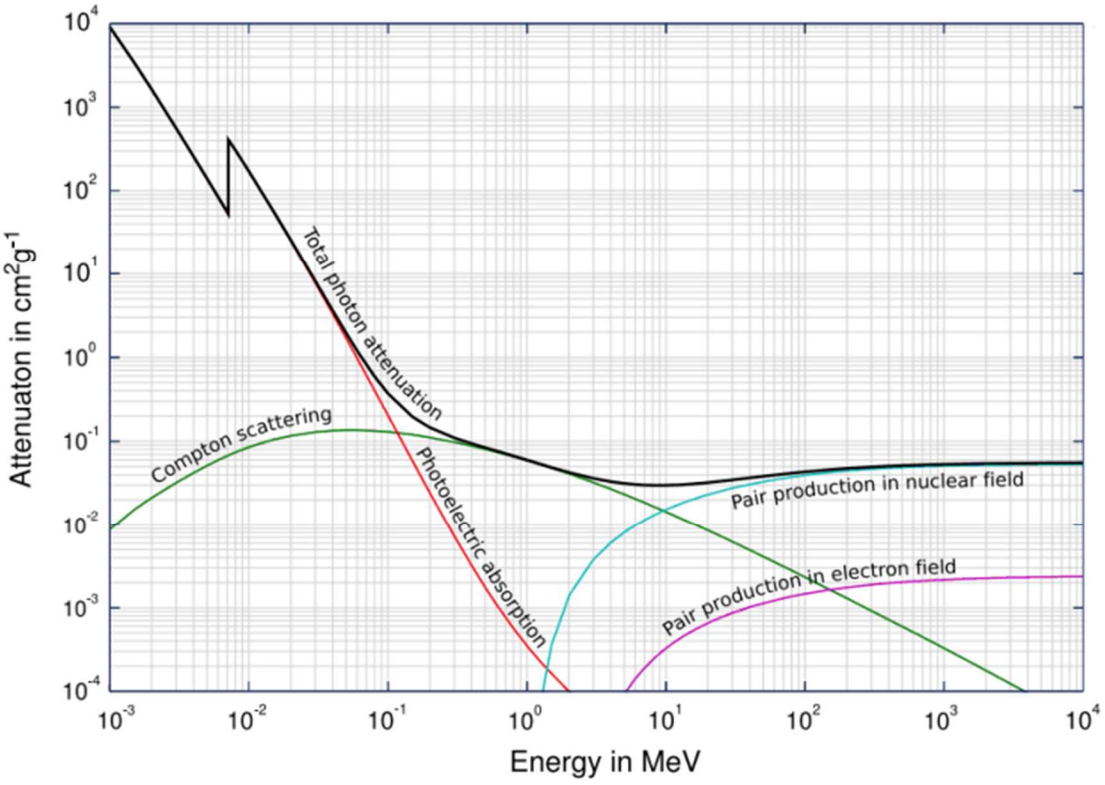


*Fig. 5: attenuation coefficient of every process and the total one as function of the impinging radiation energy[6].*

This $\mu_{tot}$ is particularly relevant since it controls the attenuation of the incident intensity as it penetrates the material, according to (Eq. 3):

$$I(z) = I_0 e^{-\mu z} \quad [3]$$

Where $I$ is the intensity at depth $z$, $I_0$ is the intensity of the radiation before the penetration into the medium and $z$ in the distance of a given point in the material from the surface.

### *1.3. X-ray detectors*

In general, a ionizing radiation detector collects high energy photons and converts them into an electric signal. In the case of X-rays, it is important to maximize the active volume of the device and the interaction between the material and the stimulus since this kind of radiation can deeply penetrate matter. These devices can operate in two distinct modes: in the "pulse mode", every single interaction can be detected, although a *dead time* must go by after the following signal can be measured by the detector. On the other hand, devices operating in "current mode" do not distinguish among individual signals but provide an electric signal proportional to the energy released by radiation by averaging all interactions. All possible X-rays detectors can be traced back to three different mediums where the absorption takes place: gasses (output: ions and electrons), scintillating materials (output: UV-visible photons) and semiconductors (output: electrons and holes). The working principles of gas-based detectors will not be discussed in detail in this work, since their features and applications are far from those that will be treated here. As a matter of fact, the next section will discuss the most relevant differences between detectors based on scintillation (*indirect*) and semiconductor-based ones (*direct* detectors).

### *1.3.1. Direct and indirect detectors*

In indirect detectors, X-rays are firstly converted into UV or visible radiation thanks to a "scintillator", and finally a photodetector converts this intermediate signal into an electrical one. On the other hand, a direct detector has an active material (generally a semiconductor) that absorbs bare ionizing radiation and produces an electric current as output[1] (Fig. 6).

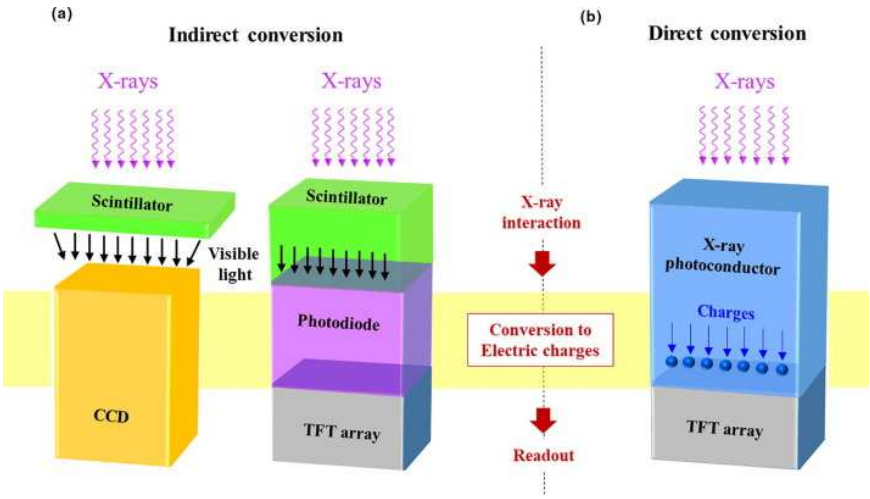


*Fig. 6: A graphical comparison between indirect and direct detection mechanisms for imaging application. In the first case, after the scintillation stage photons can be collected using different devices, as depicted here[7]. In other words, photodetectors are not the only option to be coupled to scintillators.*

In general, indirect devices have a more complex architecture and need an accurate coupling between two separate components. This can lead to losses and to self-absorption, so that direct detectors are often more suitable if we aim to detect ionizing radiation, as they possess useful features as a more compact structure and a better spatial resolution. Besides, considering the single-step conversion, direct detectors are typically faster than the indirect ones.

Direct detectors can be designed according to mainly three architectures, namely photoconductor, photodiode and phototransistor (Fig. 7). In the following, we will be focusing more in detail on the physical phenomena that are involved in the direct detection of X-rays.

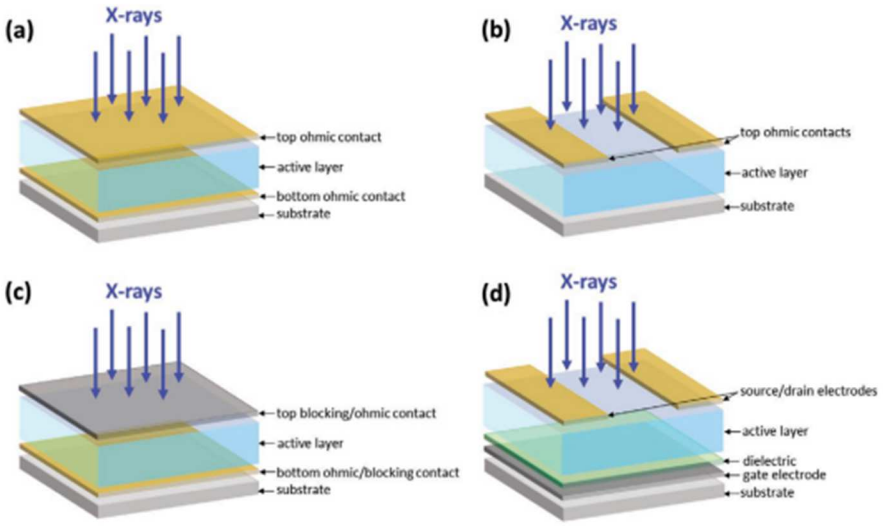


*Fig. 7: The three main architectures used in direct detectors. a) and b) are respectively the vertical and co-planar version of a photoconductor, while c) is a photodiode and d) is a phototransistor (the only 3-terminal device)*[1].

### *1.3.2. Direct detection mechanism*

When ionizing radiation impinges on a semiconductor layer, high-energy electrons will be generated and their energy will be released to nearby atoms, causing electron-holes pairs to be created together with phonons[6]. At this point, an electric field can be used to separate charge carriers and collect them at the electrodes, thus generating an electric signal as explained at the beginning of this section.

A simple equation can depict this process that produces the so-called *charge collection current* $I_{CC}$ (Eq. 4):

$$I_{CC} = \Phi n q \qquad [4]$$

Where $q$ is the elementary charge, $\Phi$ is the photon absorption rate, $n$ is the electron-hole pair generation rate per absorbed photon[8]. In many cases (especially for highly pure materials with low trap density), charge collection is the main phenomenon that permits the direct detection of ionizing radiation[1]. Nevertheless, in some materials we can observe an electric signal that overcomes the maximum nominal value of current generated from charge collection: this phenomenon is called “photoconductive gain”, and it can account for a major part of the output signal in those materials where trap states have a key role in transport properties[8]. An exhaustive explanation of this can be found in section 1.5.3.

### *1.3.3. Figures of merit*

In order to provide a quantitative description of X-ray detector performances, some *figures of merit* can be defined. For our purposes, we will focus mainly on the sensitivity since it is the most investigated figure of merit in this work. X-ray sensitivity (S) is defined as the charge collected Q per unit exposure of radiation X and unit area A. In other words, this quantity describes the ability of a detector to respond to a certain amount of radiation, normalizing the response to the area of the device[1]. Therefore, the sensitivity of a detector is determined by all the processed that play a role in the final output, starting from the collection of incoming radiation. From a theoretical point of view, we can write[9] (Eq. 5):

$$S_{th} = S_0 \eta_X \eta_m \eta_{CC} \quad [5]$$

Where $S_0$ is a normalization constant that depends only on the X-ray energy, and the η values are the efficiencies of the three main processes that make up the final sensitivity to X-rays. First, $\eta_X$ represents the quantum efficiency, namely the fraction of radiation that is absorbed by the active layer. It depends on the thickness of said layer and on the main properties of the material, as density and atomic composition. $\eta_m$ represents the efficiency of electron-hole pairs generation. This quantity is defined as the number of pairs created per absorbed photon. The last process that plays an important role is the charge transport and collection, which permits the measurement of the final electric output signal. The efficiency of this phenomenon is described by $\eta_{CC}$ and depends mainly on the mobility of the material in the active layer, on the driving force (the applied bias) and on the geometrical features of the device[1]. In conclusion, the final value of the detector sensitivity is the result of a huge number of contributions and processes, and a great variety of strategies and methods can be employed and studied to enhance this figure of merit.

Before introducing the operational definition of sensitivity, two physical quantities must be defined, namely the *absorbed dose* and the *dose rate* (*DR*). The former is defined as the energy deposited in matter by ionizing radiation per unit mass, and is measured in *Gray* (*Gy*), or Joule/kilogram. The latter represents the amount of radiation absorbed or delivered per unit time, and is measured in Gy/s.

At this point, if we are interested in the experimental evaluation of the performances of a detector, we can take advantage of the operative definition of sensitivity (Fig. 8), that is the linear dependence of the X-ray photocurrent signal $\Delta I = I_{Xray} - I_{dark}$ as a function of the impinging dose rate[1], often normalized by active area.

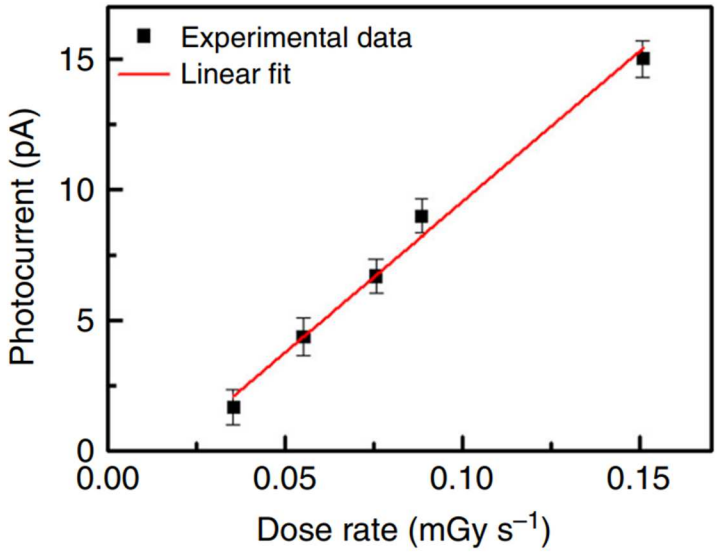


*Fig. 8: An example of sensitivity calculated from a linear fit according to its operative definition*[10].

Moreover, $I_{dark}$ is another important figure of merit of this kind of devices, called *dark current*: it is the current that can be measured as output of the device when no radiation is impinging. Its fluctuations are an important source of noise, so that it is important to keep it as low as possible, even if a precise threshold cannot be defined since it is strongly dependent on the application of every device and on the applied external bias. The main reason why a low $I_{dark}$ is desirable is that a low noise is essential to reach a high Signal-to-Noise Ratio (SNR), which represents a key parameter to assess the performance of a detector. For instance, another important figure of merit is the *Limit of Detection* (*LoD*), defined theoretically as the smallest signal that a device can clearly detect, and it can be operationally defined as the signal that produces a SNR equal to 3.

In conclusion, it is worth mentioning also the *response time*, which quantifies the speed of the detector (how fast an output signal can be generated after the stimulus is given).

### *1.4. Semiconductors for X-ray detection*

As discussed before, X-rays solid-state direct detectors rely on active layers made of semiconductors, so that it is crucial to analyze this component in detail. Historically, the first detectors designed for these purposes were based on silicon and germanium[6]. Nowadays, these materials still find application in the detection of other stimuli, such as high-energy radiation (Ge-based detectors are used for γ-rays) and particles (mainly Si), but they have been completely outperformed by more recent compounds, among which it is worth mentioning Cadmium Zinc Telluride (CZT)[11], which has reached unprecedented performances and represents the state-of-the-art for direct solid state X-rays detectors. In recent years, other classes of materials were developed in order to widen the spectrum of applications of this kind of devices, such as perovskites, organic and organic-inorganic active layer (*hybrid* semiconductors), for which a description will be provided later.

#### *1.4.1. Inorganic semiconductors*

The main reason why inorganic semiconductors have been the most obvious choice from the beginning and were the first to be employed for X-rays detection lies in their excellent transport properties. For instance, inorganic semiconductor single crystals present a very high degree of order and it is possible to apply metallurgical processes to reduce or control the number of their impurities or defects. Therefore, their charge transport properties can be pushed to high levels and their mobilities can reach values close to 1000 $cm^2/Vs$ [12]. Also, since the elements that are used for the active layer tend to have very high atomic numbers, they possess a very high stopping power and are particularly suitable for dosimetry. Considering all the previous aspects, it is possible to build devices with excellent sensitivity: this is the main aspect for which this kind of detector has impressive performances, together with a typically short response time, particularly required for medical applications such as imaging and mammographies[13].

On the other hand, this kind of devices suffer from some limitations, such as the difficulty to grow large-size crystals and at an affordable cost, their intrinsic rigidness and, in some cases, the presence of toxic elements like cadmium. To overcome these main limitations, in recent years scientists have explored other materials able to fulfill important emergent requirements such as the mechanical flexibility and the large area.

### *1.4.1. New alternatives: Perovskites and hybrid semiconductors*

A very promising class of materials is represented by perovskites: these compounds share a common crystal structure (Fig. 9a) that was firstly identified in $CaTiO_3$.

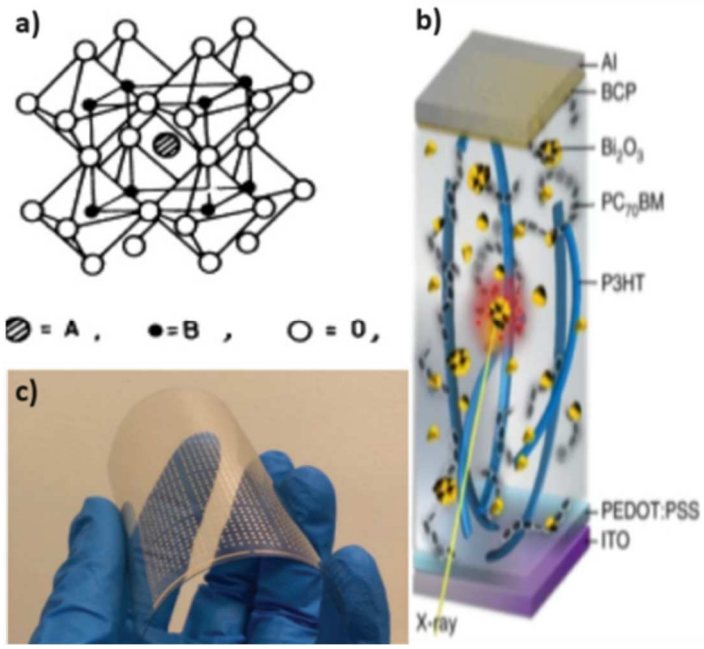


*Fig. 9: a) the $ABO_3$ structure of perovskite[14]. In the case of $CaTiO_3$, A is Ca, B is Ti. b) an example of hybrid material used as active layer of a detector[15]. c) a flexible device based on a perovskite ($CsPbBr_3$)[16].*

In particular, research interest for perovskite arose in the field of solar cells and LEDs first, as they have shown great capabilities as highly efficient materials[17]. In the case of photovoltaic applications, they became the principal competitor of silicon-based traditional cells thanks to a great absorption of solar light and different precursory materials.

Perovskites were first employed in the active layer of an X-ray detector in 2013 in the form of single crystal[18] and in 2015 as a thin-film detector[19], and they have been showing great potential due to their good transport properties and high stopping power, coming from the high atomic number of their constituents (Fig. 9c). On the other hand, some drawbacks have not been faced yet, since perovskite are still prone to degradation when exposed to air and water and lead-halide ones, although showing excellent performances, employ toxic materials that hinder their potential for several applications such as medical ones[1].

Finally, organic materials are another important alternative to traditional inorganic active layers and to perovskites as they show those features that cannot be offered by other compounds, such as tissue equivalence, low toxicity and environmental compatibility in their production processes. Full organic active layer will be investigated in detail in the next section, but it is worth mentioning the existence of organic-inorganic blends (so-called *hybrid* materials), that have been investigated as a possible solution to limit the main disadvantage of organic material, namely their low stopping power: indeed, organic molecules and polymers are made of carbon and hydrogen, which implies a very low atomic number and an intrinsic low charge collection current. A possible solution to increase Z in organic materials is the addition of high-Z molecules such as $Bi_2O_3$ nanoparticles (Fig. 9b)[20], as this can improve the final stopping power of the blend. However, this solution presents other issues, such as the loss of tissue equivalence for high concentrations of nanoparticles and the possibility of aggregation and formation of clusters that degrade the electric properties of the film, so that some constrains exist in the addition of this kind of blended materials.

## *1.5. Organic semiconductors for X-ray detection*

In the last decades, the field of organic electronics has become one of the most important research areas of materials science, and its results have had major implications in a wide variety of devices, ranging from organic LEDs (OLEDs)[21] to flexible photovoltaics[22] and sensors[23]. Also X-rays detectors could take advantage of the rise of this new class of materials, in order to satisfy the requirements coming from emerging applications.

### *1.5.1. Main features and comparison with inorganic semiconductor-based devices*

The success of organic semiconductors is due to their peculiar features, since these materials show low fabrication costs, simple production processes and compatibility with flexible substrates and large-area devices. As more and more researchers started studying organic active layers for detection applications, their performances became better and better, up to reach and overcome those of traditional inorganic polycrystalline and amorphous compounds employed for large-area applications (Fig. 10)[24].

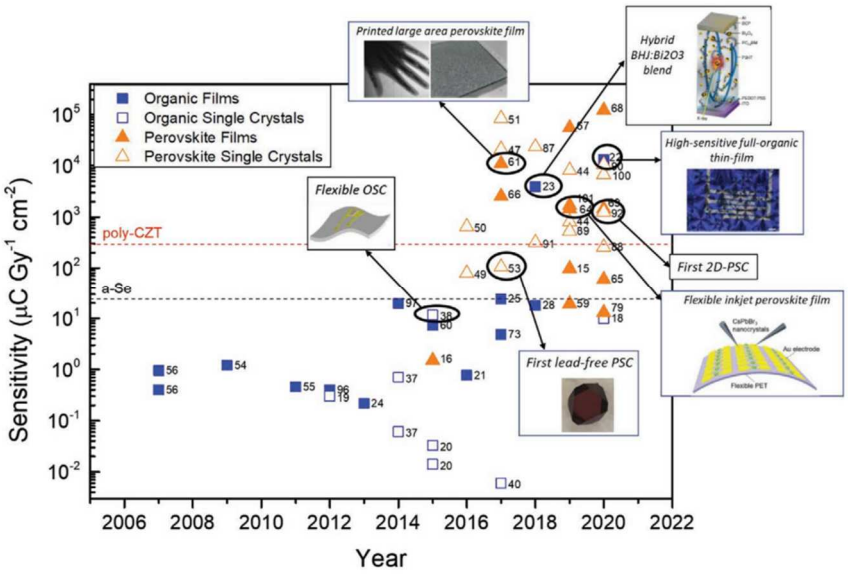


*Fig. 10: Timeline of X-ray detector development in terms of sensitivity[1]. In recent years, organic films reached sensitivity values comparable with some inorganic materials, such as a-Se (One of the main inorganic-based competitor for large-area direct radiation detection).*

The semiconducting materials used for these devices are composed of small molecules or polymers, and they possess unique electronic properties that make them suitable for various applications. In the context of ionizing radiation detection, organic materials offer major advantages over their inorganic counterparts. One of the key advantages of employing organic materials in devices for ionizing radiation detection is their mechanical flexibility, that together with their low toxicity make them ideal for medical applications. Additionally, the fabrication processes of devices based on organic materials are relatively simple and cost-effective, making them an attractive option for large-scale production and for scalability onto large areas, as well as compatible with printing production techniques and with the goals of the green transition.

While organic materials offer numerous advantages, they do present some challenges when compared to the inorganic films that are traditionally employed in direct radiation detectors. The main intrinsic disadvantage is their low atomic number Z, a consequence of their composition made essentially of carbon and hydrogen atoms: this leads to a poor absorption of high energy photons, which strongly limits their external quantum efficiency[25]. Various techniques have been investigated in order to mitigate this drawback, among which we have already discussed the addition of high-Z nanoparticles to increase the radiation absorption of the devices. Another meaningful strategy is the tuning of the photoconductive gain effect, a peculiar phenomenon caused by trap states that produces an amplification of the current generated during X-rays exposure, which will be discussed in the following.

### *1.5.2. Organic semiconductors for X-ray detection: State-of-the-art*

Research in organic semiconductors for ionizing radiation detection follows mainly two paths: organic single crystals and polycrystalline thin film devices. The former are valid candidates for the employment in detectors since they show long-range molecular packing order, lack of grain boundaries and high electrical mobility (in the order of 10 $cm^2/Vs$). Also, their dark current is remarkably low and allow an effective charge collection at electrodes. One of the most interesting aspects about single crystals is the fact that their detection performance seems to be independent on the mobility[26]. Although the best results have been obtained using high applied voltages and thick crystals that hinder those devices from being flexible[1], in recent years the possibility of building low-voltage and bendable detectors using organic single crystals was proved[27], enlarging the potential of this kind of active layers for X-ray detection.

On the other hand, devices based on organic polycrystalline thin films have shown great potential from the very beginning, due to their excellent compatibility with solution-based deposition techniques that are suitable for large-area detectors with low-cost production and complexity. In order to reach better performances, different strategies have been studied: a very simple and obvious solution to achieve better sensitivities is the use of thicker active layers that can produce more free charges and thus a higher response, but a heavy drawback has to be considered, since this will impact negatively on the mechanical flexibility of the device. Similarly, the addition of high-Z nanoparticles has already been cited and offers good results, but has relevant limitations linked to the concentration of said nanoparticles that cannot be overcome easily[20]. Therefore, other strategies were developed, such as a better understanding of the photoconductive gain effect (more in detail in the next section) and the optimization of the transport properties and collection efficiency by the blending with other organic compounds[1].

A meaningful result was reached in 2020 by Temiño et al.[10], who built an ultrahigh sensitivity detector employing an organic thin film blend of TIPS-pentacene and Polystyrene (PS) and showed that the addition of Polystyrene to the TIPS-pentacene thin film had a powerful effect on both mobility and X-ray sensitivity (Fig. 11).

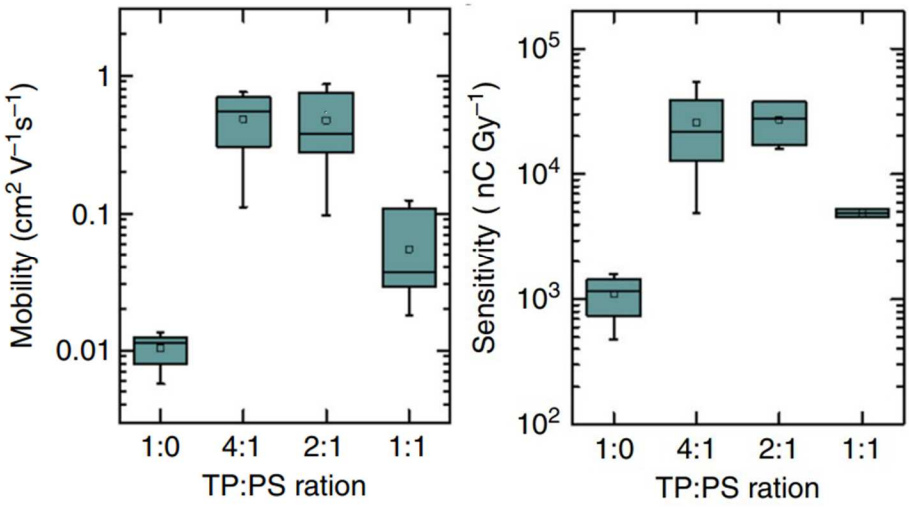


*Fig. 11: Box-plot statistics for mobility and sensitivity of OFET based on blends of TIPS-pentacene and Polystyrene with different ratios. It is possible to see how the presence of Polystyrene strongly enhances both parameters*[10].

Moreover, thin films allow the use of meniscus-shearing techniques by which it is possible to control the morphology of the final active layer, which plays a major role in the final performance of the detector[28].

### *1.5.3. Photoconductive gain*

In the case of organic semiconductors, the *charge collection current* $I_{CC}$ that was introduced with Eq. 4 does not represent the main part of the current that can be measured by X-ray detectors in the case of inorganic active layers: indeed, it is possible to show[8] that for organic materials the theoretical calculated $I_{CC}$ strongly underestimates the actually measured signal by orders of magnitude.

The process that accounts for this wide discrepancy is called "photoconductive gain" (PG) and represents the main reason why organic semiconductors can reach high sensitivity values despite having a low stopping power with respect to inorganic materials. The amplification G given by photoconductive gain can be written as (Eq. 6):

$$\Delta I_{PG} = G I_{CC} \quad [6]$$

Where $\Delta I_{PG}$ represents the amplificated current signal that is measured when the detector is irradiated, and $I_{CC}$ is the current generated by charge collection.

To explain this peculiar effect and the typical saw-tooth shape of the photocurrent in organic materials detectors (Fig. 12), a "kinetic model" was proposed in 2016[8], focusing on the increase in carrier concentration caused by impinging X-rays.

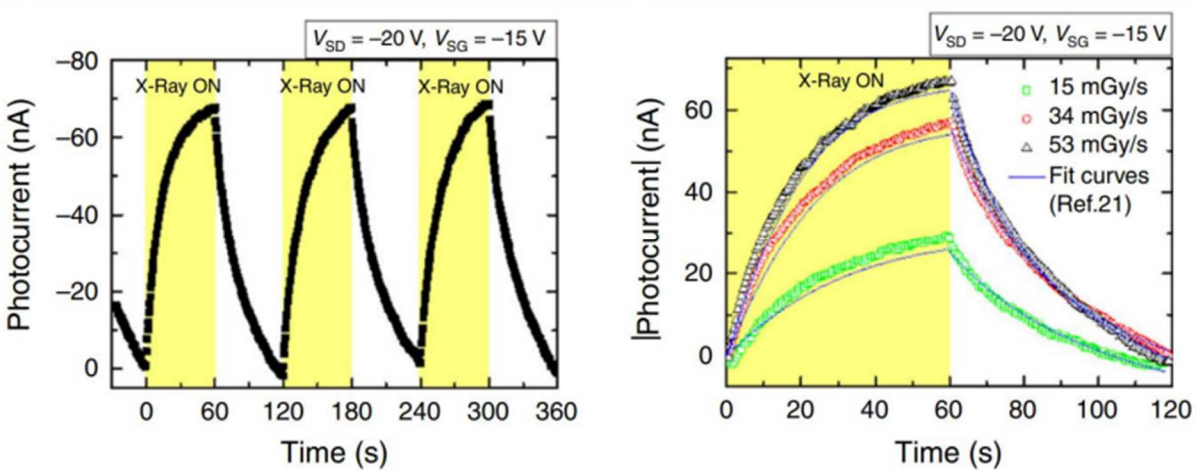


*Fig. 12: Saw-tooth shape of photocurrent upon three switch on-off cycles (left) and fit on curves with different X-ray dose rate to find the phenomenological parameters of the kinetic model (right)*[10].

In organic materials, holes and electrons have different transport properties, since for most of them (e.g. TIPS-pentacene) the former (i.e. majority carriers) tends to reach high mobility values while the latter (i.e. minority carriers) get easily trapped in ambient conditions (in presence of oxygen). In this situation, when these materials are irradiated and electron-hole pairs are created, holes drift towards the collecting electrode due to the applied potential difference, while some electrons will fill trap states.

As charge neutrality must be maintained, trapped electrons will be constantly counterbalanced by holes injection at the opposite electrode, meaning that every electron-hole pair created by high energy photons will produce more than just one free charge carrier, resulting in again inner amplification mechanism (Fig. 13).

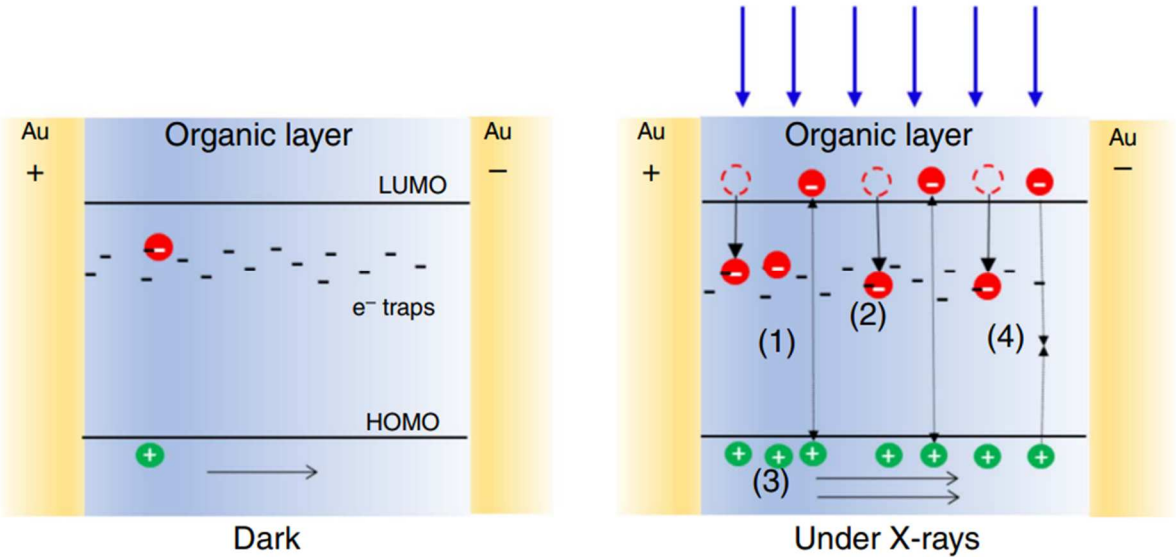


*Fig. 13: Organic material detection mechanism: in dark conditions, only intrinsic carriers contribute to current (so-called "dark current"), while under X-rays additional charge carriers are generated. Holes drift towards the negative biased electrode, while electrons get stuck in trap states*[8].

In this model, the photoconductive gain G will be equal to the ratio between two different characteristic times, accounting for the two main aspects of transport properties of the material: recombination time $\tau_r$ and transit time $\tau_t$. The first term describes electron recombination time and can be written using a phenomenological equation (Eq. 7):

$$\tau_r(\rho_x) = \frac{\alpha}{\gamma}\left[\alpha \ln\left(\frac{\rho_0}{\rho_x}\right)\right]^{\frac{1-\gamma}{\gamma}} \qquad [7]$$

Where $\alpha$, $\gamma$ and $\rho_0$ are material-related parameters that can be extracted from dynamic curves after X-ray irradiation, as shown in Fig. 12 (right). They describe the trap states ($\alpha$ and $\gamma$) and the reference carrier density ($\rho_0$) of the material.

On the other hand, the transit time $\tau_t$ represents the time that charges need to reach the electrode and be collected, producing a current. It can be calculated as shown in Eq. 8:

$$\tau_t = \frac{L^2}{\mu V} \quad [8]$$

Where $L$, $\mu$ and $V$ represent the channel length, the electrical mobility and the applied bias, respectively.

As it is possible to see from these equations, the control of charge transport properties is crucial to fully exploit the photoconductive gain. Indeed, this is one of the main pathways that have been investigated in recent years, and deposition techniques that allow a better control over the quality of the organic film have received more and more attention. Among them, it is worth mentioning Bar-Assisted Meniscus Shearing (BAMS): this technique has been successfully employed to fabricate organic X-ray detectors with record sensitivity in 2022[28] (Fig. 14) thanks to the possibility of controlling the grain size and grain boundaries, which are directly connected to the density of trap states for electrons. This plays a key role to enhance the sensitivity of this kind of detectors, as the kinetic model showed with the concept of photoconductive gain.

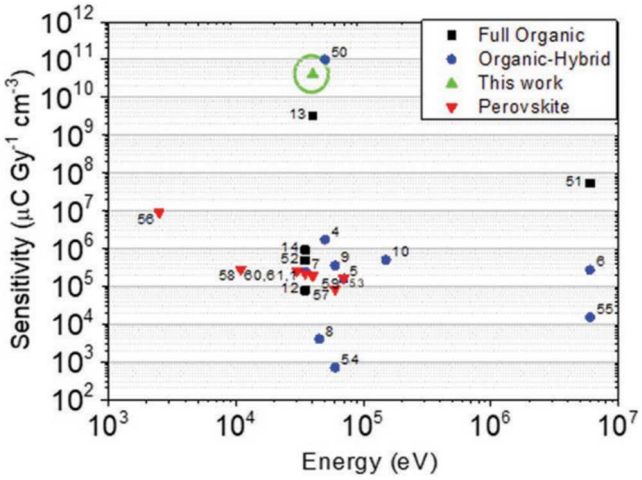


*Fig. 14: Comparison of the sensitivities per unit volume between TMTES:PS-based OFET deposited with BAMS and other state-of-the-art thin-film detectors[28].*

### *1.5.4. Organic semiconductors deposition techniques*

One of the crucial steps in the fabrication of ionizing radiation detectors based on organic materials is the deposition of the semiconductor layer, since it represents the active material of the device, and a careful and well-controlled film deposition has a major role in the final performances of the detector. In recent years, devices based on thin films of organic semiconductors grown from solution have shown higher and higher performances, so that many solution-based techniques were developed in order to achieve a better control over film morphology and alignment of crystals in the polycrystalline thin films[29]. This section will provide a quick description of the main procedures that are being developed to improve this very important step of the fabrication of organic semiconductor-based devices (Fig. 15), with a particular emphasis on solution shearing techniques, since they have been deeply studied for the development of devices easily scalable onto flexible and large areas.

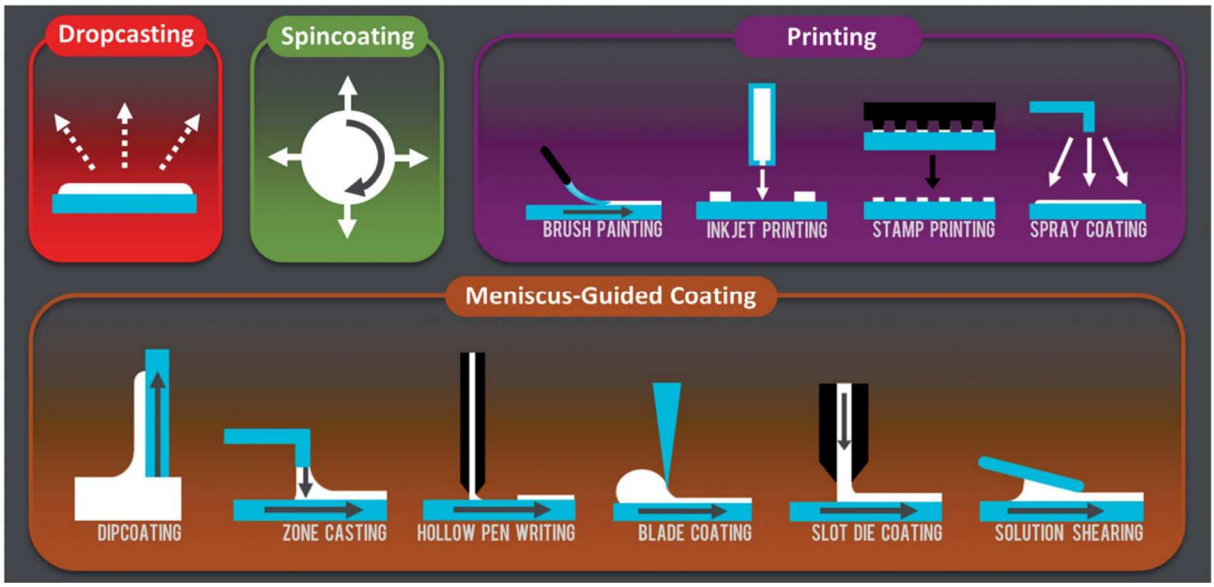


*Fig. 15: Summary of solution-based techniques used to deposit organic semiconductor thin films[29].*

- ***Dropcasting and spincoating***

Dropcasting is a simple technique that is performed casting an organic semiconductor solution to let it evaporate, producing a thin film or a single crystal (mainly in the case of self-organizing materials). More sophisticated methods have been studied to better control the deposited layer, working on the atmosphere of the deposition chamber, on the solvent composition or employing sound waves[29]. On the other hand, spincoating uses a rotating surface where the solution is dropped, in order to achieve a thin layer thanks to the centrifugal force exerted on the solution drop. This method is exploited in many ways, but the main parameters that are varied to control the final films are accelerating and decelerating rates of the rotating substrate, the angular speed, the time of spinning and the position of the solution drop[30].

- ***Printing***

Printing methods cover a wide variety of very different procedures: here we will just focus on inkjet printing, since it is one of those techniques that meet the need for flexibility and large area scalability required by the detectors that we are considering, and it is one of the most common techniques for the deposition of organic semiconductors. It involves the deposition of a jet of ink in form of small droplets onto a substrate where they evaporate, and it is primarily controlled by tuning the viscosity of the solution and the ink-substrate interaction[30]. Another printing technique of interest, similar to inkjet printing, is spray coating: in this case, droplets are formed by aerosolization with an inert gas so that they coat the substrate, and the key parameters to control the process include also the atomizing gas pressure and the spray nozzle features[29]. In general, these techniques can be further developed into more complex systems, in order to meet harder requirements such as the deposition of multiple organic semiconductor layers.

- ***Meniscus-Guided coating***

These techniques involve the linear translation of either the substrate or the coating tool to induce aligned growth of crystals in the deposited thin films, and a key role is played by the evolution of the solution meniscus, acting as an air-liquid interface for solvent evaporation[29]. Different ways of approaching this concept have been developed, as it is possible to see in Fig. 14, but one of them is particularly meaningful for the purposes of this report, namely solution shearing: in this method, a shearing blade or bar is moved on a hot-plate substrate (at a certain controlled temperature) containing an organic semiconductor solution. The shearing tool moves on the substrate at a fixed speed, so that the solvent on the coated surface can evaporate and consequently a thin film is formed[30]. A specific variety of this technique, called BAMS (Bar-Assisted Meniscus Shearing, Fig. 16) was proven to be particularly suitable to produce very performant organic field-effect transistors (OFETs), since it allows to control and tune the morphology of the polycrystalline semiconductor thin films.

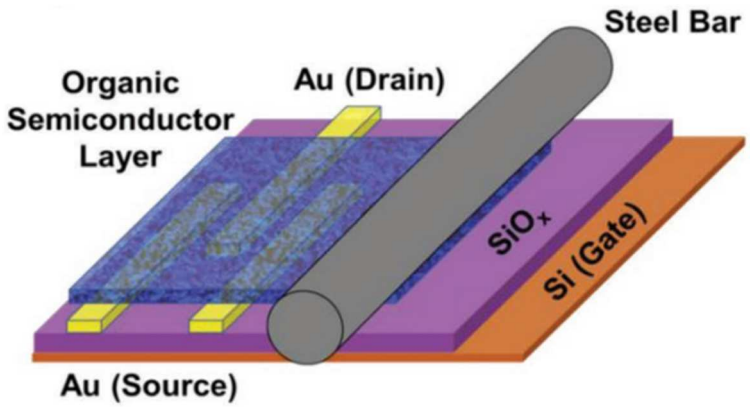


*Fig. 16: Scheme of the deposition of the semiconductor layer of an OFET using bar-assisted meniscus shearing*[28].

Notably, it is possible to vary the electrical properties and the final structure of the thin film acting on the substrate temperature and the coating speed (the velocity of the bar movement above the substrate)[31].

# *Chapter 2:*
# *Organic Field-Effect Transistors (OFETs)*

Generally speaking, Field-Effect Transistors (FETs) are three-terminal devices where it is possible to control the flow of current between the source and drain electrodes by acting on the conductivity of the channel thanks to a contact called *gate.* When the conducting channel is made of an organic semiconductor, this kind of device is called *Organic* Field-Effect Transistor (OFET). The use of an organic material as active layer of the device offers various advantages, such as the possibility to have flexible devices because of the low-temperature processes and to employ low-cost deposition techniques for their fabrication. OFETs are also a promising device architecture for X-rays direct detectors, since they allow the tuning of the main electric features of the conducting channel, which permits to have a better control of the final performance of the detector.

## *2.1 Architectures and geometries*

OFETs can be fabricated using four geometries, in which the main components of the device are placed in different ways according to the order of their deposition. The architecture of the device has an impact on its performance, so that the final purpose should be taken into account before organizing the deposition steps, together with the features of the active material and the possible addition of an encapsulation layer to improve the device stability over time.

### *2.1.1 Main components*

An OFET is made of three contacts (namely, *gate*, *source* and *drain*) and multiple layers, whose composition depend on the function that they have in the device: the organic semiconductor (where the conductive channel between source and drain is present or created), the dielectric layer (which can be made of both organic and inorganic material) and a substrate on which electrodes and layers are deposited. All the previously mentioned components are always present, but they are placed in different positions in the device, according to the geometry that is chosen for the specific purpose of the transistors (Fig. 17).

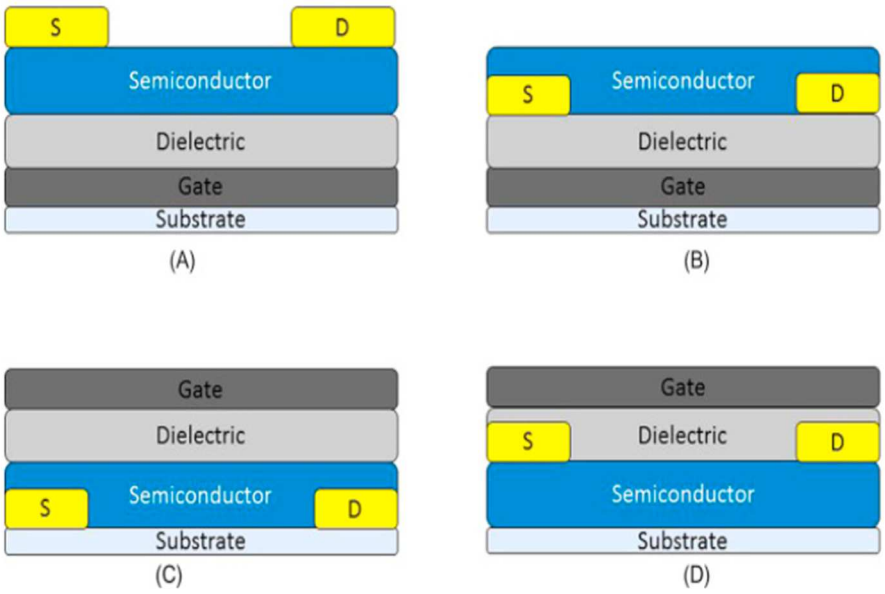


*Fig. 17: The four geometries that can be used in OFETs. (A) bottom gate, top contacts, (B) bottom gate, bottom contacts, (C) top gate, bottom contacts, and (D) top gate, top contacts*[32].

These four configurations can be split into two groups, namely coplanar (BGBC and TGTC, namely bottom gate bottom contacts and top gate top contacts, respectively) and staggered (BGTC and TGBC, namely bottom gate top contacts and top gate bottom contacts, respectively). Every configuration shows some advantages and disadvantages, and the chosen one should be determined by the final application of the device. For example, the BGBC structure is particularly suitable for the study of the semiconductor material and the deposition processes, since in that case the dielectric layer and the three contacts are prefabricated, while the semiconductor deposition is the very last step. This also allows to have a pristine semiconductor-dielectric interface, since no additional process is required after the semiconductor has been deposited. Nevertheless, this configuration is particularly vulnerable to those ambient conditions that speed up the degradation of the device, such as the interaction with air and humidity. On the other hand, the architectures that possess a top-gate terminal, namely TGBC and TGTC, reduce environmental degradation, since the dielectric acts as an encapsulation layer as well[30].

### *2.1.2 Enhancement and depletion transistors*

When a transistor is switched on, an electric current flows through the conductive channel between the source and drain contacts. Depending on the doping of the semiconductor, charge majority carriers can be holes (p-type) or electrons (n-type). In both cases, it is possible to distinguish between depletion and enhancement types, corresponding to the state of the transistor (off and on, respectively) when the gate-source voltage is zero (Fig. 18).

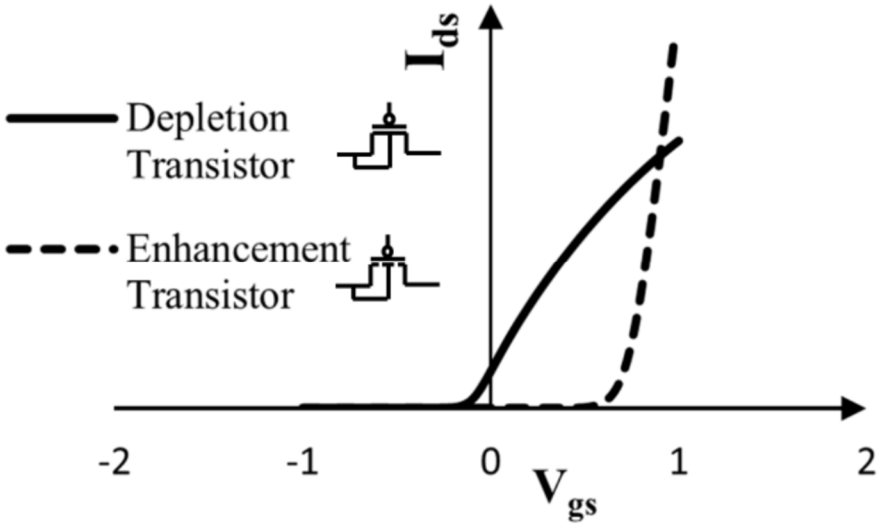


*Fig. 18: Depletion and enhancement types I-V characteristics. It is possible to see that in depletion mode, current flows between source and drain even if no voltage is applied to gate*[33].

In other words, in a depletion mode transistor an n-channel (or p-channel) region exists between the source and the drain electrodes even with 0 V applied to the gate. Conversely, in an enhancement mode n-channel (p-channel) transistor, the semiconductor material close to the interface with the dielectric is not inverted directly with zero gate voltage. A positive (negative) gate voltage induces an n-type (p-type) inversion layer, which then connects the n-type (p-type) source and the n-type (p-type) drain regions and allows the current to flow ($I_{SD}$ will be negative for p-doped semiconductor and positive for n-doped ones)[34].

This difference has an impact on the main equations that describe the drain current as a function of the applied voltages, since the threshold voltage $V_T$ of the device (for its definition, see section 2.2) is negative for (p-channel) enhancement transistors and positive for depletion transistors. Since organic semiconductors are mostly p-doped, in the following we will be implying that we are considering p-channel transistors, unless differently specified.

### *2.1.3 Role of encapsulation*

The use of an encapsulation layer on top of the semiconductor is particularly required in those cases where the conditions in which transistors operate induce a relevant degradation that can worsen their performances over time. A meaningful example is the one of perovskites-based solar cells, for which a lot of effort has been put in the study of proper encapsulating materials that could preserve them from the penetration of oxygen and water through the active layer, in order to retain their efficiency over time[35]. However, even if encapsulation can strongly improve the stability of OFETs, the addition of a layer (and therefore, of an interface) can also impact the transport properties of the organic active material, leading to worse transport properties[36]. These effects can be due to both interfacial and bulk effect produced by the encapsulation, so that its thickness plays a major role in the variation of the electric parameters of the device. Several compounds have been studied to be used as encapsulating materials, such as silicon oxides ($SiO_x$) and aluminum oxides ($AlO_x$), but also a wide variety of organic polymers and molecules[37].

### *2.2 OFETs working principles*

OFETs can be operated acting on gate and drain potentials ($V_{SG}$ and $V_{SD}$) once the source electrode has been grounded and taken as the reference for them. For an ideal device, when the gate voltage is set at 0 V, no charge accumulation is present at the semiconductor-dielectric interface and the device is turned off. Conversely, when $V_{SG}$ is applied, the dielectric gets polarized and charges accumulate at the interface, so that the device is turned on: at this point, if $V_{SD}$ is applied, charges will be collected and current will flow through the conductive channel (drain current, $I_D$). In other words, $V_{SG}$ controls the charge density (and therefore the magnitude of the drain current) applying an electric field that forces the charges at the semiconductor-dielectric interface, from which the term "field-effect" comes from. Anyway, in a real device it is crucial to remember that an initial $V_{SG}$ is often needed in order to occupy possibly existent trap states at the interface before charge accumulation can take place. This additional potential that we need to provide before seeing a rise in the current is called *threshold voltage* ($V_{Th}$), and it is a figure of merit that accounts for many non-idealities in the device, such as crystal defects, impurities and trap states. This quantity can be both positive and negative, as already discussed in section 2.1.2., so that it can happen that a positive $V_{SG}$ must be applied to switch off the device[30].

If we plot the drain current as function of $V_{SD}$ for different values of $V_{SG}$, we get the so-called *output characteristic* (Fig. 19a): this plot is particularly meaningful to understand the two regimes where an OFET can work.

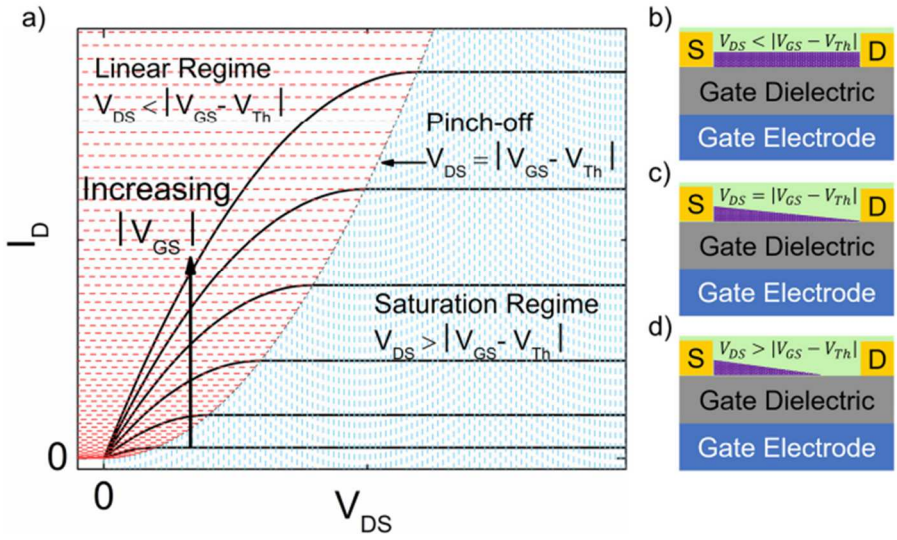


*Fig. 19: Linear and saturation regimes, and their effect on the conductive channel (in purple) charge density. a) Ideal OFET output characteristics, (b) linear regime, (c) pinch-off, (d) saturation regime.*

### *2.2.1 Linear regime*

The linear regime is the part of the output characteristic where $V_{SD} < |V_{SG} - V_{Th}|$. In this region (Fig. 19b), the drain current increases linearly with $V_{SD}$ and the device behaves as a resistor with resistance given by $V_{SG}$. A very popular model to describe the charge transport mechanisms that dominate this regime is the *gradual channel* approximation[38], that assumes a channel length $L$ much bigger than the dielectric thickness $d$ (this condition is satisfied in common OFETs). Following this model, it is possible to find (Eq. 9):

$$I_D = \frac{W}{L}\mu C_{diel}\left[(V_{SG} - V_{Th})V_{SD} - \frac{1}{2}V_{SD}^2\right] \quad [9]$$

Where $W$ is the channel width, $\mu$ is the charge carrier mobility and $C_{diel}$ is the capacity of the dielectric layer of the transistor.

As $V_{SD}$ increases and becomes closer to $V_{SG}$, these two potentials start to interact and the free charge density decreases in the vicinity of the drain electrode. When $V_{SD} = |V_{SG} - V_{Th}|$, $I_D$ stops growing even if $V_{SD}$ is increased and the area of the conductive channel near the drain electrode is depleted of free charges: at this point, the channel becomes *pinched off* (Fig. 19c)[30].

### *2.2.2 Saturation regime*

After the pinch-off condition is reached, if a higher $V_{SD}$ is applied, $I_D$ does not grow. This phenomenon is caused by the increasing depletion of the channel between source and drain, that becomes wider and wider (Fig. 19d). This condition (when $V_{SD} > |V_{SG} - V_{Th}|$) is called *saturation regime*, and a different equation (Eq. 10) is needed to describe the drain current after the channel has been pinched off:

$$I_D = \frac{W}{2L}\mu C_{diel}(V_{SG} - V_{Th})^2 \qquad [10]$$

Which arises from the constrain on the source-drain voltage at $V_{SD} = |V_{SG} - V_{Th}|$.

The differences between these two regimes are particularly relevant since they also affect the shapes of the *transfer characteristics*, from which the main electrical parameters of a transistor are calculated (next section).

### *2.3 Electrical characterization*

The main measurement that is performed in order to find the parameters that describe the features of an OFET is the *transfer characteristics*, namely the measurement of the drain current as function of the gate voltage, while keeping the drain-source voltage constant (Fig. 20).

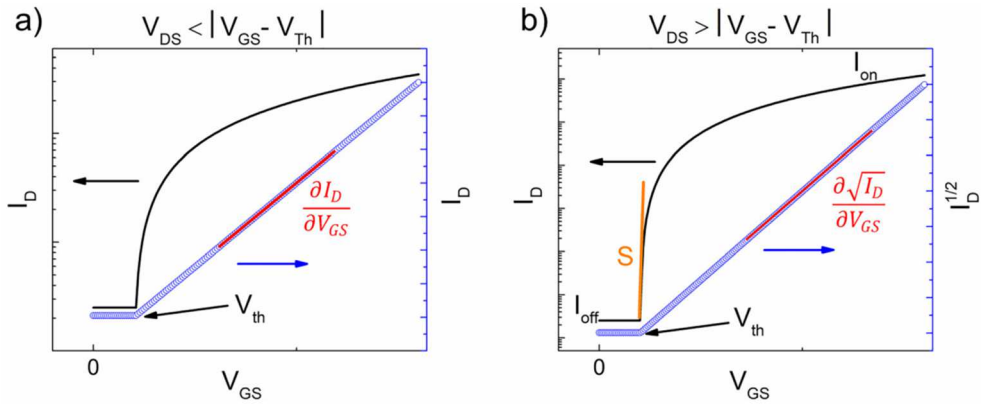


*Fig. 20: Transfer characteristic in linear (a) and saturation (b) regimes. From this measurement, it is possible to extract the main electrical parameters of a device.*

Before pointing out the details of the practical extraction of the parameters, their definitions are discussed.

### *2.3.1 Figures of merit*

- **Field-effect mobility (μ)**: the electrical mobility is the parameter that measures how quickly charge carriers can move when an external electric field is applied. Its theoretical definition can be written as $v_d = \mu E$, where $v_d$ is the drift velocity of the charge carrier and $E$ is the applied electric field. It is often measured in $cm^2/Vs$, and ranges from roughly 0.1 $cm^2/Vs$ for amorphous silicon up to 1000 $cm^2/Vs$ for high-ordered inorganic single crystals[12]. Organic semiconductors often present a high degree of disorder, and their values of mobility cannot compete with inorganic materials, even if in recent year many materials and techniques have been investigated to improve this figure of merit, with very promising results and mobilities higher or in the same order of magnitude of amorphous silicon[39].

- **On/Off ratio**: the on/off ratio, as the name might suggest, is the ratio between the current flowing through the conductive channel when the device is "on" and "off". A wide on/off ratio is desired in many applications since it permits to distinguish clearly the two possible states of the device. $I_{off}$ can be minimized by choosing a proper dielectric material, while $I_{on}$ can be maximized working on the mobility of the semiconductor, on the capacity of the dielectric and on the density of trap states[30].
- **Threshold voltage ($V_{Th}$)**: the deviation of the threshold voltage from zero is one of the results of the presence of trap states within the semiconductor layer. These states are the first to be filled when $V_{SG}$ is applied, before free charges can contribute to the drain current. Since in most cases the density of traps depends on temperature, $V_{Th}$ temperature dependence can be used to provide an estimation of the interfacial trap states $N_{it}$, according to Eq. 11.

$$N_{it} = \frac{C_{diel}}{k_b q}\frac{\partial V_{Th}}{\partial T} \qquad [11]$$

Where $k_b$ is the Boltzmann's constant, $T$ is the temperature and $q$ is the elementary charge[30].

- **Subthreshold swing (S)**: the subthreshold swing accounts for the rapidity of the device in switching from the "off" to the "on" state. It is measured in V/decades (more details in the next section), and its value depends on the interfacial trap states and on the temperature, according to Eq. 12.

$$S = \frac{k_b T ln(10)}{q}\left(\frac{N_{it}q^2}{C_{diel}} + 1\right) \qquad [12]$$

Where all quantities have already be defined in previous equation. A lower value of the subthreshold swing indicates that the switching off and on of the device is fast. A theoretical lower limit for S exists, since with no interfacial trap states present, Eq. 12 would provide S = 60mV/dec[30].

### *2.3.2 Extraction of parameters*

All the parameters that have been defined in the previous section can be extracted from the transfer characteristics of a transistor, both in linear and saturation regime. In particular,

- The **mobility** can be extracted using Eq. 9-10 depending on the regime the transfer characteristics is measured, as depicted in Fig. 20. More in detail, it is possible to exploit the following formula (Eq. 13a-b):

$$a)\ \mu_{lin} = \frac{L}{C_{diel} W V_{SD}} \frac{\partial I_D}{\partial V_{SG}}, \quad b)\ \mu_{sat} = \frac{2L}{C_{diel} W} \left(\frac{\partial \sqrt{I_D}}{\partial V_{SG}}\right)^2 \qquad [13]$$

  In ideal devices, these two expressions should provide the same result, but in those cases where the contact resistance (this effect will be discussed in section 2.4.1) plays a major role, this non-ideality has a stronger impact in linear regime and produces a lower $\mu_{lin}$ with respect to $\mu_{sat}$. Indeed, contact resistance decreases the effective $V_{SD}$, which in the linear regime is already smaller than in the saturation one, so that the final underestimation is bigger[30].

- Together with the mobility, it is possible to also extract the **threshold voltage**, that can be operationally defined as the voltage at which the drain current is zero. This can be seen graphically in Fig. 20, where the red regression line intersects the zero-current line.
- The **on/off ratio** can be easily extracted from the maximum and minimum values of the transfer characteristics, as it is possible to see in Fig. 20b.
- To extract the **subthreshold swing**, it is necessary to plot the saturation regime drain current in logarithmic scale and apply Eq 14:

$$\frac{1}{S} = \frac{\partial (log_{10}(I_D))}{\partial V_{SG}} \qquad [14]$$

  The result of this kind of linear regression can be seen in the orange line in Fig. 20b.

All these parameters that can be extracted from the transfer characteristics of a transistor provide relevant information on the quality of the final device and can be used (together with the shape of the transfer curve) to identify the main non-idealities that may impact in the correct functionality of the OFET. Therefore, an accurate analysis is necessary to point out possible solutions to improve the performances of the device, acting on the fabrication processes or on the active material composition. In the next section, we will discuss the most common defects that can be present in OFETs.

## *2.4 Main non-ideality effects in OFETs*

Non-idealities represent the main challenge to find a reliable value of the electric parameters of a device[40]. Even if the origin of them is still not fully understood neither the techniques to reduce their consequences are completely effective, many procedures have been developed in order to recognize and get rid of the most common non-idealities[41]. In the following, a brief description of them will be provided, together with some strategies to lower the effect that they produce on the measurements reliability.

### *2.4.1 Contact resistance*

Even if most models that describe the electrical behavior of OFETs assume a negligible contact resistance, the recent development of high-mobility materials involved the presence of a lower and lower channel resistance $R_{Ch}$, which increased the impact of the contact resistance $R_C$ on the final behaviour of the device. As a result, in modern OFETs it is crucial to address this issue. The origin of the contact resistance lies in the fact that a non-zero voltage is needed to transfer charges from an electrode into the semiconductor, and viceversa[30]. This leads to a potential drop at the metal-semiconductor junction and reduces the effective $V_{SD}$ that eventually produces the drain current $I_D$. It is possible to express mathematically[41] this results as (Eq. 15):

$$I_D = \frac{V_D}{R_{Ch} + R_C} \rightarrow V_{Ch} = I_D R_{Ch} = V_D - I_D R_C \qquad [15]$$

The most common reasons why contact resistance appears include the presence of structural defects during the deposition process and the contamination of the surface of semiconductor layer, which gives rise to localized states at the metal-semiconductor interface and therefore to a higher injection barrier. On the other hand, the morphology of the semiconductor layer can be a key factor in the bulk component of the contact resistance $R_{C,\,bulk}$.

Therefore, two main contributions to contact resistance can be pointed out, namely injection from the contacts into the semiconductor ($R_{C,\,int}$) and charge transport within the semiconductor from the electrode interface to the channel ($R_{C,\,bulk}$). The former is mainly due to the injection barrier present between the electrode and the semiconductor, while the latter is due to the depleted semiconductor region close to the electrode. In the last case, the consequences can be diminished acting on the device geometry (mainly adopting a staggered geometry, as depicted in Fig. 17a and 17c)[30]. As we are mainly interested in the extraction of a reliable value of mobility, it is crucial to avoid both overestimation and underestimation that can arise from transfer characteristics where a large contact resistance is present. Indeed, in this condition, it is frequent to observe a "kink" that splits the drain current vs. gate-voltage plot into two regions with very different mobilities (Fig. 21).

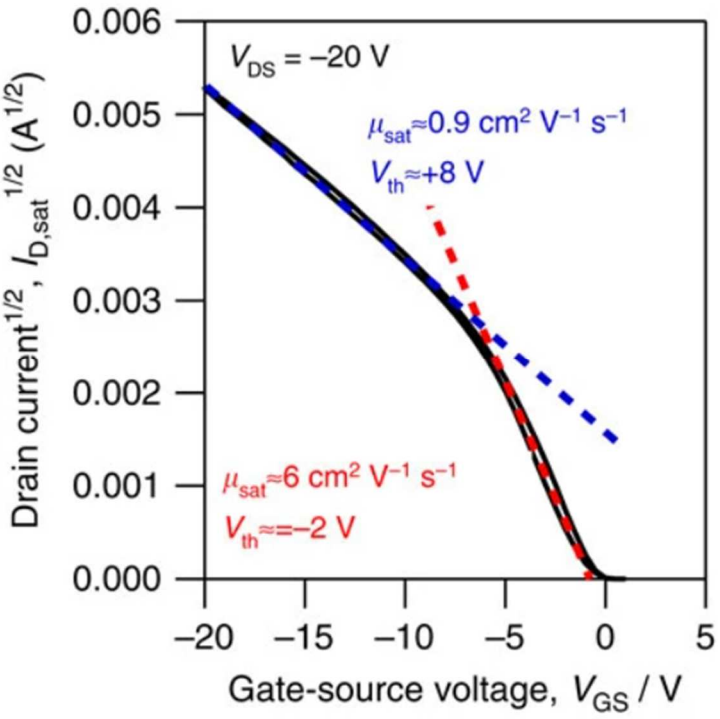


*Fig. 21: $I_D^{1/2}$ vs. $V_{SG}$ plot that shows how mobility evaluation at low gate voltages can lead to a major overestimation of its value in case a large contact resistance is present*[42].

Many engineering techniques exist to reduce contact resistance and flatten the kink of the $I_D$-$V_{SG}$ curve, resulting in a more linear relation (Fig. 22)[43].

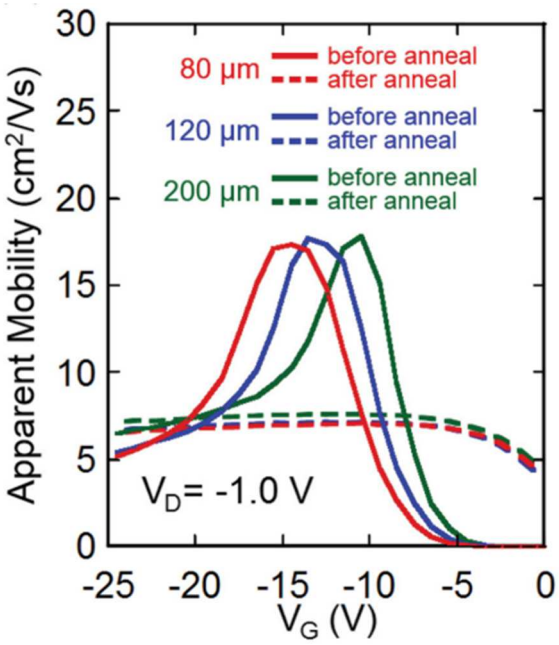


*Fig. 22: Apparent mobility as function of $V_{SG}$ for linear regime[43]. It is possible to see that the best estimation of the mobility before the annealing is performed is the plateau observed at high $V_{SG}$.*

### *2.4.2 Hysteresis*

In the case of transistors, the term *hysteresis* indicates the difference in the current values that can be measured during the forward and the reverse voltage sweep. This phenomenon can take place in different ways, depending on the kind of doping and on the main factors that originate the effect, so that it is common to distinguish between clockwise and anticlockwise hysteresis (Fig. 23).

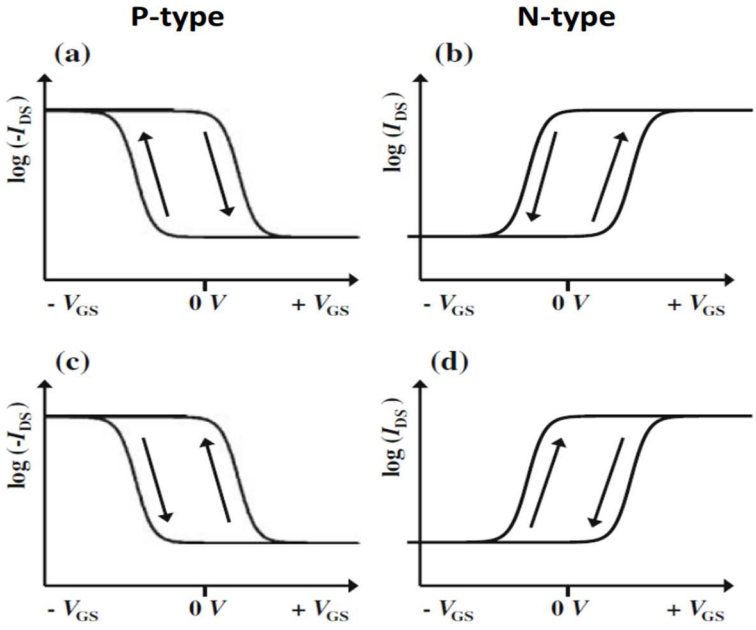


*Fig. 23: Schematic transfer characteristics for p-type and n-type OFETs. The arrows indicating the directions of the voltage sweep are used to determine the kind of hysteresis present*[44].

Hysteresis can be ascribed to a huge variety of physical phenomena, that can be divided into three main categories, according to the position in the device they originate from[45]:

- Effects in the region of the semiconductor channel (close to the semiconductor-dielectric interface), such as trapped charges, mobile ions and charge injection from the semiconductor into the dielectric
- Bulk effects of the dielectric, such as the presence of mobile ions in the dielectric material or its polarization
- Charge injection from the gate into the dielectric

A detailed dissertation of the features of all contributions would go beyond the scope of this work. Anyway, it is important to highlight that the hysteresis in the transfer characteristic of a device is a relevant track of the presence of trap states and impurities at the semiconductor-dielectric interface and within the dielectric material.

### *2.4.3 Bias stress*

With the expression *bias stress*, we mean all the effects that can be observed in the electrical characteristics of a device after it is operated with a continuous bias applied. This effects often include a lowering in the drain current, a shift in the threshold voltage, a lower mobility and a higher subthreshold swing[46] (Fig. 24).

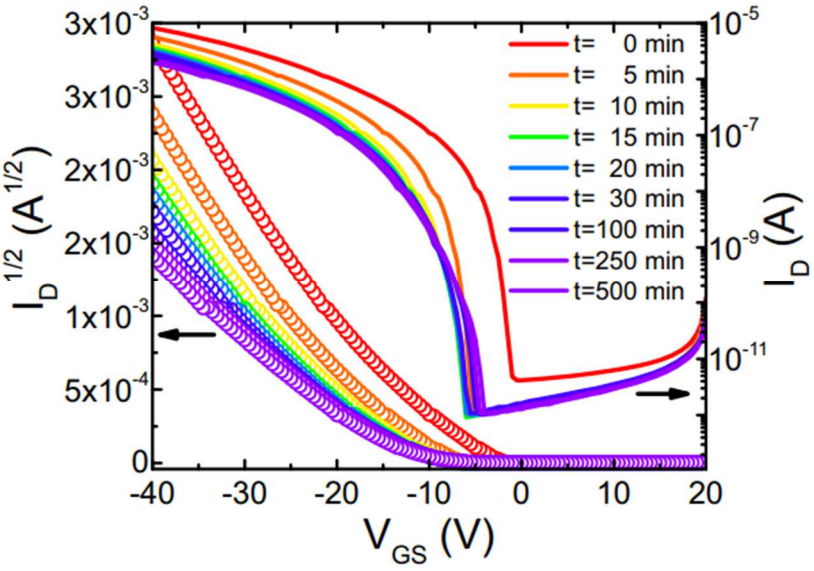


*Fig. 24:Time evolution of the saturation transfer characteristic after increasing times of device biasing ($I_D$ vs. $V_{SG}$ at $V_{SD}$=-60 V). Left and right axes measure the square root of the drain current and the logarithmic scale of the drain current, respectively[46].*

The consequences of a continuous applied bias are mainly due to majority carrier trapping: this causes a reduction in the output current, induced by a shift in the threshold voltage (which grows in absolute value). This non-ideality can be effectively reduced applying a pulsed gate voltage and tuning properly the cycle times. In addition, it is possible to mitigate bias stress acting on one of the main causes of traps formation, namely the oxidation of the organic semiconductor: indeed, the use of an encapsulating materials that stops the oxygen from spreading through the active layer can strongly improve the stability over time of a constantly biased device (Fig. 25)[46].

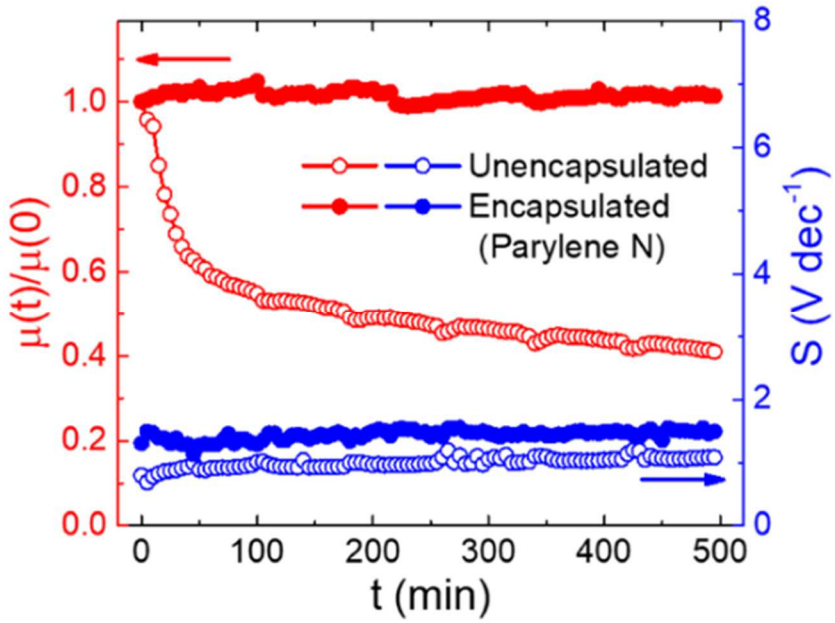


*Fig. 25: Comparison between the time variation of mobility (in red) and subthreshold swing (in blue) for encapsulated and unencapsulated devices[46]. In the first case, a better stability can be clearly observed.*

### *2.5 X-ray characterization by Organic Field-Effect Transistors*

In the last decade, the research interest into OFETs for X-ray detection has increased substantially, in light of their excellent results and promising perspectives. The phototransistor architecture allows to reach higher sensitivities thanks to the possibility to control the charge density in the conductive channel between source and drain, and therefore to enhance the output signal by acting on two externally applied biases ($V_{SG}$ and $V_{SD}$)[30]. In addition, the use of organic materials shows a wide variety of advantages and makes the device compatible with the typical applications of organic electronics. For these reasons, OFETs can merge the qualities of traditional FETs with those of organic active layers.

However, field-effect transistors were not the first architectures used to test organic active layers in X-ray detection: indeed, the first attempts with these innovative compounds were carried out using Schottky diodes[47] and photodiodes[48], and resulted in devices with much lower sensitivities with respect to the main inorganic competitors (their sensitivity was in the order of 1μC/Gy·cm$^2$, one and two orders of magnitude lower than amorphous selenium and CZT, respectively). In the following years, researchers explored new possibilities to enhance the performances of organic-based detectors: among them, it is worth mentioning the addition of bismuth oxide nanoparticles[49] (high-Z compound that led to better and better performances in following years[50]) and the use of carbon nanotubes[51]. In this last case, in 2014, the sensitivity of amorphous selenium detectors was reached, and the following year, for the first time, a similar performance was achieved using a flexible detector made of a single crystal organic semiconductor[52].

In 2017, the first organic field-effect transistor was reported[53], with a sensitivity value slightly lower than record ones among organic-based detectors. Within one year, OFETs were able to go over the performances of amorphous selenium detectors[24], and since 2020 their sensitivity growth has been recorded: in that year, Temiño et al.[10] reported a record-performing sensitivity (i.e. higher than the one reported for poly-CZT) thanks to an OFET that took advantage of a better understanding of the influence of morphology and mobility on the final performance[54]. Indeed, the blending of the organic semiconductor small molecule (TIPS-pentacene) with an insulating polymer called *polystyrene* (PS) strongly improved charge collection properties and the sensitivity to X-rays: devices made of blended active layers showed a sensitivity bigger by one order of magnitude with respect to those that employed pure TIPS-pentacene small molecules, and the same trend was observed in the case of mobility, which was bigger by up to two orders of magnitude in blended films. Together with the blending of the active layer, also the deposition technique and the active layer morphology impact was studied in detail. Indeed, this work assessed the features of organic field-effect transistors that were deposited using Bar-Assisted Meniscus Shearing (BAMS), a procedure in which the deposition speed is a remarkably important parameter to tune the grain dimensions.

In particular, as it is possible to see in Fig. 26, a low speed resulted in bigger grains, but these devices showed also a lower sensitivity. Temiño et al[10]. explained this effect demonstrating that the electrical active trap states for minority carriers able to activate the photoconducting mechanism (already described in Chapter 1) are strictly related to the grain boundaries. This is the reason why, when a low density of grain boundaries is present (i.e. big grains due to a lower deposition speed) the inner amplification mechanism is lower and consequently also the final sensitivity.

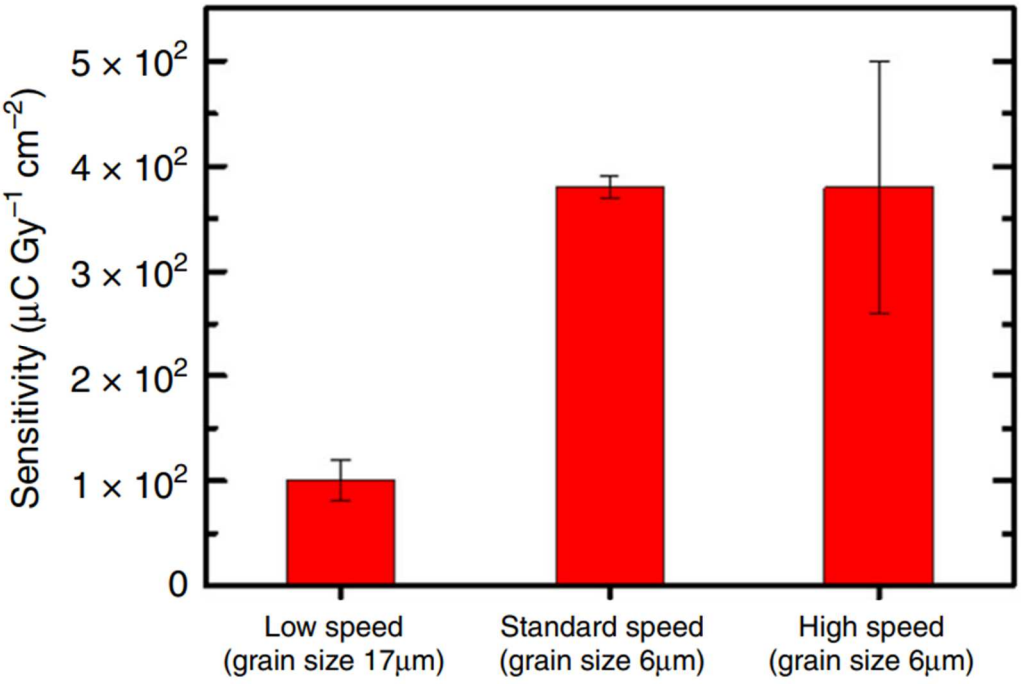


*Fig. 26: Sensitivity as a function of deposition speed. Low speed produces worse quality films, with lower sensitivity and bigger crystal grains*[10].

In 2022, the same technique and organic polymer were employed together with a different organic semiconducting small molecule, namely TMTES[28]. In this work, together with a record sensitivity (in the order of $10^5$ μC/Gy·cm$^2$), the impact of polystyrene on the morphology of the final blend was investigated even more in detail: thanks to ToF-SIMS depth profiling (Fig. 27), the vertical separation of the blended active layer was determined, and the presence of a bottom PS layer that passivates the interfacial traps for majority carriers was assessed.

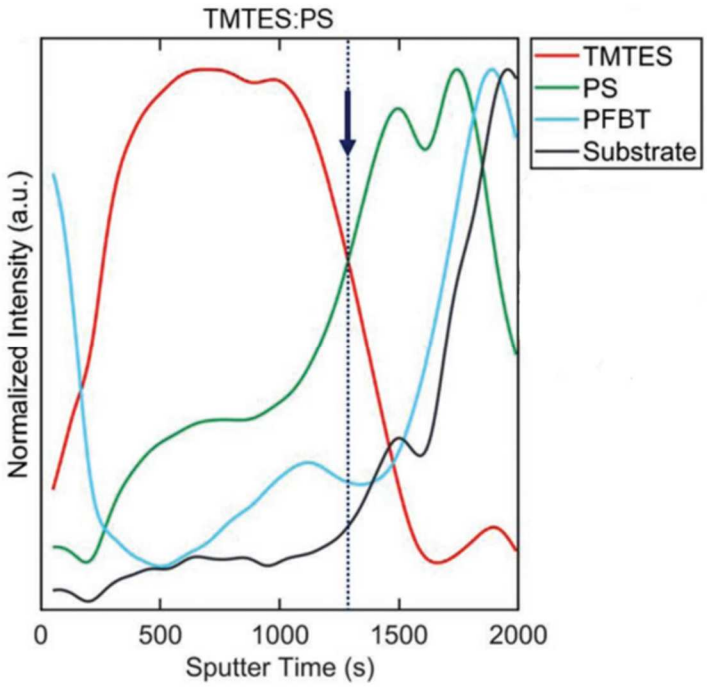


*Fig. 27: ToF-SIMS study of the TMTES:PS thin films. The normalized ToF-SIMS depth profile was acquired in the channel area of the OFET starting from the surface and reaching the $SiO_2$ substrate*[28].

This discovery confirms the importance of the study of the morphology of the blend that makes up the active layer of OFETs and, together with the impressive increase of organic-based detectors, opens a wide variety of new possibility to achieve even better results in the use of organic field-effect transistors for ionizing radiation detection. The present work aims to deepen the knowledge of the main parameters of blended active layers that can have an impact on the final performance of the device, together with the possibility of adding an encapsulating layer in order to improve the stability over time of the most important electric parameters.

# *Chapter 3:*
# *Experimental Techniques*

In the following, we describe the main fabrication processes that were employed to produce the samples and the fundamental experimental techniques that allowed to characterize them. First of all, we highlight that the fabrication of the samples took place at the *Institut de Ciencia de Materials de Barcelona* (ICMAB), by Dr. Marta Mas-Torrent research group, while I took care of the electric and X-ray characterization steps using the facilities of the Department of Physics and Astronomy in the University of Bologna (UNIBO). In this chapter, the fabrication of the OFETs will be described with a particular emphasis on the organic semiconductor layer deposition and on the possible addition of a parylene-C encapsulation layer. In the end, the experimental procedures adopted during the characterizations will be discussed, together with the ToF-SIMS method that was employed by the Professor Branchini e Dott. Tortora research group at the University of Roma Tre to study the composition of the active layer as a function of the depth, down to the substrate and the composition and morphology at the surface of the organic layer.

### *3.1 OFETs fabrication*

The fabrication processes were carried out in Barcelona according to the procedures reported in previous works in literature and that allowed to fabricate devices showing very good and reproducible performances[10,28,31]. Before the deposition of the organic semiconductor blend, the electrodes were patterned by photolithography on a highly p-doped silicon wafer (the initial substrate) with a 200 nm layer of $SiO_2$ on top. They were deposited by thermal evaporation starting with a 5 nm thick layer of chromium acting as adhesion layer followed by 40 nm of gold. These devices were designed in the form of a pixel with an active area A= $4.25 \cdot 10^{-3}$ $cm^2$ made with a channel length L=25 µm and a channel width W=2500 µm, thus with a channel width/length ratio equal to 100. At this point, the substrates were cleaned by sonication with acetone and isopropanol and dried with a nitrogen flow. The surface of drain and source contacts were chemically treated with a self-assembled monolayer (SAM) of 2,3,4,5,6-pentafluorothiophenol (PFBT). The gold activation step was performed with the exposition to a UV ozone cleaner for 25 minutes and then with the immersion in a $10^{-3}$ M solution of PFBT in isopropanol for 15 minutes. Eventually, the substrates were cleaned with pure isopropanol to wash away the PFBT in excess and dried with a nitrogen flow. After all these steps, the deposition of the organic semiconductor layer was performed: 1,4,8,11-Tetramethyl-6,13-triethylsilylethynyl pentacene (TMTES) and polystyrene (PS) with different molecular weights (10k, 100k, 280k g/mol) were bought from Ossila[55] and Sigma-Aldrich[56] respectively and used with no further treatments. TMTES/PS solutions were produced in anhydrous chlorobenzene with final concentration 2.0% w/w. The blends were prepared with four different volume ratios, namely 2:1, 4:1, 1:2 and 1:0 (with no polystyrene). Before the deposition, the solutions were heated to the temperature of the hot plate (105 °C). Then, the Bar-Assisted Meniscus Shearing (BAMS) technique was used to produce the active thin films of the devices, with a substrate temperature of 105 °C and a constant coating speed of 10 mm/s (more details in the next

section). All these processes were performed in ambient conditions and without additional thermal treatment[28]. In order to study the impact of an encapsulation layer on top of the OFETs, the same steps were carried out, followed by the deposition of the parylene-C layer acting as encapsulation. The details of the encapsulation process are discussed in section 3.3.

## *3.2 Organic semiconductor layer deposition*

The step in which the organic semiconductor layer is deposited is the most important one: it was emphasized in previous sections since it is crucial to determine the final performance of the device and its transport properties, so that its optimization has gathered the attention of researchers for years[29]. Therefore, a detailed description of its parameters and steps is required.

### *3.2.1 Bar-Assisted Meniscus Shearing (BAMS) technique and its parameters*

All the samples that were studied in this work had active layer deposited using Bar-Assisted Meniscus Shearing (BAMS), one of the possible solution shearing techniques. This kind of deposition methods rely on the linear translation of either the substrate or the coating tool (different ones exist) to induce an alignment in the crystal orientation while the film grows. This feature is particularly important for electronics applications, as it can enhance transport properties along a specific direction[29]. All these techniques take advantage of the evolution of a solution meniscus, namely the interface between the solution and the air by which the evaporation of the solvent takes place. Once the point of supersaturation is reached, solute precipitation begins and eventually a thin film is left on the substrate. In the case of BAMS, a cylindrical metal bar is kept some hundreds of micrometers above the substrate, which is sheared at a constant speed while kept at a constant temperature. By deposition techniques from solution, it is possible to tune morphological and transport properties of the organic semiconducting layer by varying different parameters of the deposition. Here in the following, some examples reported in literature are reported.

The importance of the temperature of the hot plate beneath the substrate has been assessed with a wide study in 2017 by Galindo et al.[31], from which it is possible to see how the previously mentioned temperature has a remarkable impact on the shape of the transfer characteristics and, thus, on the electric parameters (Fig. 28).

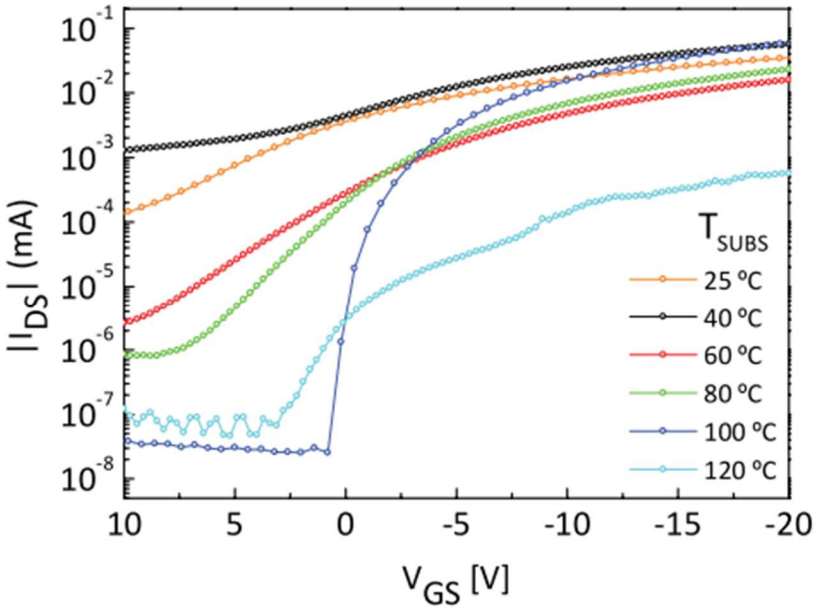


*Fig. 28: Transfer characteristic of an OFET with different substrate temperatures. It is possible to see that a temperature close to 100 °C produces the best shape of the drain current and, as a consequence, the best electric parameters[31].*

On the other hand, the coating speed plays a key role as well: for instance, it has a great impact on the grain dimension, which is a major feature of the morphology of the film, representing one of the most important factor for the final performance of the device (Fig. 29)[10].

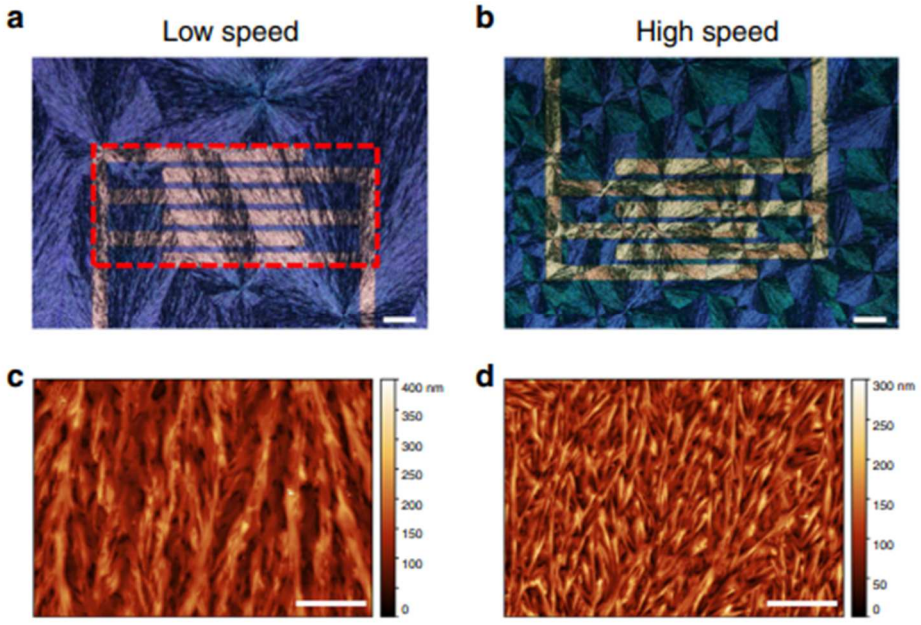


*Fig. 29: Influence of different coating speeds (4 and 28 mm/s) on the morphology of the film. a) and b) are optical microscope images, while c) and d) are AFM topography images*[10].

In 2021, another study by Tamayo et al.[57] proved that a low coating speed can lead to a relevant anisotropy in the mobility of the deposited film, with higher mobility values along the direction of the coating blade movement (Fig. 30).

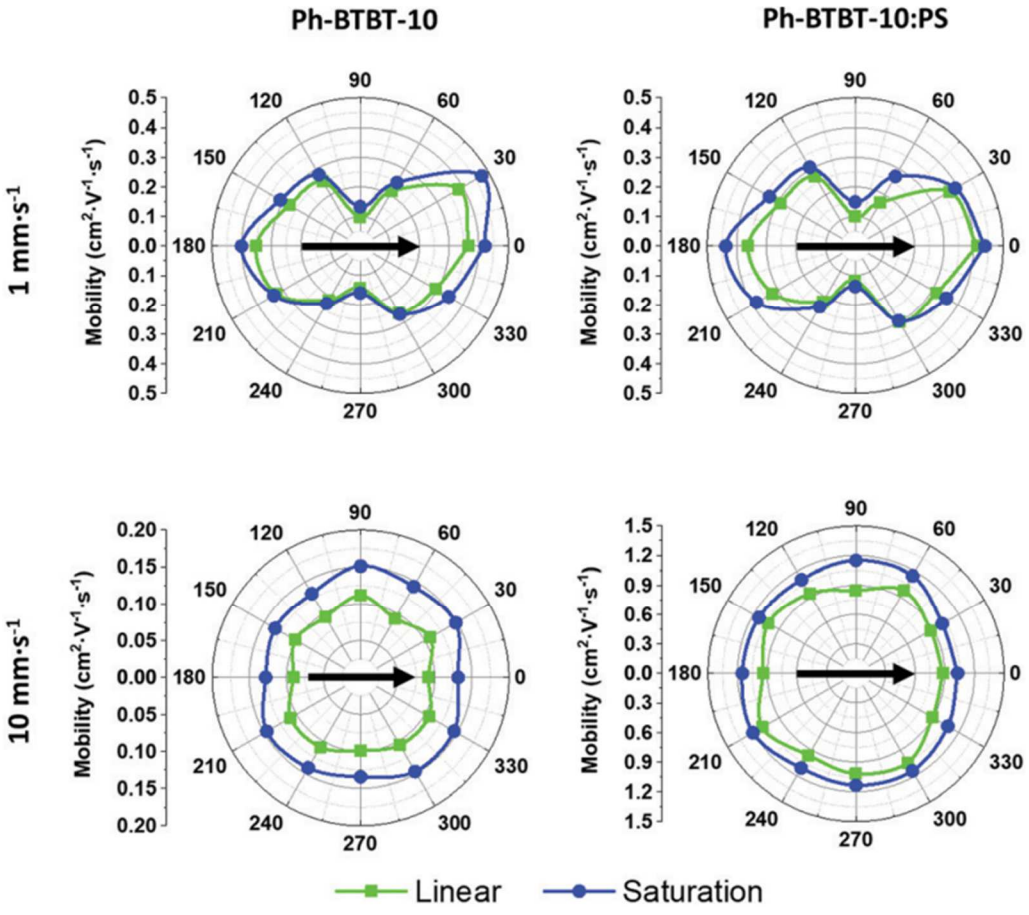


*Fig. 30: Polar plot of the linear and saturation mobility of the Ph-BTBT-10 at low and high coating speed. The direction of the solution shearing is indicated with a black arrow*[57].

### *3.2.2 Active molecule: TMTES*

In this work, the active organic layer of the studied devices is made of a blend in which the small molecule organic semiconducting molecule is represented by 1,4,8,11-tetramethyl-6,13-triethylsilylethynyl pentacene (TMTES, Fig. 31).

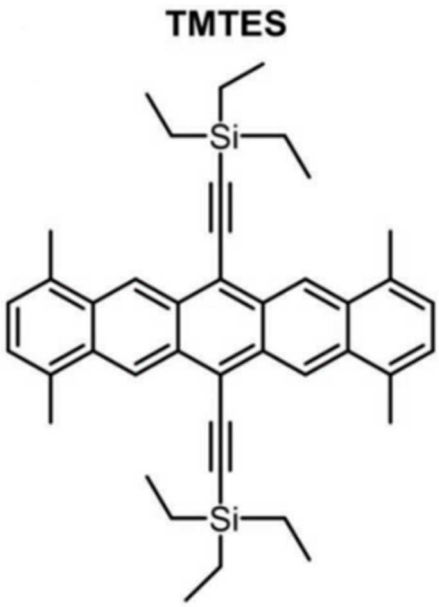


*Fig. 31: Molecular structure of TMTES*[28].

The molecular structure of TMTES is similar to that of TIPS-pentacene, but when BAMS is employed as deposition technique, thin films crystallize in a completely different way.

This results in OFETs with very high mobilities, up to 2.5 $cm^2/Vs$ [28]: the origin of such a high electric performance can be traced back to the particular structure in which TMTES crystallizes in these blends. Indeed, TMTES is known to crystallize in two ways, named Polymorph I (PI, with a slip-stack structure) and Polymorph II (PII, with a herringbone motif)[58]. X-ray diffraction experiments showed that, in polystyrene blends, TMTES crystallizes in this last phase, with a crystal orientation that ensures the highest possible mobility (Fig. 32)[28].

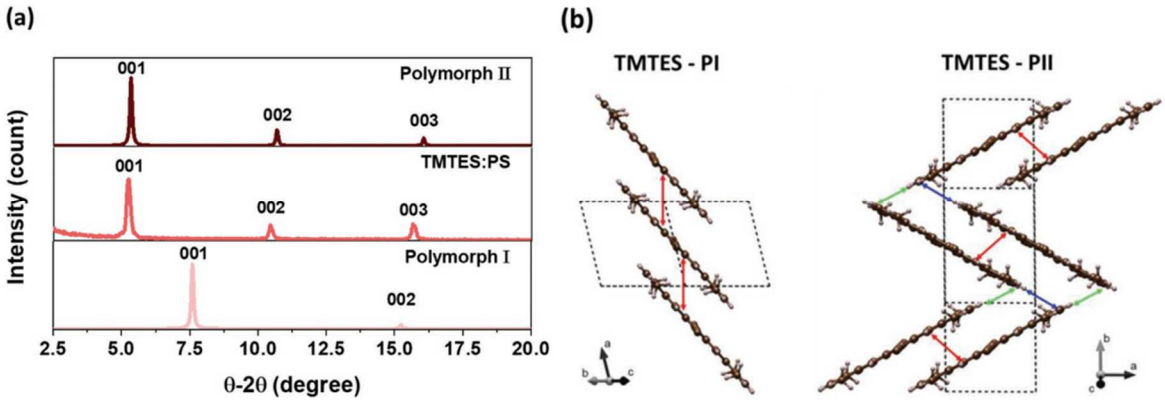


*Fig. 32: On the left, X-ray diffractogram of a TMTES:PS blend compared to reported PI and PII diffractograms, from which the latter phase can be clearly identified. On the right, the crystal structure of the two possible phases of TMTES[28].*

### *3.2.3 Final active blend:* **Polystyrene** *(PS) role and parameters*

Except for two substrates that contained pure TMTES active layers, in this work we will discuss the performance of devices made of a blend of TMTES with *polystyrene* (PS). This organic material (Fig. 33) is a synthetic polymer produced from the polymerization of the aromatic hydrocarbon monomer *styrene*.

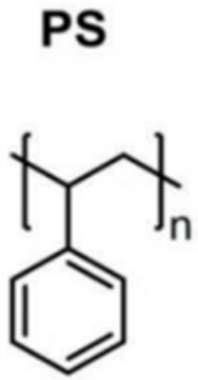


*Fig. 33: Molecular structure of polystyrene[28]. Since polystyrene is a polymer, the length of its polymeric chain is not fixed and depends on the number of attached monomers* n.

The reason why this polymer has been chosen as binding polymer in different work reported in literature in the last years[10] lies in its low relative permittivity, good solubility in organic solvents, low cost and a weak interaction with organic semiconductors[28]. The blending of small molecule (TMTES) with insulating polymers has shown positive effects on the semiconductor processability, a better crystallization in the final thin film, better electric performance and stability over time[59]. The main parameters that involve the use of PS and its intrinsic features are mainly two: the volume ratio between TMTES and PS and PS molecular weight.

The former has already been investigated in the case of TIPS-pentacene in 2020, and its impact on the performances of the device (both electric and under X-rays) has already been assessed[10]. The latter derives from the possibility of controlling the length of the polymeric chain that constitutes PS and therefore the weight of the molecule (measured in kilodalton [kDa]), and has not been investigated previously. Both parameters are evaluated in this work and their impact on the performance of the devices based on TMTES organic small molecule will be discussed.

## *3.3 Encapsulating layer*

The importance of encapsulation has already been discussed in section 2.1.3, in its most general employment and features. In the present work, the role of an encapsulation layer on top of the active layer of OFETs has been evaluated both in its interfacial and bulk effects, thanks to a very common and popular polymeric material: parylene-C.

### *3.3.1 Parylene-C as encapsulating material*

*Parylene* is the commercial name of a family of semicrystalline thermoplastic polymers known as poly(para-xylylenes), or PPX. The chemical structure of parylene is a linear chain of benzene rings with two methylene groups in place of two hydrogen atoms on opposite sides of the ring. More than 20 kinds of parylene-derived materials exist, depending on the atom that substitutes one or more hydrogen atoms in the benzene ring[60]. When no hydrogen atom is removed from the benzene ring, the polymer is called *parylene-N*, while when a chlorine atom is added, we have *parylene-C* (Fig. 34).

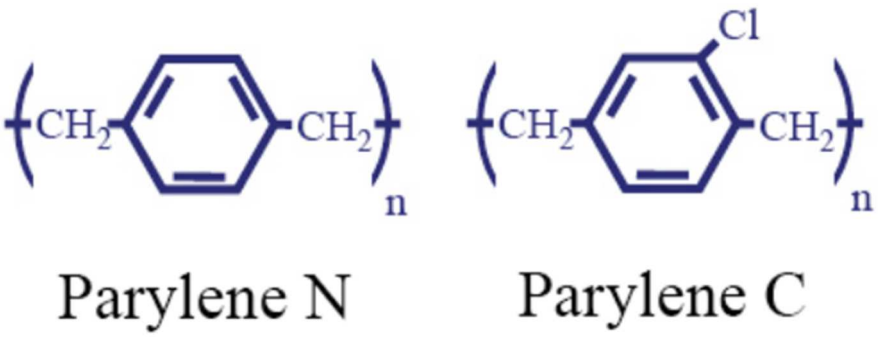


*Fig. 34: Molecular structure of Parylene-N (left) and parylene-C (right)*[60].

The existing variants of parylene show different features, and they are meant for diverse purposes: Parylene-N is mainly used as a dielectric and when lubricity and crevice penetration is important. Parylene-C is an ISO 10993, United States Pharmacopeia (USP) Class VI material (the highest biocompatibility rating for plastics in the United States) and has excellent water barrier properties. In addition, it has high flexibility and mechanical strength[61].

In this work, the encapsulating layers used in OFETs are made of parylene-C, an ideal material for this purpose: it can be deposited at room temperature, it is transparent, flexible, chemically inert and compatible with microfabrication processes[62]. In addition, parylene is a good barrier to air moisture and gases thanks to its low permeability and shows good properties as a pinhole-free dielectric material[63]. Due to all these features, this polymer has already been used in electronic devices with important results as dielectric material, as a substrate and as a passivation layer in Thin Film Transistors (TFTs)[64]. The use of parylene as a substrate for TFTs has been key factor to produce flexible devices for which a great interest has been present for years, as mentioned in previous chapters. On the other hand, the use of parylene-C in the dielectric layer of TFT is mainly due to its uniformity and excellent dielectric strength that ensures high resistance to breakdown[65]. This material has also been deeply studied in the fields of life sciences in prostheses, neural implants[60] and cell growth, thanks to the biocompatibility that has been assessed by the Food and Drug Administration (FDA). Finally, another reason why parylene-C is a popular polymer for very different purposes lies in its affordable and simple deposition technique called *Gorham vapor deposition*.

### *3.3.2 Encapsulation layer deposition*

Parylene polymers were discovered in 1947 by Michael Szwarc, and the very first parylene film deposited was parylene-N, with no substitutional atoms on the benzene ring. The deposition method that was used at that time had the disadvantage of having gaseous by-products as an intrinsic part of the process. William Gorham, an employee at Union Carbide, implemented an alternative method that involved the pyrolysis of a dimerized form of the material, called *di-para-xylylene*. When Gorham developed his method, there was no way of obtaining the dimer in large amounts, but this limitation was overcome by Donald Cram in 1951, who found a way to produce this compound in bulk. Therefore, on February 17, 1965, Union Carbide claimed the availability of parylene films produced according to this new vacuum deposition process, named after William Groham[60].

Gorham vapor-deposition process[66] takes place in different steps (Fig. 35) and is carried out in vacuum condition, in order to increase the mean free path of particles to the substrate. The reactant is represented by di-para-xylylene (parylene dimer): it is placed in a vaporizer furnace, that causes the evaporation of the dimer at 130-150 °C. The vapor passes through a high temperature pyrolysis furnace (between 650 and 750 °C) where the molecule is split into two monomers. At this point, the monomers enter a chamber that is kept at room temperature and polymerization takes place on all exposed surfaces in the chamber. Eventually, the monomer residue is collected into a cold trap. This vapor deposition process can show some variants, depending on the specific kind of parylene that is required as final product, but the steps that were described here are mostly the same[61].

The encapsulating layer of the devices studied in this work was deposited thanks to this method, but with an additional last step that is due to the electrically insulating nature of parylene: since the deposition process covers all the surface of the device, including the pads that are used to connect it when operated, it was necessary to scratch the parylene layer in the region of the pads in order to allow a proper connection with the three electrodes of the device.

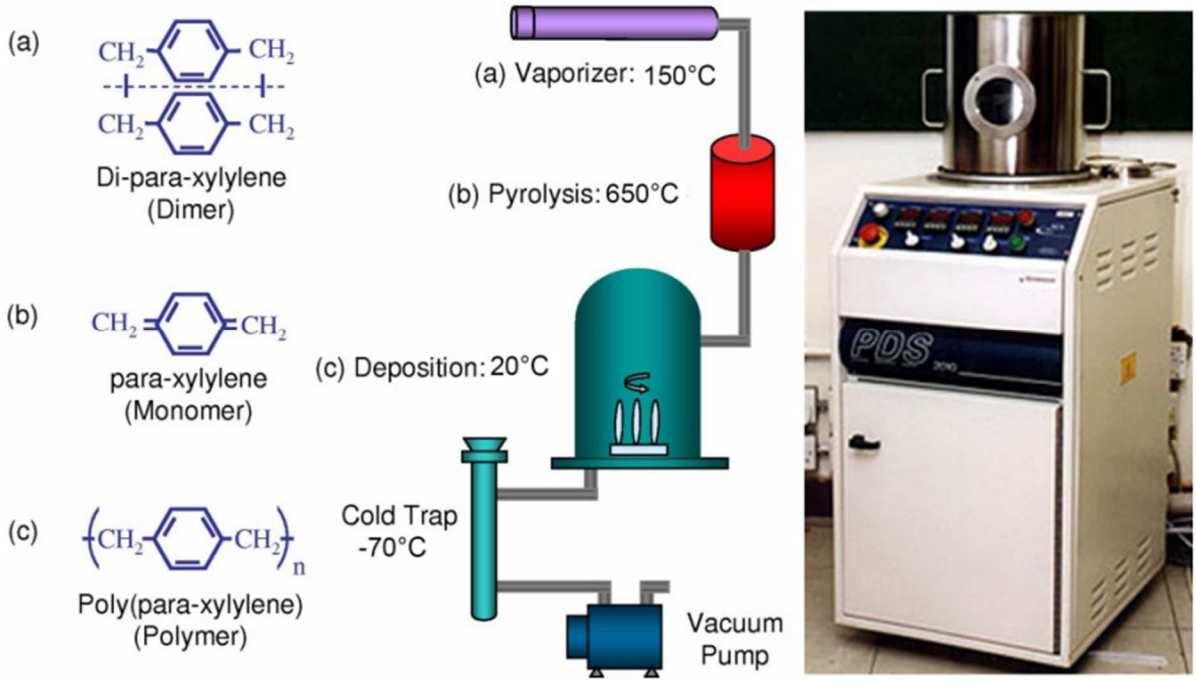


*Fig. 35: Gorham vapor deposition. On the left, chemical species present during every step of the vapor deposition. On the right, Gorham process main steps. Adapted from* [61].

## *3.4 Characterizations setup*

The devices that were studied in this work underwent two different kinds of characterizations, namely *electric* and *under X-rays*. By the electrical characterization we extracted the main electrical parameters described in Chapter 2 and we evaluated the transport performances of the electrical devices, while the characterization under X-rays was intended to assess the performances of the OFETs as radiation direct detectors. The two experimental setups employed for the characterizations will be discussed in the following.

### *3.4.1 Electrical characterization*

The electric characterization of the OFETs is carried out using the probe station shown in Fig. 36 (left). This cage is employed both as a Faraday cage to screen the electromagnetic noise coming from the external and also to prevent the illumination of the device during the measurements. The devices under test are connected using three tungsten micro-tips and placed onto the three pads of the transistors, which correspond to the source, drain and gate terminals (Fig. 36, right). The tips are connected to a Source Meter (Keysight B2912A) that allows to derive the output and transfer characteristics of the device. From these curves the main electric parameters have been extracted as it is described in the previous chapter (i.e. mobility, threshold voltage and subthreshold swing).

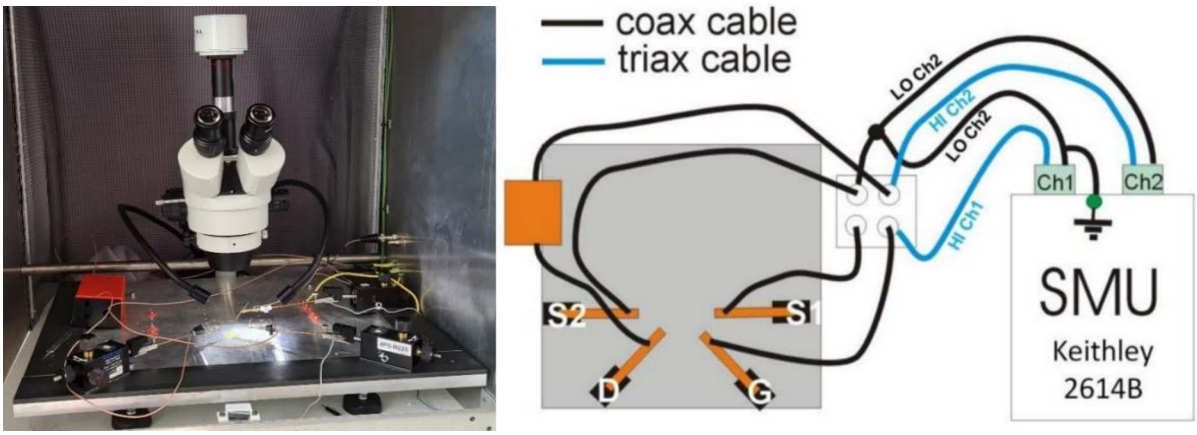


*Fig. 36: On the left, the probe station used for the electric characterization. The apparatus is placed inside a closed Faraday cage to screen external light and electromagnetic noise. On the right, the scheme of the connections used to extract the characteristic curves of the OFETs.*

The Source Meter used in this kind of measurements is a two-channels Keysight B2912A (Fig. 37).


*Fig. 37: Front panel (left) and rear part of the Keysight B2912A Source Meter.*

In Fig. 38, the main specifications of the instrument are reported.

## Voltage source specifications

| Range | Programming resolution | | Accuracy (% reading + offset) | Noise (peak to peak) 0.1 Hz to 10 Hz[1] | Max voltage (over range) |
|---|---|---|---|---|---|
| | B2901A/B2902A | B2911A/B2912A | | | |
| ±200 mV | 1 µV | 100 nV | ±(0.015 % + 225 µV) | ≤ 10 µV | ±210 mV |
| ±2 V | 10 µV | 1 µV | ±(0.02 % + 350 µV) | ≤ 20 µV | ±2.1 V |
| ±20 V | 100 µV | 10 µV | ±(0.015 % + 5 mV) | ≤ 200 µV | ±21 V |
| ±200 V | 1 mV | 100 µV | ±(0.015 % + 50 mV) | ≤ 2 mV | ±210 V |

1. Supplemental characteristics

## Current measurement specifications

| Range | Measurement resolution | | Accuracy (% reading + offset) |
|---|---|---|---|
| | B2901A/B2902A | B2911A/B2912A | |
| ±10 nA[1] | — | 10 fA | ±(0.10 % + 50 pA) |
| ±100 nA | 100 fA | 100 fA | ±(0.06 % + 100 pA) |
| ±1 µA | 1 pA | 1 pA | ±(0.025 % + 500 pA) |
| ±10 µA | 10 pA | 10 pA | ±(0.025 % + 1.5 nA) |
| ±100 µA | 100 pA | 100 pA | ±(0.02 % + 25 nA) |
| ±1 mA | 1 nA | 1 nA | ±(0.02 % + 200 nA) |
| ±10 mA | 10 nA | 10 nA | ±(0.02 % + 2.5 µA) |
| ±100 mA | 100 nA | 100 nA | ±(0.02 % + 20 µA) |
| ±1 A | 1 µA | 1 µA | ±(0.03 % + 1.5 mA) |
| ±1.5 A | 1 µA | 1 µA | ±(0.05 % + 3.5 mA) |
| ±3 A | 10 µA | 10 µA | ±(0.4 % + 7 mA) |
| ±10 A[2] | 10 µA | 10 µA | ±(0.4 % + 25 mA)[3] |

1. 10 nA range is not available for B2901A/B2902A.
2. 10 A range is available only for pulse mode, not available for DC mode.
3. Measurement speed: 0.01 PLC

*Fig. 38: Keysight B2912A datasheet for voltage drop generation and current reading[67].*

The Source Meter was controlled remotely via a custom LabView software where all measurement parameters were set and controlled.

### *3.4.1 X-ray detection characterization*

The characterization of the device as detector of ionizing radiation was carried out placing the samples into a metallic box (Fig. 39) where the device under test could be electrically connected to the connectors using silver paste, and then to a Source Meter. This allowed to keep the sample in dark throughout the measurements session and to get rid of external electromagnetic noise, since the metal box works as a Faraday cage. A mm thick lead foil was placed on the cover of the box to screen the readout and the connection components from the ionizing radiation. This screen presents a window that allows the X-ray to irradiate the samples under test. The X-ray beam was produced by an X-ray tube (see section 1.1) whose operative details will be provided in the following.

*Fig. 39: Metal box used during the irradiation sessions. The box is covered with lead in the front part except for a small square corresponding to the sample under test, that permits to focus the beam on it. The square is covered with aluminum foil to screen external light.*

The X-ray tube that was employed in these measurements is made of a tungsten target whose radiation spectrum is shown in Fig. 40.

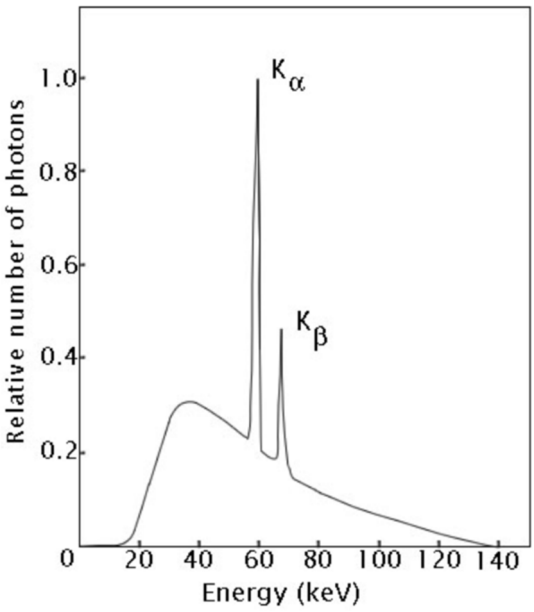


*Fig. 40: Emission spectrum of an X-ray tube with tungsten target. The peaks $k_\alpha$ and $k_\beta$ represent the characteristic X-ray lines, while the lower intensity part is the* bremsstrahlung *radiation.*

The energy of the spectrum is determined by the voltage of the tube while the dose rate of the emitted radiation is mainly determined by the tube current.

The intensity of the radiation emitted by the tube was initially calibrated employing the output of a commercial detector (BARRACUDA X-ray Analyzer, Fig. 41).

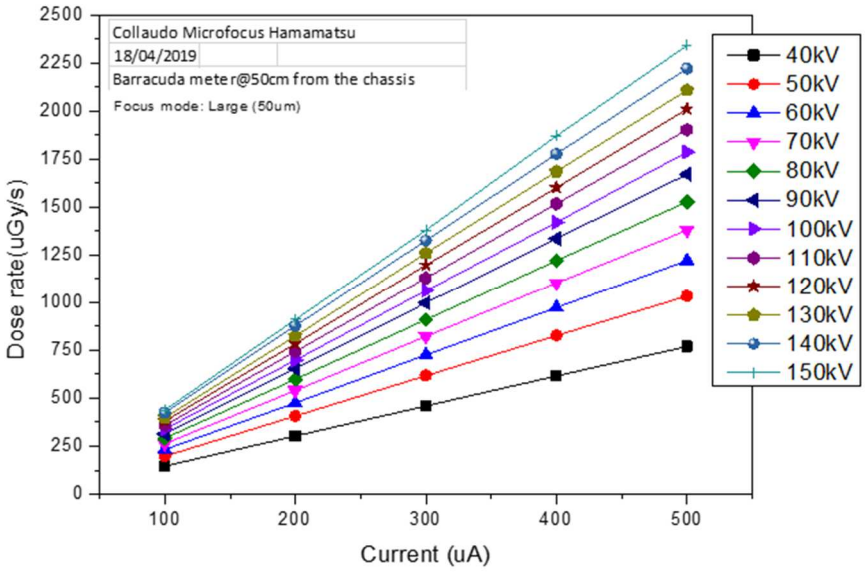


*Fig. 41: X-ray tube calibration. The calibration was performed using different tube voltages and currents, from which it is possible to find the dose rate correspondent to every working point. The calibration has been done placing the BARRACUDA X-Ray Analyzer at 50 cm from the X-ray tube.*

Another important variable that has an impact on the dose rate that impinges on the sample is the distance between the detector and the focus of the X-ray tube. In all the measurements this distance was 17cm, from which it is possible to find the values of the four different dose rates used during the irradiation sessions, where the tube voltage was fixed at 40kV and only the tube current was varied (Tab. 1).

| Corrent (μA) | Dose Rate (μGy/s) |
|---|---|
| 100 | 1300 |
| 200 | 2700 |
| 350 | 4600 |
| 500 | 6600 |

*Tab. 1: Tube currents and correspondent dose rates for tube voltage at 40kV and distance 17cm.*

The irradiation apparatus is shown in Fig. 42. In front of the X-ray tube, a mechanic shutter with a lead slab is used to stop the irradiation towards the sample when required by the experimental protocol. This control is performed remotely using a custom LabView software that allows to run the shutter both manually and with automatic cycles.

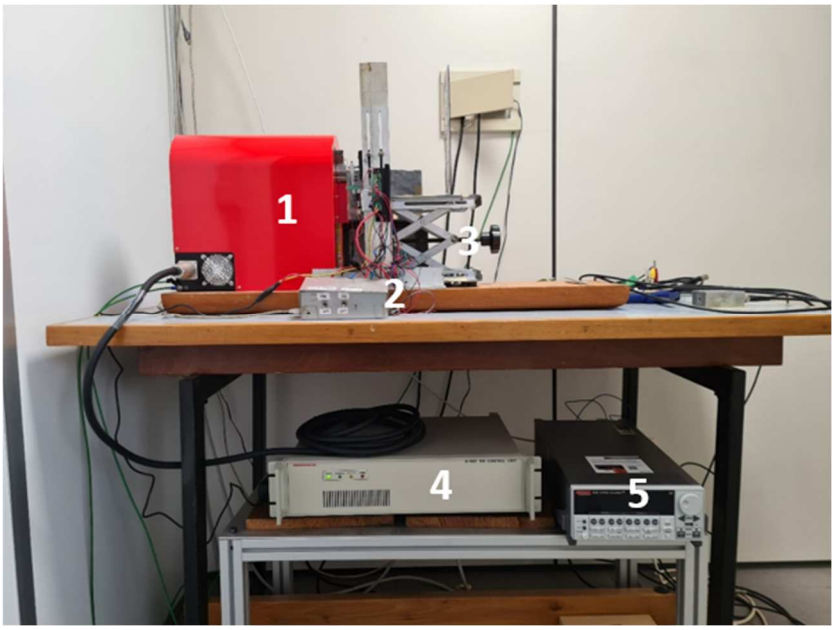


*Fig. 42: Experimental apparatus for X-ray irradiation. On the desk, it is possible to see (from the left) the X-ray tube (1), the support for the shutter with the switch (2) and the support for the metal box with a knob to adjust the height of the sample. Under the table, it is possible to see the high voltage generator (4) and the Source Meter (5, a Keithley 2614 controlled remotely) that is used to polarize the sample under test and to record its currents. All the necessary connections are realized using coaxial cables.*

The detection of X-ray radiation can be measured by the continuous and real time acquisition of the sample current flowing through the channel of the OFETs as a function of time. When the X-ray irradiates the sample, a photocurrent is generated because of the absorption of energy by the semiconducting layer. The photocurrent is defined as the difference between the drain current flowing with and without impinging radiation, with the origin of this current due to the X-ray-matter interaction mechanisms already discussed in section 1.2.

### *3.5 ToF-SIMS*

Secondary Ion Mass Spectroscopy (SIMS) is an experimental technique that allows to detect the presence of elements in a sample for both the analysis of impurities or dopants trace concentrations and composition determination. This method can be applied to study materials in distinct ways: it is possible to obtain information in the horizontal plane on the surface of a 2D-sample as well as to produce a depth profile on the Z-dimension of a bulk sample. The fundamental principle that SIMS relies on is the atomic erosion of the surface of the studied sample, that is realized using a beam of heavy ions [62]. The penetration of a fast ions beam through the surface of a solid compound involves just a few tens of nanometers, in which primary ions transfer their kinetic energy to the local atoms as a result of multiple collisions. Part of this energy can eventually be transferred to surface atoms, that gain enough kinetic energy to leave the solid and be emitted. This is the main source of information about the chemical composition of the studied surface, even if not the only one (for instance, electrons and photons, not treated here)[63]. The sputtering of the surface produces *secondary ions*, that can be studied with a mass spectrometer in a wide range of concentrations.

In the case of Time-of-Flight Secondary Ion Mass Spectroscopy (ToF-SIMS), the ions beam that is directed towards the sample surface is pulsed[62]: this is needed by a time-of-flight spectrometer (Fig. 43) in order to analyze the secondary ions coming from the surface with the shortest possible time interval. When the pulsed ions beam hits the surface, secondary ions are generated almost simultaneously and then accelerated by a fixed voltage $U_{ac}$, before entering the flight path of length $L$. At this point, it is possible to measure the time-of-flight $T$ and therefore find the mass of the secondary ion, which is directly connected to its elemental identity[63].

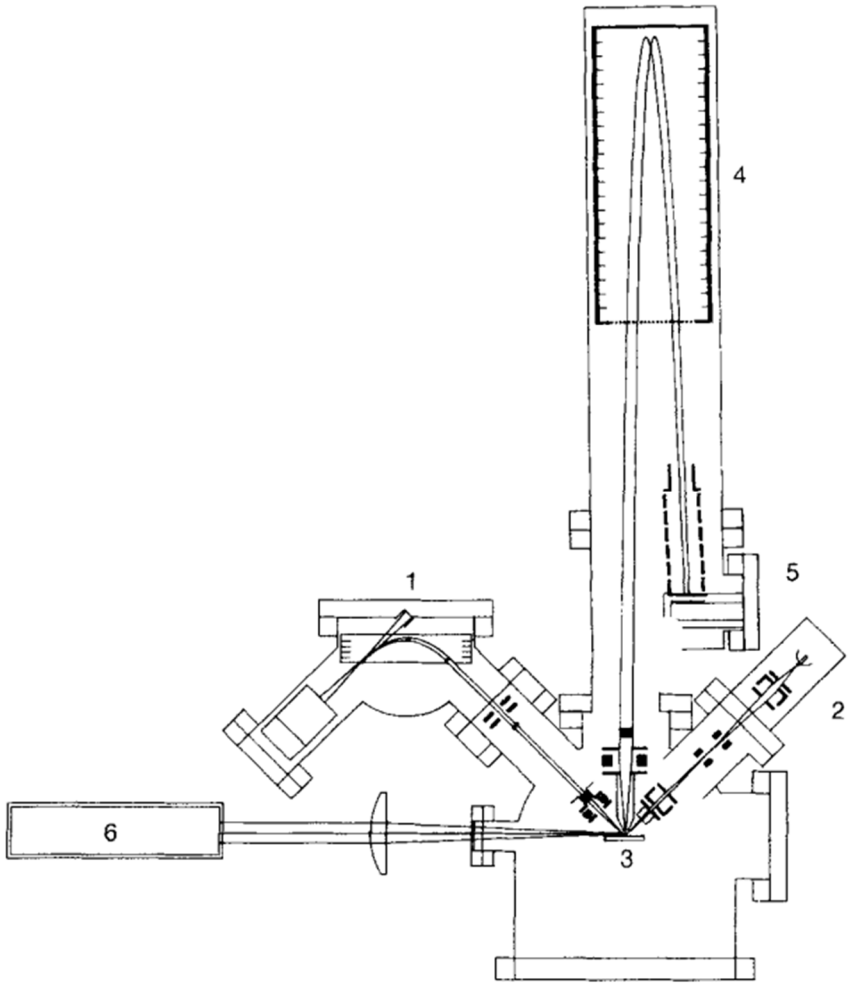


*Fig. 43: Scheme of the main components of a modern high-resolution time-of-flight spectrometer. It is possible to distinguish a pulsed mass-separating electron impact ion source (1) and a pulsed fine-focusing liquid metal ion source, producing beams with different diameters. The other parts of the experimental instrument are the target (3), a reflector for energy focusing the mass-separated focusing ions (4), a detector (5) and a laser for post-ionization of emitted neutral particles*[63].

A time-of-flight spectrometer is made of three main parts: the primary ion source(s), the accelerating and flight path system and the detector. The source of primary ions can be varied according to the needs of the experiment, while the other elements of the instrument are fixed.

As mentioned above, ToF-SIMS is a versatile technique that can be operated in different modes. First, a very popular employment is the large-area surface analysis[63], in which the scope is to determine with high sensitivity the chemical structure of the upper layer of a solid. In this kind of measurements, the radiation damage that this technique produces beneath the first layer of atoms hinders the possibility of a *depth profile* analysis of the bulk sample. This last operational mode allows to study the vertical composition of the thin film that constitutes the active layer of the OFETs tested in this work, and permits the evaluation of a possible segregation of polystyrene. Indeed, it was proven that the presence of a phase separation between the active small-molecule and the inert polymer allows the latter to act as a passivation layer for majority carrier trap states at the interface with the $SiO_2$ dielectric layer, enhancing the performance of the detector[23]. In this specific operational mode, a pulsed primary ion beam is used to remove many monolayers in a small surface area (typical beam diameter in the order of 1 pm). This kind of analysis can penetrate the material with a velocity in the order of ten monolayers per second, but it is not compatible with a molecular investigation of the sample, due to the damage produced by the ion beam in the sample. The limitation of this mode to an elemental analysis is not an issue for the objectives of this work, since the presence of certain chemical species is enough to discriminate between the two compounds of the active blends used in these samples ($SiC^-$, $SiCH^-$, $SiC_2H^-$, $SiC_5H_2^-$ and $SiC_7H_2^-$ for TMTES, $C_3H_3^-$, $C_4H_3^-$, $C_5H_3^-$, $C_6H_3^-$ and $C_7H_3^-$ for PS[23]).

### *3.6 Scripts for data analysis*

The data analysis step of this thesis work was performed using python scripts that I coded and by which the main electrical parameters and the sensitivities of the devices under test were extracted. In particular, the electrical mobility, the threshold voltage and the subthreshold swing slope of the detectors were extracted from their transfer characteristics in saturation regime. The electrical mobility has been calculated using Eq. 13b and, from the same regression line, the threshold voltage has been extracted. To find the subthreshold swing, Eq. 14 was employed.

On the other hand, the sensitivity measurements were taken using multiples irradiation cycles, according to a standard protocol: set to zero the time at which the device was polarized, no irradiation was used for 60 s in order to let the current stabilize. After this *wait time*, 4 irradiation cycles took place, every one of them made of 60 s with no radiation followed by other 60 s when the sample was bombarded with X-rays. From all off intervals (four in total), the last current points were used to normalize the drain current with a parabolic fit to get rid of possible increasing or decreasing trends that would alter the signal.

Once the signal had been preprocessed as described above, it was possible to calculate the signal (photocurrent) that a certain dose rate produces (Fig. 44).

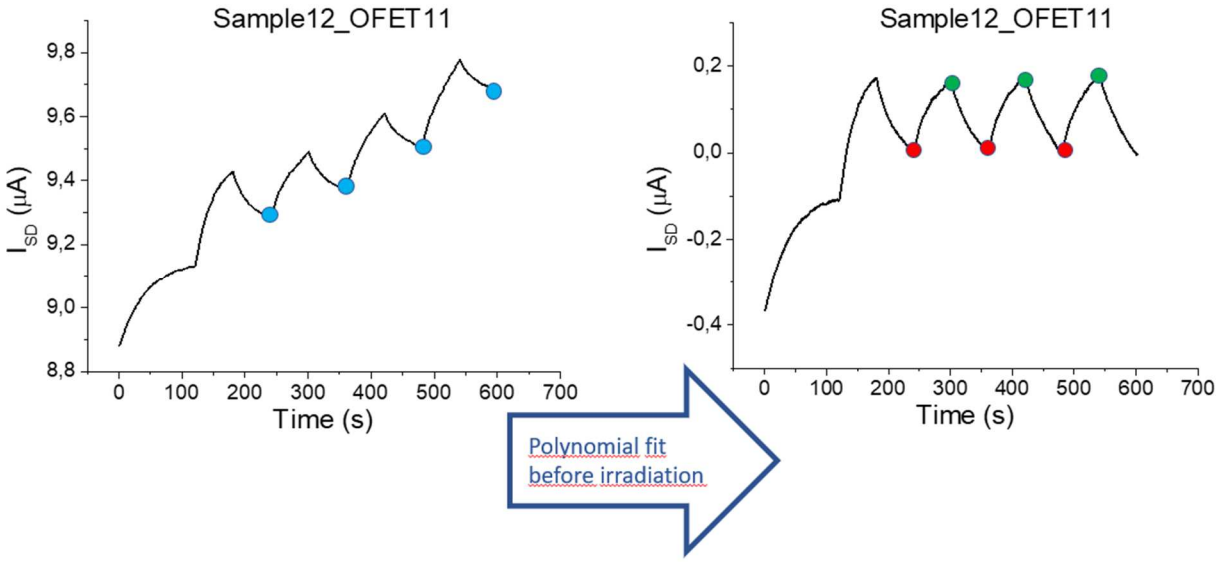


*Fig. 44: Current normalization procedure. On the left, it is possible to see how a sensitivity measurement appers as it is performed. The light blue dots are used to fit a parabola to normalize the signal, the result of which is reported on the right: Green and red dots indicate the peaks and the minima from which the photocurrent is calculated (the last three), respectively. The three values are then averaged and associated with their semidispersion to provide an estimation of the signal for the given dose rate*

The plot of the photocurrents vs. dose rate provides the sensitivity of the device, according to the operative definition given in section 1.3.3.

The details of said scripts can be found in Appendix. A.

# *Chapter 4:*
# *Results and Discussion*

In the following chapter, before showing the main results of the electric and X-rays characterizations of the OFETs batches that were analyzed in this work, a resume of their nomenclature and features is provided. In conclusion, the ToF-SIMS analyses of these samples is provided and discussed in light of the characterizations results and considering possible new perspectives opened by the conclusions of this work for future investigation.

### *4.1 Characterized batches: main features and parameters of interest*

In this thesis, two separate studies were performed: in the first three sample batches, the role of the TMTES:PS volume ratio and of the PS molecular weight were investigated using three different ratios (one per batch) and three different PS molecular weights. In the last two sample batches, the impact of the presence of a parylene-C film was analyzed both in the case of an interfacial and bulk contribution of the encapsulating layer (with a 900 nm and 7.5 µm thick parylene layer, respectively). All batches share a common structure of the devices and of the substrates on which they are fabricated (Fig. 45).

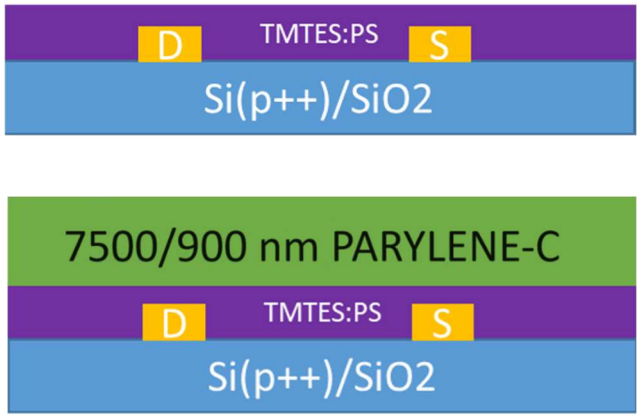


*Fig. 45: Scheme of the structure of not encapsulated (upper part) and encapsulated samples (lower part). In both cases, the thickness of the Si/$SiO_2$ substrate is 200 nm and the electrodes (D and S) are made of gold.*

The channel features are reported in Tab. 2, together with the active area of the device pixel.

| Channel length (µm) | Channel width (µm) | Specific capacitance ($F/cm^2$) | Pixel area ($cm^2$) |
|---|---|---|---|
| 25 | 2500 | $17.3 \cdot 10^{-9}$ | $4.25 \cdot 10^{-3}$ |

*Tab. 2: Channel features of the batches for TMTES:PS study. The pixel area in the quantity needed to normalize the sensitivity to the active area of the device.*

In the case of the TMTES:PS study, every batch has a fixed ratio and three different PS molecular weights, namely 280 kDa, 100 kDa and 10 kDa. Every molecular weight is used in two substrates, containing four OFETs each, with a common gate structure (Fig. 46). Therefore, 24 transistors are present in every batch, 8 for every molecular weight.

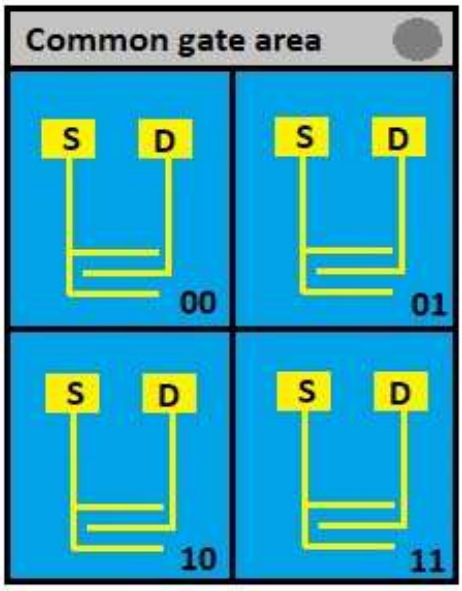


*Fig. 46: Structure of a substrate, in which 4 OFETs are deposited. It is possible to see the matrix-like numeration of the devices and the common gate area with a circular scratched zone that allows to connect the silicon substrate that constitutes the common gate.*

The three batches were named after their fabrication date, namely 20230315, 20230427 and 20230508 for the 2:1, 4:1 and 1:2 TMTES:PS ratio batch, respectively. In the following, they will be referred to as MW21, MW41 and MW12 in order to employ a clearer and shorter notation. Since these batches contain a total of 72 transistors, just the mean value of the parameters of every composition will be shown here (the complete results of the characterization will be shown in Appendix B)

On the other hand, the role of parylene was studied in two batches called 20230412 (containing samples with a 7.5 µm thick encapsulation layer and not encapsulated ones, in the following referred to as P7500) and 20230606 (containing samples with a 900 nm thick encapsulation layer and a not encapsulated one, in the following called P900). Both batches have the same geometric features reported in Tab. 2, with an active blend made of TMTES:PS with a fixed 2:1 ratio and 280kDa PS molecular weight. In this case, the batch structures are widely different: batch P7500 is made of 8 substrates, each one of them containing 4 OFETs with common gate (Fig. 47), for a total of 32 OFETs. The first 4 substrates are coated with parylene-C, the electrically insulating polymer that was described in section 3.3, while the last 4 (Substrate 5-6-7-8) have no encapsulation and possess the same features of the batch MW21 with 280kDa PS molecular weight.

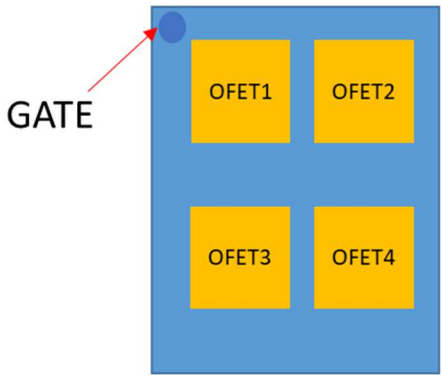


*Fig. 47: Structure of a substrate of batch 20230412. The numeration of the OFETs is different from previously presented batches, but the common gate area with scratched zone to allow access to the silicon layer that constitutes the gate is the same.*

Batch P900 is made of just 3 samples and was mainly used to perform a recovery test, in which the devices were characterized electrically before, during and after X-ray irradiation. All these results of the encapsulation study are presented and discussed in section 4.4.

A resume table of the batches studied in this work is presented as follows (Tab. 3).

| Name of the batch | Name used in this thesis | Number of samples | Characterizations performed | Composition of the batch | Section of discussion |
|---|---|---|---|---|---|
| 20230315 | MW21 | 24 | Electrical, X-rays | 2:1 ratio | 4.2, 4.3, 4.4 |
| 20230427 | MW41 | 24 | Electrical, X-rays | 4:1 ratio | 4.2, 4.3, 4.4 |
| 20230508 | MW12 | 24 | Electrical, X-rays | 1:2 ratio | 4.2, 4.3, 4.4 |
| 20230412 | P7500 | 32 | Electrical, X-rays, Recovery test | 2:1 ratio, encapsulated | 4.5 |
| 20230606 | P900 | 3 | Electrical, Recovery test | 2:1 ratio, encapsulated | 4.5 |

*Tab. 3: Resume table of the batches that were studied in this thesis.*

In the following, the numerical results of the electric and X-ray characterizations of the batches MW21, MW41 and MW12 are shown (Tab. 4). The missing values of sensitivities are caused by a decrease in the current instead of the expected increase under irradiation. This phenomenon has already been reported in literature[17], but a deeper analysis of this effect goes beyond the scope of this work.

The trends that can be associated with the TMTES:PS ratios and PS molecular weights are discussed in section 4.2 and 4.3, respectively.

| Ratio, MW | μ ($cm^2 \cdot V^{-1}s^{-1}$) | $V_{Th}$ (V) | SS (V/dec) | Sensitivity ($\mu C \cdot Gy^{-1}cm^{-2}$) $\bullet 10^3$ |
|---|---|---|---|---|
| 2:1, 280kDa | 0.8±0.1 | 0.13±0.08 | 0.19±0.02 | 3.4±0.3 |
| 2:1, 100kDa | 0.73±0.04 | 0.15±0.05 | 0.18±0.02 | 2.6±0.2 |
| 2:1, 10kDa | 1.45±0.04 | 0.45±0.07 | 0.11±0.01 | 3.4±0.6 |
| 4:1, 280kDa | 2.4±0.1 | 0.63±0.07 | 0.49±0.04 | 5.4±0.9 |
| 4:1, 100kDa | 1.8±0.2 | 0.9±0.1 | 0.7±0.1 | 2.4±0.5 |
| 4:1, 10kDa | 1.8±0.2 | 0.80±0.04 | 0.99±0.08 | 3.0±0.1 |
| 1:2, 280kDa | 0.90±0.04 | 0.13±0.04 | 0.23±0.01 | 1.7±0.1 |
| 1:2, 100kDa | 1.27±0.07 | 0.22±0.03 | 0.26±0.01 | No |
| 1:2, 10kDa | 1.6±0.2 | -0.02±0.04 | 0.23±0.01 | No |

*Tab. 4: Electrical and X-ray characterization results for different TMTES:PS ratios and PS molecular weights. The reported parameters are the average values for every composition, and the associated error is the mean standard deviation. The 4:1, 10 kDa sensitivity was extracted from just one sample, so that the associated error is its own one.*

## *4.2 Role of TMTES:PS ratio*

In the batches MW21, MW41 and MW12, both the PS molecular weight and the TMTES:PS ratio vary. We will first discuss how the electric parameters and the sensitivity of the devices are influenced by the variation of the latter.

### *4.2.1 Electrical parameters*

First, we report the output and transfer characteristics of the devices. Here, a comparison between the OFETs based on pure TMTES and the ones based on the TMTES blended with polystyrene is shown (Fig. 48 and Fig. 49) By these characterizations we investigated and confirmed the impact of the presence of polystyrene on the OFET electric performance as previously reported in literature[20,23].

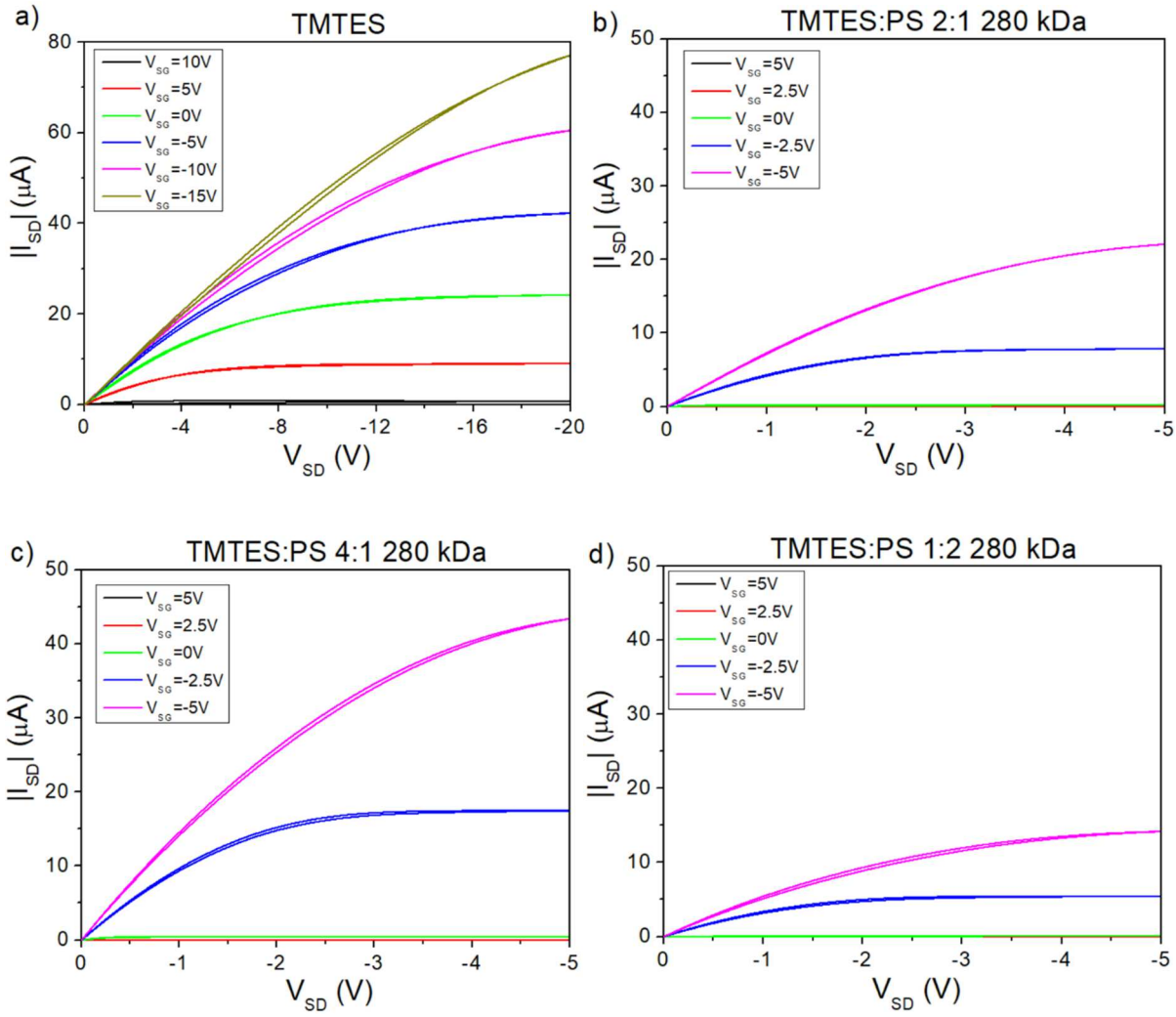


*Fig. 48: a) pure TMTES; b) TMTES:PS 2:1; c) TMTES:PS 4:1; d) TMTES:PS 1:2 output characteristics. All reported characteristics are taken from devices with 280 kDa PS molecular weight, but the same trend is present for 100 kDa and 10 kDa.*

From these graphs, it is possible to see that the presence of PS reduces the hysteresis and the threshold voltage (in pure TMTES samples, a $V_G = 5$ V is enough to measure a non-zero drain current, while in blended ones it is necessary to provide a negative gate voltage to switch them on). This is a first indication of the majority carrier traps passivation role played by the polystyrene, since both hysteresis and threshold voltage are effects connected to the density of interfacial trap states, and a reduction of these features in the output characteristics of the devices represents an indication of a lower interfacial trap states density.

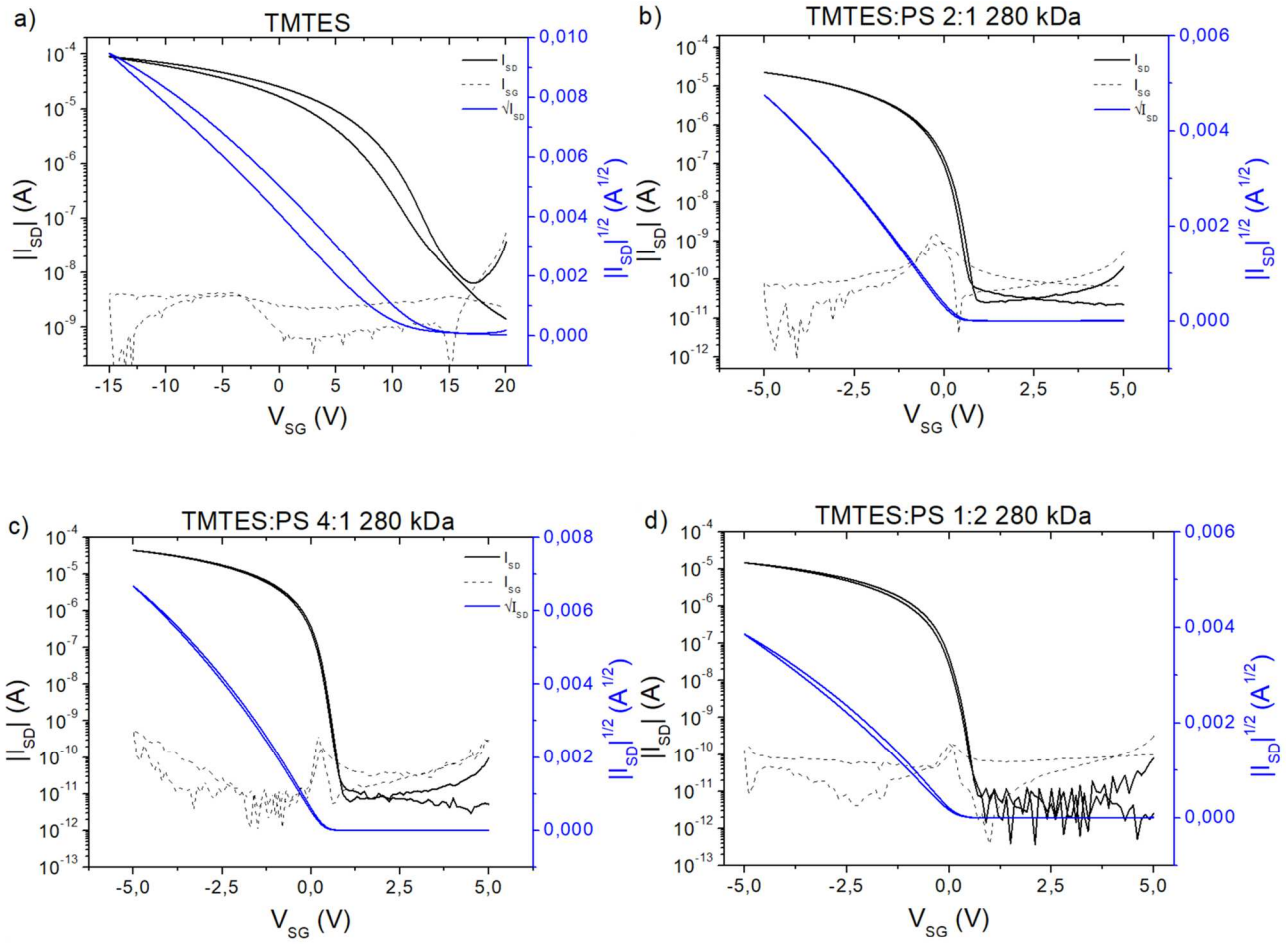


*Fig. 49: a) pure TMTES; b) TMTES:PS 2:1; c) TMTES:PS 4:1; d) TMTES:PS 1:2 transfer characteristics in saturation regime (VDS = -10). The dashed line represents the leakage current. All samples were measured with $V_D$=-10V. All reported characteristics are taken from devices with 280 kDa PS molecular weight, but the same trend is present for 100 kDa and 10 kDa.*

From the transfer characteristics in saturation regime reported in Fig. 49, no clear difference can be seen among blended samples: in all of them, the transfer characteristics show a very low hysteresis and leakage current, and a steep increase in the drain current in the logarithmic scale. All these features indicate good electrical parameters, which are confirmed by the data about threshold voltages and subthreshold swing.

The comparison with the pure TMTES sample is intended to highlight the impact of polystyrene on the transport properties of OFETs: it is straightforward to see that the absence of this polymer can be associated with a more marked hysteresis, a much higher threshold voltage and subthreshold swing and a leakage current higher by one order of magnitude. A quantitative analysis is presented with Fig. 50, where the average values of the electric parameters are shown as a function of the polystyrene concentration.

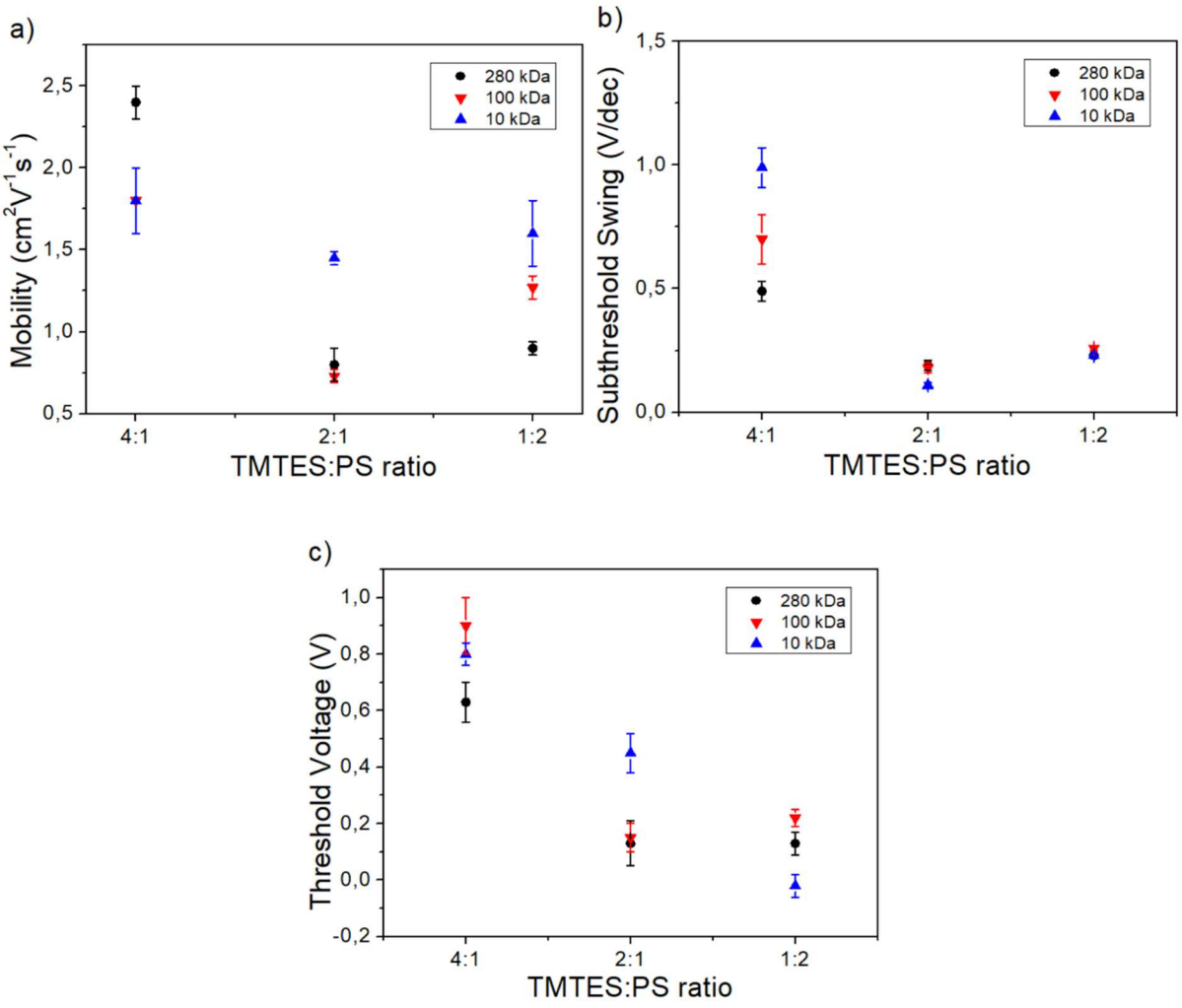


*Fig. 50: Electric parameters with increasing PS concentration. In particular, a) mobility, b) subthreshold swing and c) threshold voltage are shown.*

From these graphs, it is possible to see that a clear trend is present for all molecular weights in the case of the subthreshold swing and threshold voltage, where a higher concentration of polystyrene produces better electric performance (i.e. values closer to zero), especially if we compare the batch with ratio 4:1 with the others. This is not true for the electrical mobility, where a clear tendency is not present, although the 4:1 ratio batch presents better mobilities for all molecular weights with respect to every other composition. In general, these results show that the blending of the organic semiconductor small molecule with polystyrene has an excellent impact on the electric performance of the devices, especially for the figures of merit that are related to the presence of semiconductor-dielectric interfacial trap states (subthreshold swing and threshold voltage). This is in perfect agreement with previous results, where the vertical segregation of the PS at the bottom of the organic semiconducting small molecule film acts as a passivation layer for majority carriers trap states[20,23].

### *4.2.2 Sensitivities*

In Fig. 51, some examples of dynamic X-Ray responses and correspondent sensitivity calculations (for a more detailed description of them, see section 3.6) are provided for every TMTES:PS ratio, in the case of 280 kDa PS molecular weights (the same considerations hold for 100 kDa PS molecular weight, whose dynamic responses can be found in Appendix C).

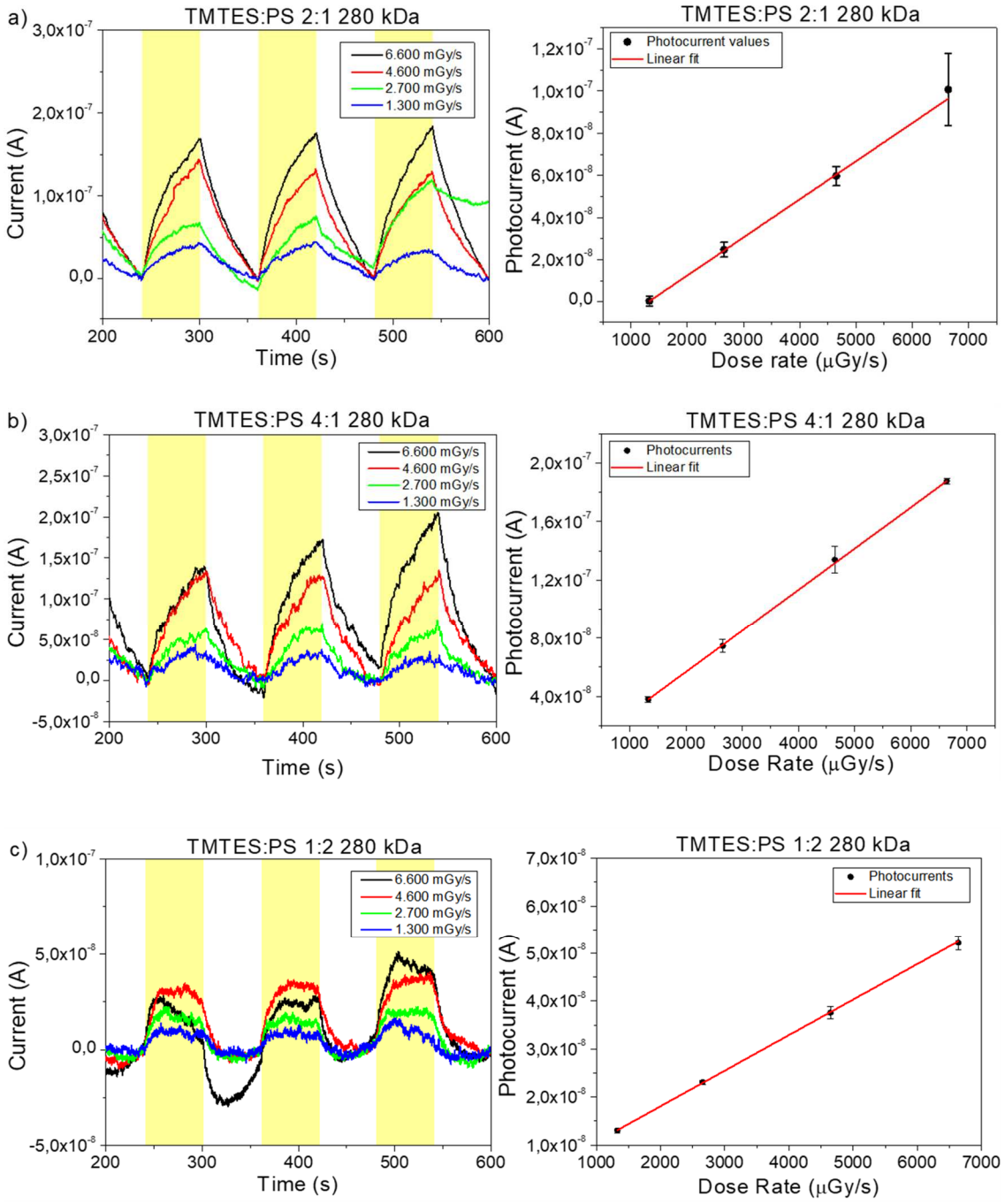


*Fig. 51: From above: a) TMTES:PS 2:1, b) 4:1 and c) 1:2 ratio normalized dynamic response under X-Ray and corresponding sensitivity calculations. In the normalized current graphs, the light-yellow bands indicate the time intervals during which the samples were irradiated. The samples were biased at $V_{SD}$=-10 V and the irradiation cycles last 60 s. Each photocurrent value is the average between three subsequent irradiation cycles in the same conditions and the errors are calculated as the standard deviations.*

These graphs show that the photocurrents follow the expected linear dependence on the dose rate, so that the sensitivity measurements can be evaluated as the slope of the linear fit. By averaging on all the samples analyzed, it is possible to understand the consequences of different TMTES:PS ratios on the OFETs detection performance (Fig. 52).

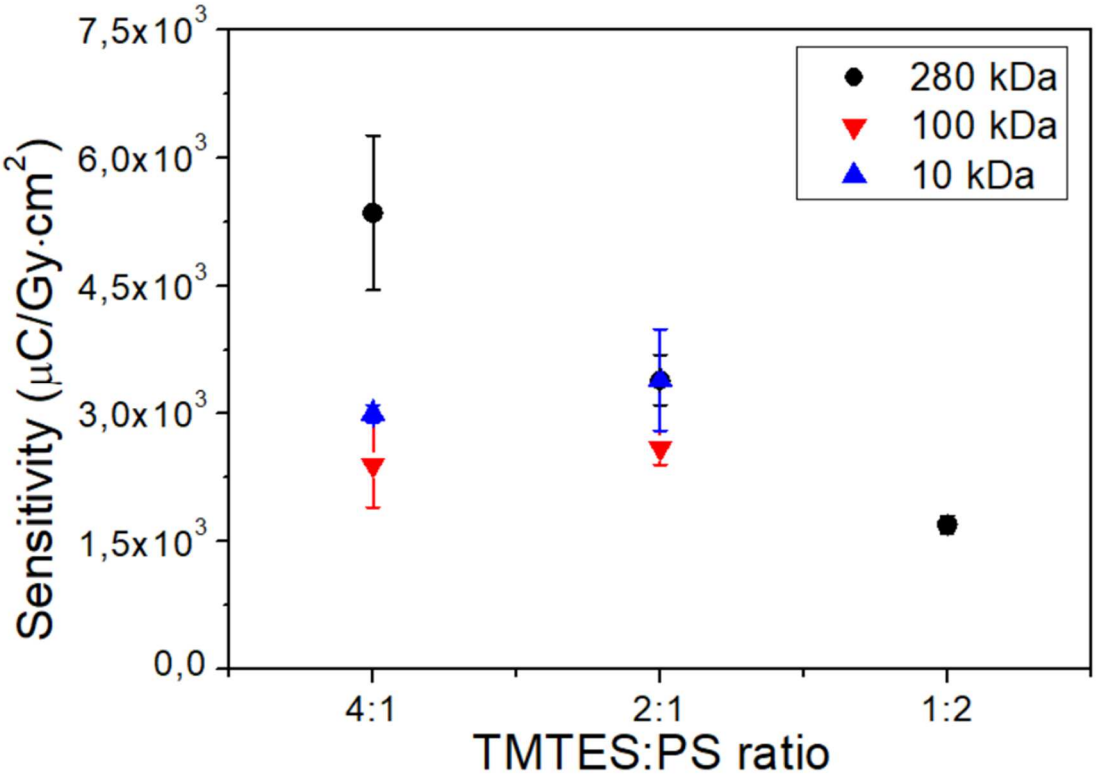


*Fig. 52: Sensitivity values as function of different PS concentrations for three PS molecular weights.*

*The missing values in the 1:2 ratio batch have been already mentioned in section 4.1.*

From this graph, a clear trend can be seen for the 280 kDa PS molecular weight samples: in this case, the sensitivity decreases with increasing PS concentration. Interestingly, this trend was also present in the case of mobility, which may explain effect, since the charge transport properties of a transistor play an important role in the final detection performance, as shown with the kinetic model for organic semiconductors in section 1.5.3.

To deepen the analysis of this trend, we compared the correspondent results obtained by Temiño et at.[20] in 2020 with TIPS-pentacene as active organic small molecule and 280 kDa PS molecular weight (using also the same working conditions, namely $V_G$ = -15 V and $V_D$ = -20 V), normalizing the sensitivities to the respective mobility, in order to account for possible different charge transport properties (Fig. 53).

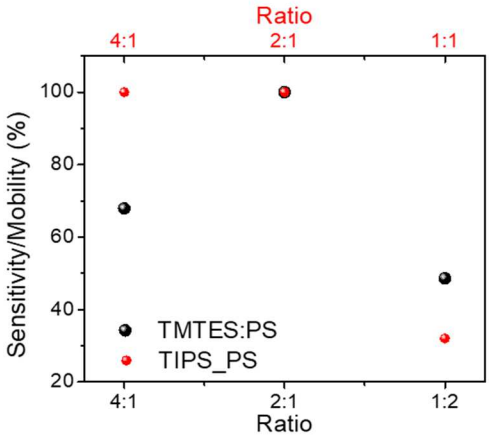


| TIPS:PS | | |
|---|---|---|
| Ratio | Mobility ($cm^2 V^{-1} s^{-1}$) | Sensitivity ($uC Gy^{-1} cm^{-2}$) |
| 4:1 | 0.5±0.2 | 13 × $10^3$ |
| 2:1 | 0.5±0.3 | 13 × $10^3$ |
| 1:1 | 0.06±0.04 | 0.5 × $10^3$ |
| **TMTES:PS** | | |
| Ratio | Mobility ($cm^2 V^{-1} s^{-1}$) | Sensitivity ($uC Gy^{-1} cm^{-2}$) |
| 4:1 | 1.4±0.4 | (44±3) × $10^3$ |
| 2:1 | 0.8±0.2 | (37±14) × $10^3$ |
| 1:2 | 0.8±0.1 | (18±3) × $10^3$ |

*Fig. 53: Percentage comparison between the sensitivity/mobility ratio for TMTES:PS and TIPS:PS blends (left) and the absolute values of sensitivity and mobility (right).*

From this comparison, a different trend appears in the two blends, but with similar percentage variations and with a common worse performance in presence of a high PS concentration (1:2 ratio for TMTES:PS, 1:1 for TIPS:PS). Another meaningful comparison can be realized with the results obtained by Tamayo et al.[23] in the case of TMTES:PS with 280 kDa PS molecular weight: if we use the same polarization conditions ($V_G$ = -15 V and $V_D$ = -20 V) and normalize the sensitivity for the electrical mobility to account for the different transport properties, the results of this work are consistent with the data reported by Tamayo et al. (Fig. 54).

The importance of using the same biases arises from the fact that, according to the photoconductive gain model, the lower gate voltage used in the measurements of this work leads to a smaller charge carrier density in the conductive channel, which in turn lowers the recombination time term in the gain factor G. Similarly, a lower drain voltage results in a smaller driving force and a weaker photo-generated charges collecting field, with an impact on the final sensitivity.

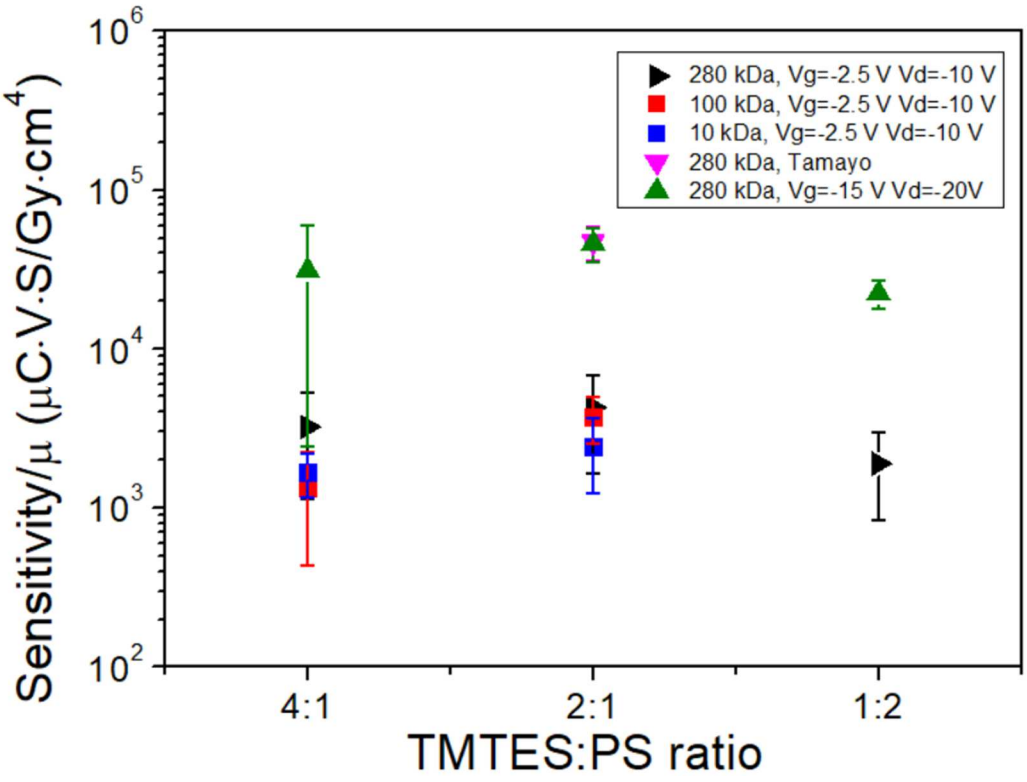


*Fig. 54: Comparison of the result of this work with previous ones in the case of the ratio sensitivity/mobility. It is possible to see that using higher polarizations, the sensitivity increases (an ordinary effect, widely documented in literature) and that, accounting for the different mobility values, this work is consistent with the results by Tamayo et al.: for a TMTES:PS ratio at 2:1, irradiated in the same conditions, these quantities are completely comparable.*

### *4.3 Role of polystyrene molecular weight*

The main difference between this work and the previous studies that have been carried out about blended organic active layers for ionizing radiation detectors is that also the molecular weight of the polystyrene was varied, and not just the volume ratio between the active small-molecule and the inert polymer that constitutes the blend. Therefore, the influence of different PS molecular weights on both the electrical parameters and the detection performance is shown and discussed in the following section.

#### *4.3.1 Electrical parameters*

As it was done for the section 4.2.1, we report the output and transfer characteristics of the devices based on the blended TMTES:PS and of a pure TMTES layer without polystyrene (Figg. 55-56) This shows the impact of the presence of polystyrene on the electric performance of the OFETs confirming the role of the PS in passivating the traps at the interface with the dielectric as it was previously reported in literature[20,23].

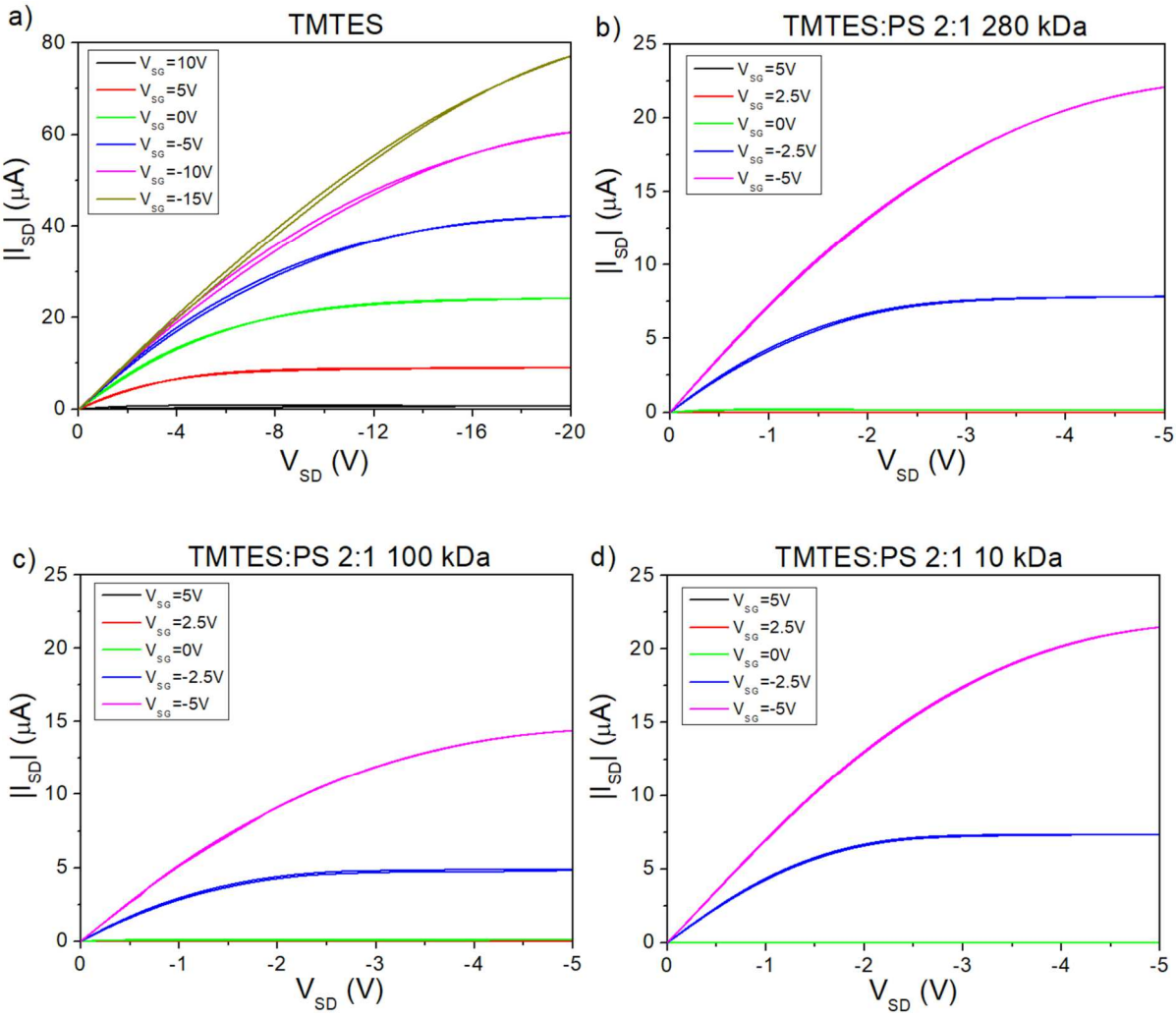


*Fig. 55: a) pure TMTES; b) 280 kDa; c) 100 kDa and d) 10 kDa PS molecular weight output characteristics. All reported characteristics are taken from devices with 2:1 TMTES:PS ratio, but the same trend is present for 4:1 and 1:2 ratios. From these graphs it is possible to see that the working point used to evaluate the sensitivities ($V_G$=-2.5V and $V_D$=-10V) of the blended sample is in the saturation regime.*

From these graphs, it is possible to see that, except for the already discussed difference between pure TMTES samples and blended ones, distinct PS molecular weights do not produce any clear variation in the output characteristics of the OFETs.

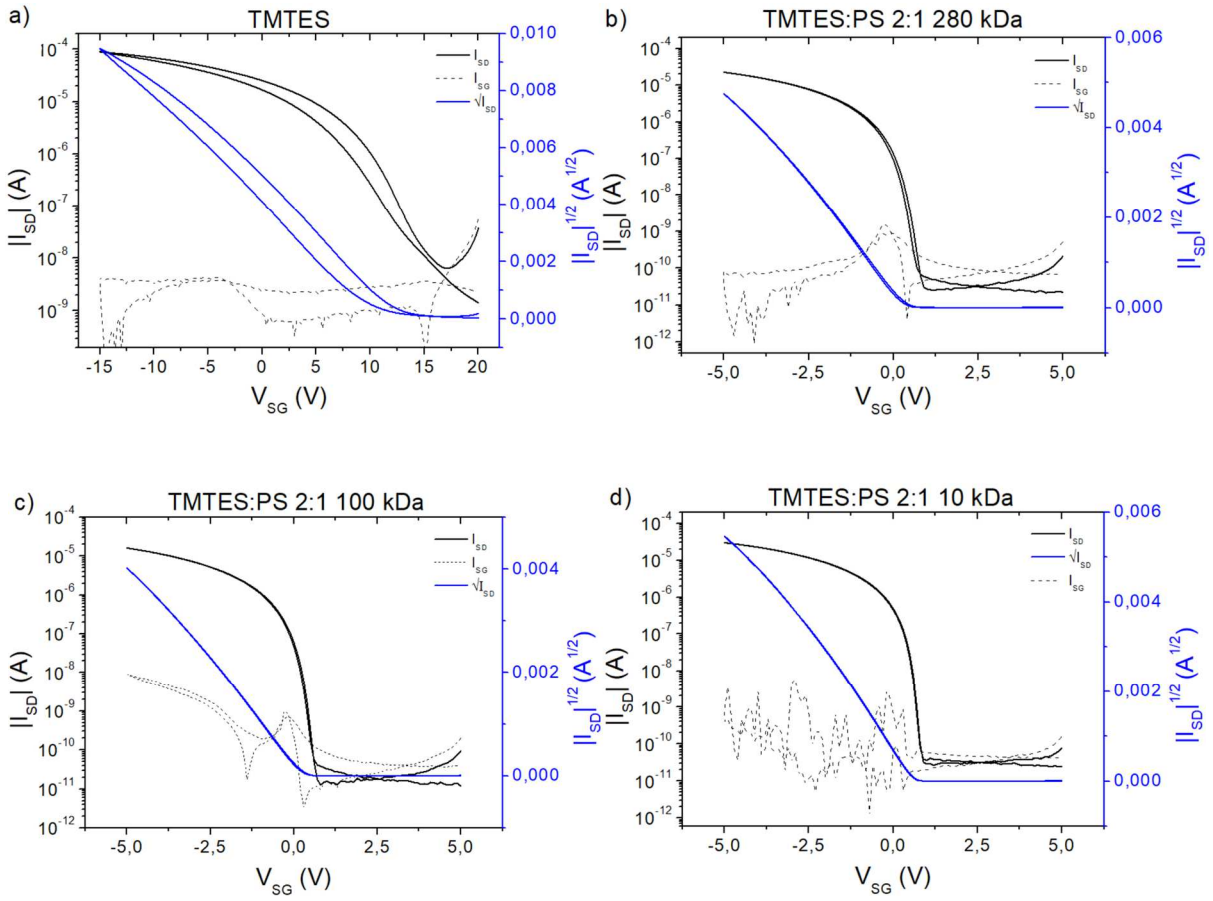


*Fig. 56: a) pure TMTES; b) 280 kDa; c) 100 kDa and d) 10 kDa PS molecular weight transfer characteristics. The dashed line represents the leakage current. All samples were measured with $V_D$=-10V. All reported characteristics are taken from devices with 2:1 TMTES:PS ratio, but the same trend is present for 4:1 and 1:2 ratios.*

In this case as well, no relevant impact can be ascribed to the presence of polystyrene with different molecular weights: also from the evaluation of the influence of this other parameter of the active blend, the strongest difference in the transfer characteristics is the positive role of polystyrene in the lowering the non-ideality effects such as hysteresis and trap states, as well as in the reduction of the leakage current. Therefore, a confirmation of the benefits coming from the use of a blended active layer can be deduced from the comparison between distinct polystyrene molecular weights as well.

In conclusion, the quantitative results of the variation of molecular weight on the electric parameters are shown in Fig. 57.

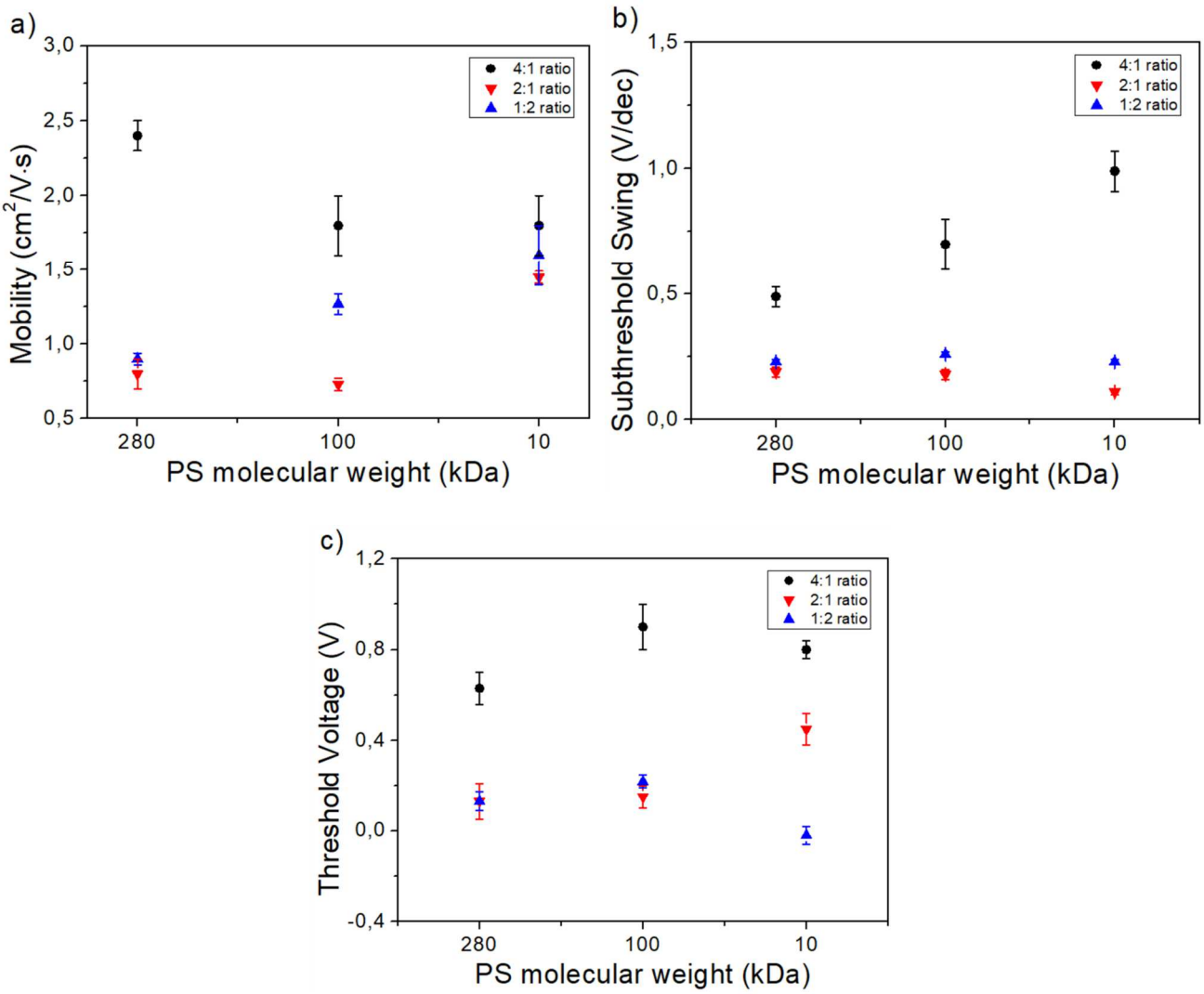


*Fig. 57: Electric parameters with different PS molecular weights. In particular, a) mobility, b) subthreshold swing and c) threshold voltage are shown*

From these graphs, it is not possible to recognize any trend with the molecular weight: indeed, the only considerations that can be derived are a result of those formulated in section 4.2.1, namely the higher values of the 4:1 ratio batch for every figure of merit and a certain similarity between the 2:1 and 1:2 ratio batches (in many cases, their electric parameters overlap). In other words, we can conclude that the employment of different PS molecular weights does not seem to have a meaningful impact on the electric performance of the OFETs.

### *4.3.2 Sensitivities*

In Fig. 58, some examples of normalized currents and correspondent sensitivity calculations are provided for every PS molecular weight, in the case of 2:1 TMTES:PS ratio (the same considerations hold for the ratio 4:1, whose normalized currents and sensitivity calculations can be found in Appendix C. In the case of ratio 1:2 just one sensitivity was calculated clearly, so that its results are not shown).

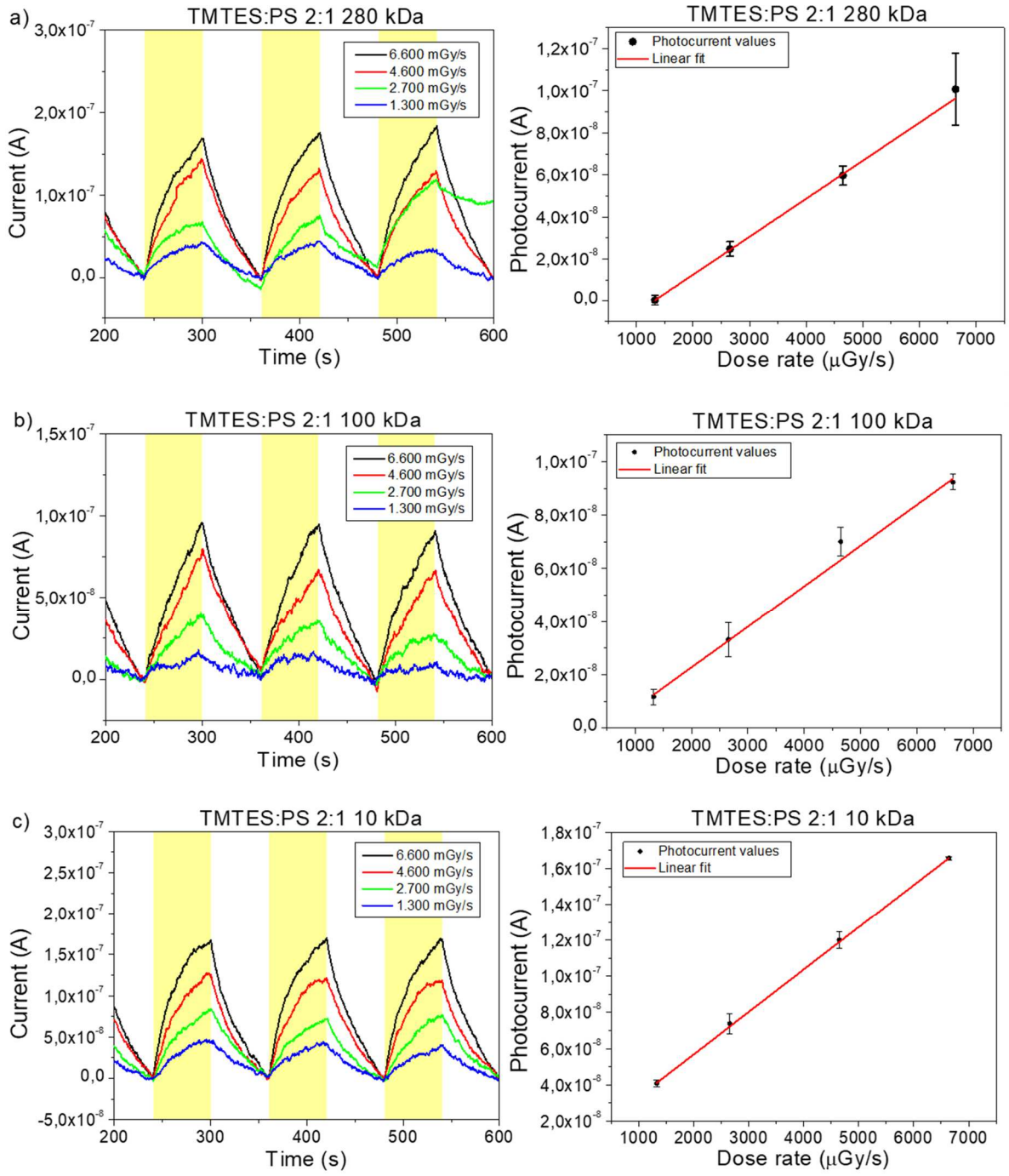


*Fig. 58: From above: a) 280 kDa, b) 100 kDa and c) 10 kDa PS molecular weight dynamic response under X-Rays and corresponding sensitivity calculations. In the normalized current graphs, the light-yellow bands indicate the time intervals during which the samples were irradiated. The samples were biased at $V_{SD}$=-10 V and the irradiation cycles last 60 s. Each photocurrent value is the average between three subsequent irradiation cycles in the same conditions and the errors are calculated as the standard deviations.*

These graphs confirm that the photocurrents follow the expected linear behaviour from which it is possible to derive the sensitivity of the sample as the slope of the linear fit. If we consider the average on all the devices that worked properly under test, we can plot the dependence of the sensitivity on the molecular weight of PS for all TMTES:PS ratios (Fig. 59).

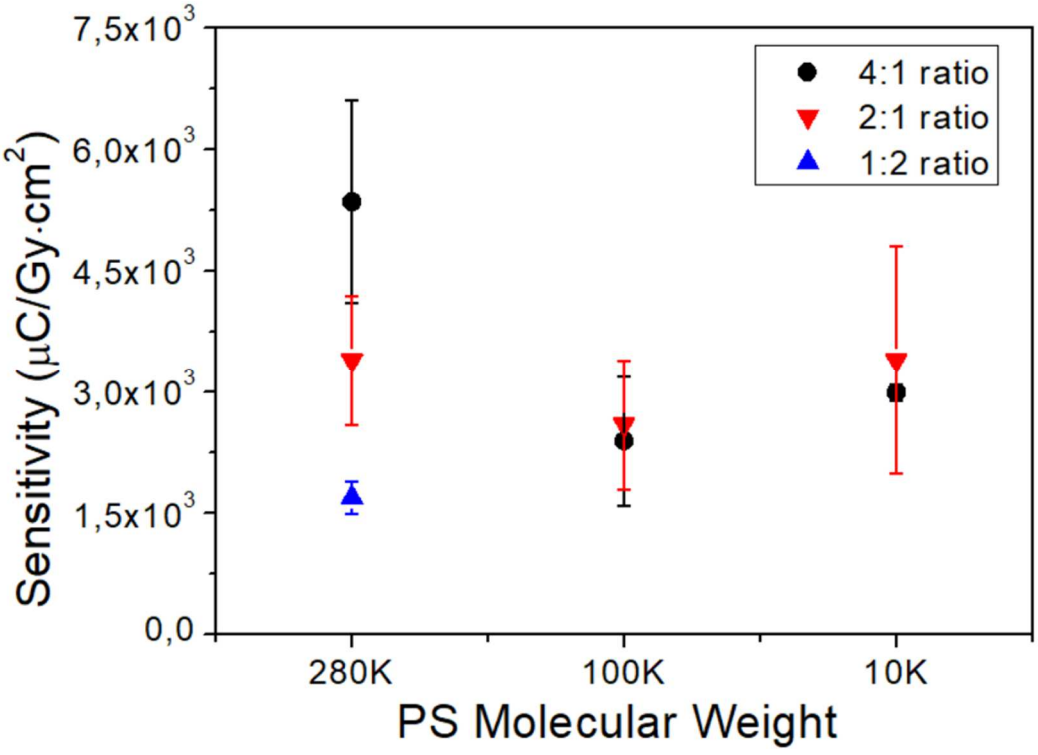


*Fig. 59: Sensitivity values as function of different PS molecular weights for every TMTES:PS ratio tested. The missing values in the 1:2 ratio batch have been already discussed in section 4.1.*

This graph shows no evidence of a relevant trend of the sensitivity with the molecular weight of polystyrene: indeed, most values are comparable and wherever considerable differences are present they follow the mobility behaviour (Fig. 57), indicating that sensitivity fluctuations are mainly due to slightly different transport properties. In other words, if we account for the diverse mobilities that are present in the sample, we can conclude that changing the molecular weight of the polymer that constitutes the active blend does not seem to play a major role on the final detection performance.

### *4.4 ToF-SIMS*

In the following, the results of the ToF-SIMS analysis performed at the University of Roma Tre are presented and discussed together with the data coming from the electrical and X-ray characterizations performed in Bologna.

Since in previous sections no proof of an impact of the PS molecular weight was found neither in the transport properties nor in the X-ray detection sensitivity, we focused mainly on the 280 kDa samples, which is the most reported in literature so far.

The ToF-SIMS depth profiles (Fig. 60) clearly show the vertical segregation of the PS for all the three ratios which induce a passivation of the interface between the dielectric and the semiconducting layer and improve the electrical parameters of the OFETs based on the blend with respect with the ones based on the pure TMTES.

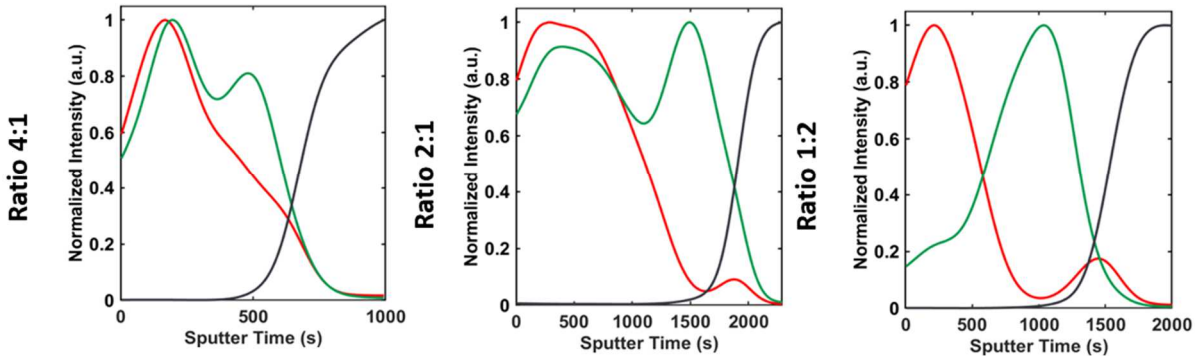


*Fig. 60: ToF-SIMS depth profiles for different TMTES:PS ratios. The black, green, and red lines refer to the substrate, PS and TMTES, respectively. From them, it is possible to see that the phase segregation takes place in all three cases.*

The fact that the semiconductor/dielectric interface is passivated by the segregated PS in all three cases can be seen also from the calculation of the interfacial trap states, where the reduction of trap density with the addition of PS is clear and comparable independently on the TMTES:PS ratio (and PS molecular weight), as depicted in Fig. 61.

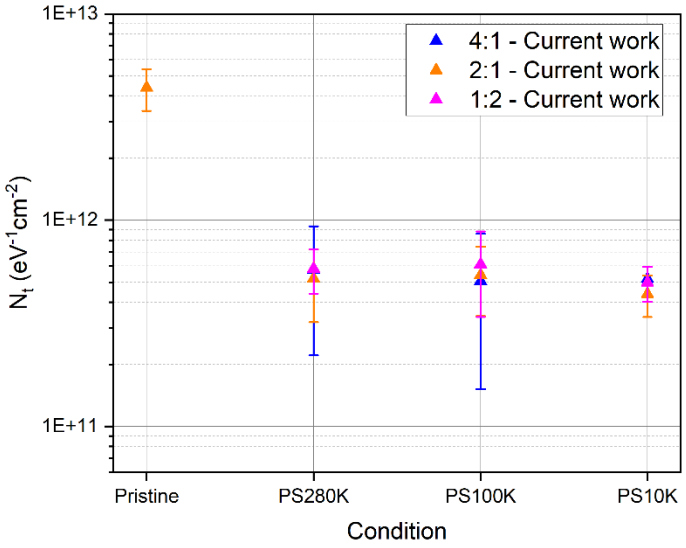


*Fig. 61: Interfacial trap states density for different TMTES:PS ratios and PS molecular weights.*

In Fig. 62 we also report the optical microscope and the ToF-SIMS surface analysis for the pure TMTES based OFET and the three different blend ratios.

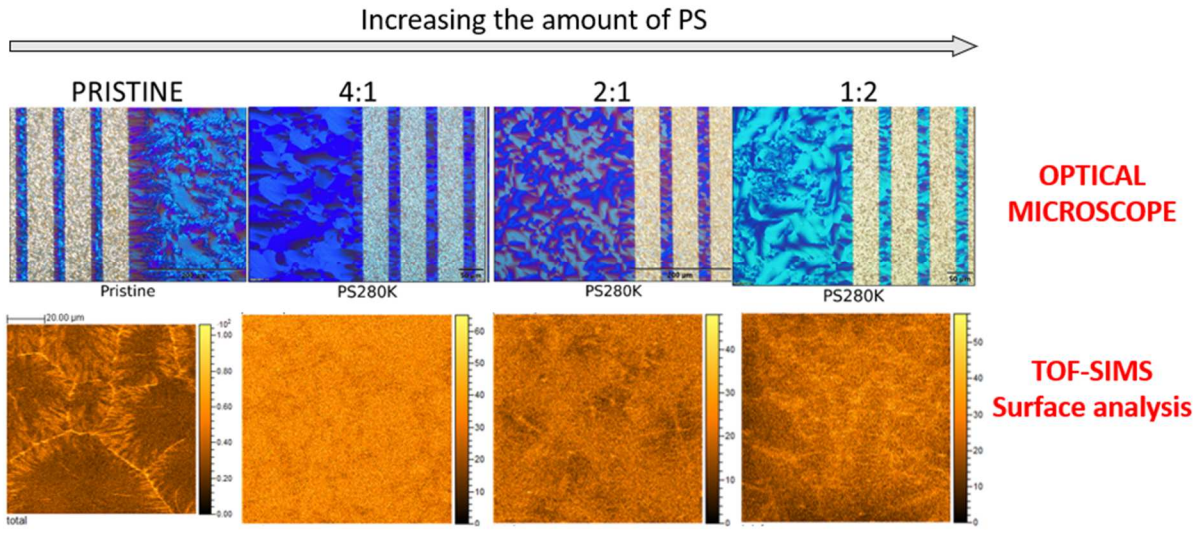


*Fig. 62: Optical microscope and ToF-SIMS analysis for different TMTES:PS ratios.*

From these images, it is possible to see that the absence of PS produces negative effects in the crystallization process, with the presence of the highest amount of grain boundaries and with the formation of a non-homogeneous film. But also, the presence of PS affects the uniformity and crystallization of the active layer in different ways depending on the amount of polymer: increasing the quantity of PS brings a worsening of the uniformity of the film and a degradation of the crystallization process of the organic semiconducting thin film. This worsening of the crystallization process due to the increasing amount of PS can strongly affect the quality of the semiconducting layer properties and can be the main reason for the decrease of mobility and sensitivity already discussed in section 4.2.2 (Fig. 63).

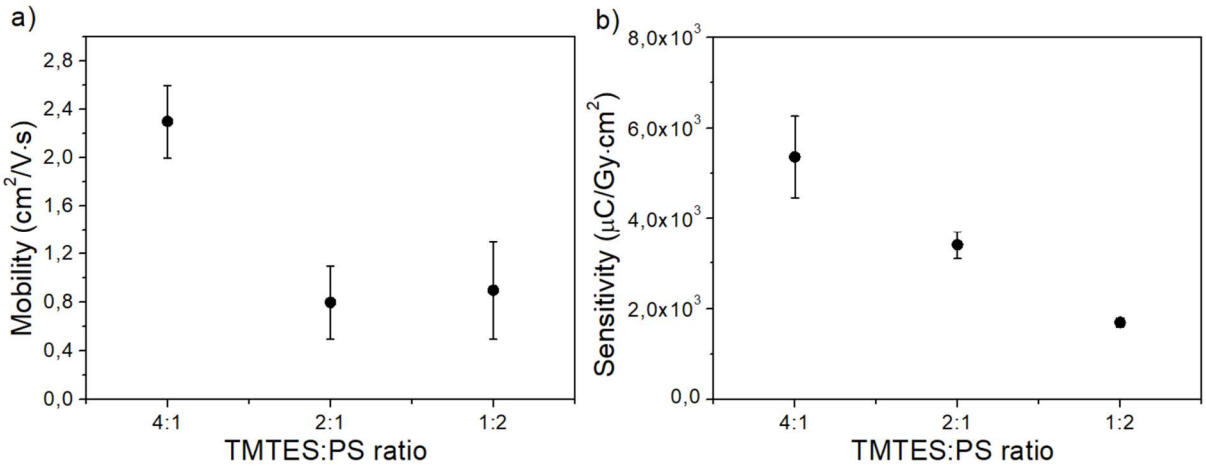


*Fig. 63: a) Mobility and b) sensitivity values as function of different PS concentrations for 280 kDa PS molecular weight. The negative impact of a high PS concentration appears clearly.*

These results clarify that a small amount of polystyrene is enough to passivate the traps for majority carriers at the dielectric/semiconductor interface, and that an excess of the polymer can worsen the transport properties of the devices. Since the best performances were measured in the case of the lowest PS concentration, a possible strategy to further improve the electric and X-ray detection efficiencies could be to try an even lower amount of polystyrene, in order to find the best ratio at which this polymer can perform at its best.

### *4.5 Encapsulation layer study*

In the following, the main results regarding the role played by the parylene passivation layer in the electrical and detecting performances of the devices are reported and discussed (for batch P7500). In the case of parylene-coated samples, we present the mean values of all samples, since they show high homogeneity good level of reproducibility of the devices functionalities. On the other hand, unencapsulated samples showed very different behaviours, and the mean values of every substrate will be provided separately (Tab. 5).

| Sample | μ ($cm^2 \cdot V^{-1}s^{-1}$) | $V_{Th}$ (V) | SS (V/dec) | Sensitivity ($\mu C \cdot Gy^{-1}cm^{-2}$) $\bullet 10^3$ |
|---|---|---|---|---|
| Parylene | 2.3±0.1 | 1.7±0.1 | 1.8±0.1 | 13.7±0.9 |
| No parylene | 2.6±0.1 | 1.1±0.2 | 0.8±0.2 | 6.9±2 |
| Sample5 | 2.8±0.1 | 1.1±0.2 | 0.8±0.2 | 11.3±0.3 |
| Sample6 | 2.43±0.07 | 1.0±0.1 | 0.7±0.1 | 2.4±0.2 |
| Sample7 | 2.29±0.08 | 1.1±0.1 | 0.8±0.1 | Discharge |
| Sample8 | 2.76±0.07 | 1.4±0.4 | 0.6±0.1 | 5±3 |

*Tab. 5: Electrical and X-ray characterization results. Reported values are the average for all the devices for every composition, and the associated error is the standard deviation. Samples cells from 5 to 8 contain the mean values of the 4 transistors that were deposited on a common substrate, since they showed common features. Sample6 sensitivity was extracted from just one sample, so that the associated error is its own one.*

### *4.5.1 Electrical parameters*

First, we report the output and transfer characteristics in saturation regime of the devices both for the case of a parylene-coated sample and for a no-encapsulated one (Figg. 64-65).

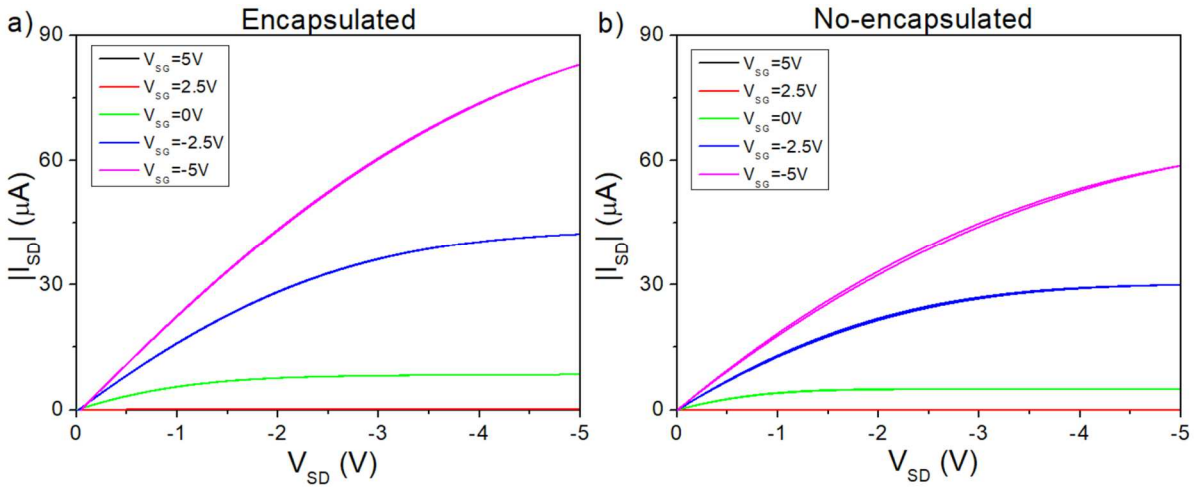


*Fig. 64: Encapsulated (left) and unencapsulated (right) output characteristics.*

It is easy to see that the output characteristics are very similar in both cases, and the presence of an encapsulating layer does not affect the electric performances of the OFETs.

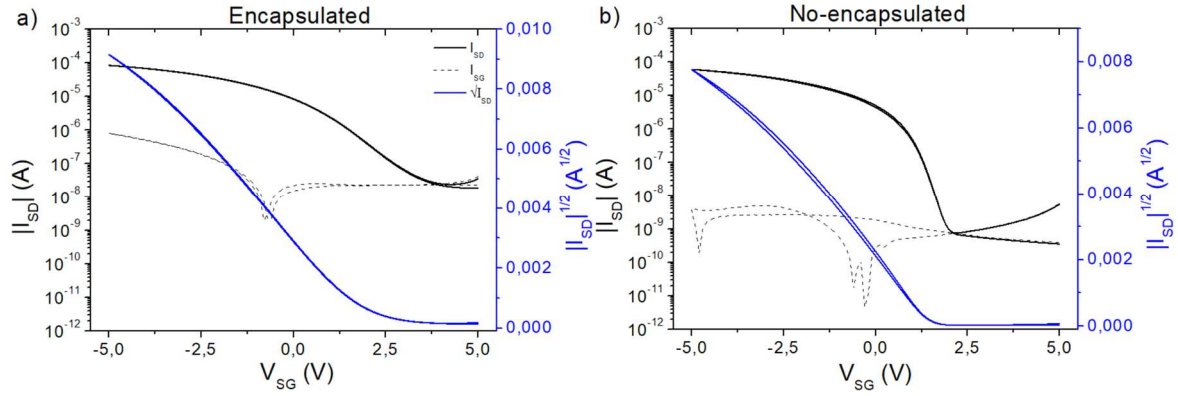


*Fig. 65: a) Encapsulated and b) not encapsulated transfer characteristics in saturation regime. The dashed lines represent the leakage current. All samples were measured with $V_D$=-10V.*

In this case, an important difference is present between the two different groups of samples: in the case of parylene-coated devices, the leakage current and the off current are remarkably high (by one or two orders of magnitude higher than no-encapsulated OFETs). This results in worse electrical parameters in coated samples (as it is possible to see in Tab. 5, mainly in the case of the subthreshold swing and threshold voltage). These figures of merit, together with the not negligible number of not working perylene devices, may be an effect of the final step of the parylene deposition technique that was used during the fabrication of this batch: as reported in section 3.3.2, the pads that allow to connect the gate electrode of the devices were scratched in order to remove the insulating parylene layer, and this could have induced damages, causing leakages and, at the worst, the breakdown of the transistor. An improvement of this step of fabrication is needed to obtain better devices.

***Recovery test***

The main goal of the recovery test that was performed on three different kind of samples was to evaluate the evolution of the electric parameters of the devices after a prolonged period of functioning under radiation. This experiment was performed on three OFETs: S1O2 and S4O1 from batch P900 and S2O2 from batch P7500, covered with no encapsulation, 900 nm and 7500 nm parylene layers respectively. Every transistor underwent multiple electric characterizations: 20 curves were taken before the irradiation, 60 with X-rays on and 120 after the irradiation. Every transfer was analyzed with the same scripts that were employed in the other analyses.

The transfer characteristics of the devices tested before and after the irradiation sessions are shown in Fig. 66.

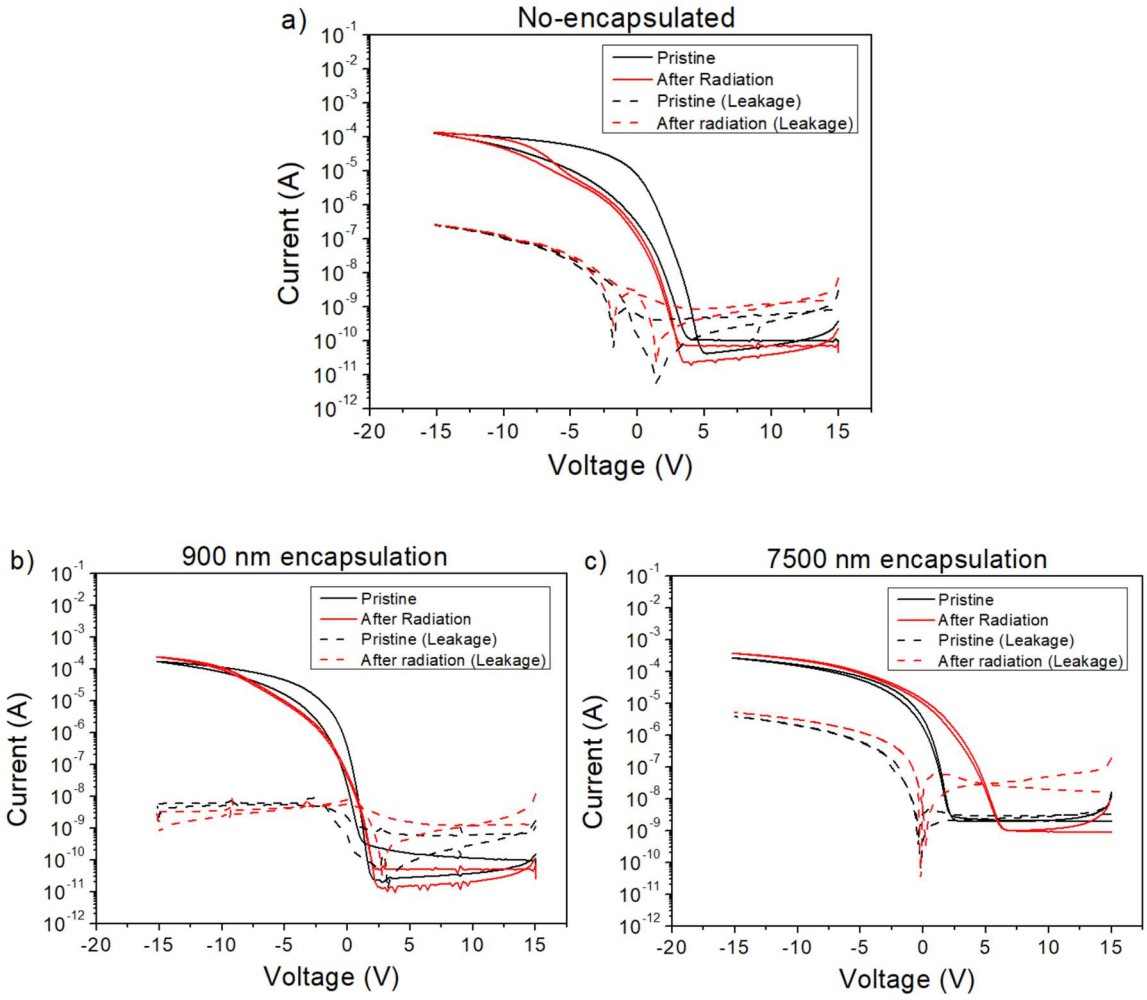


*Fig. 66: Transfer characteristics of devices tested during the recovery test. The dashed lines represent the leakage currents. All samples were measured with $V_D$=-20V, and after the irradiation they had absorbed 23.8 Gy.*

From these graphs, the wide hysteresis of the not encapsulated sample (S1O2) before receiving radiation appears clearly, but it fades away after the irradiation. This behaviour is common to all the studied devices, but in encapsulated samples the pristine transfer curve shows less hysteresis, especially in the case of 7500 nm. On the other hand, leakages currents are rather high in all samples but S4O1, and do not show appreciable variations after irradiation.

In addition, the electric parameters of all the collected transfer characteristics were calculated for the no-encapsulated and the 900 nm encapsulated samples, and their results are shown graphically in Fig. 67.

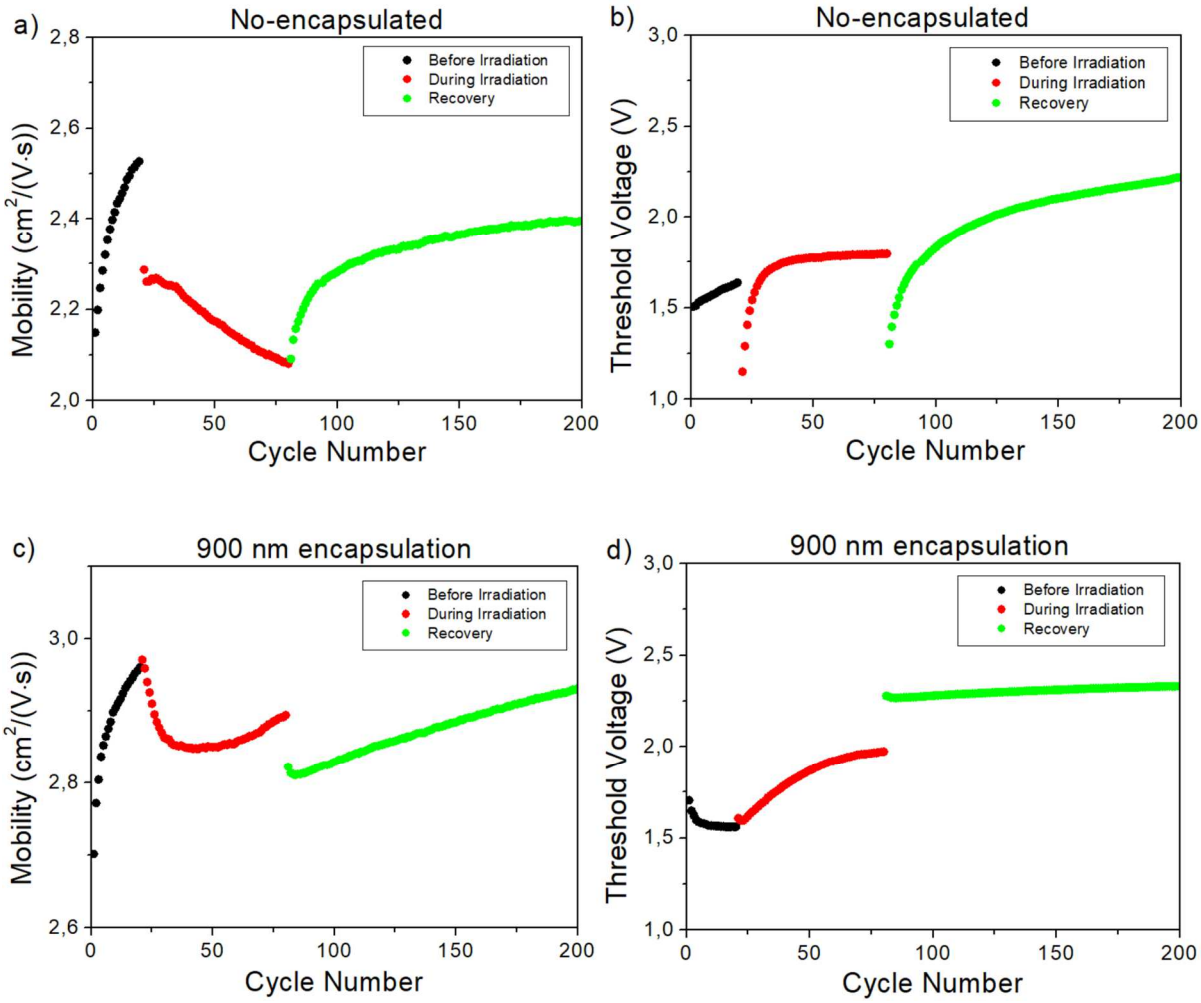


*Fig. 67: From above: unencapsulated (a, b) and 900 nm encapsulated (c, d) samples mobilities (left) and threshold voltages (right) throughout the recovery test.*

From these results, it is possible to see that encapsulated device shows more stable parameters: Also, after every part of the recovery test, the encapsulated device tends to keep the last value showed, while the no-encapsulated device presents a recovery to the initial value for the electric parameters. As a consequence, it is possible to hypothesize that the presence of an encapsulation layer introduces a sort of *memory* in the transistors maintaining the variation induced by the x-rays for roughly 120 minutes after the irradiation. However, other investigations are needed to reach a better understanding of this complex phenomenon and to solidify the interpretation of these results.

### *4.5.2 Sensitivities*

In Fig. 68, we provide some examples of dynamic photocurrent curves before and after the normalization for both encapsulated and no-encapsulated samples. Since the substrates from 5 to 8 of batch 20230412 (unencapsulated) show very low level of homogeneity in their current curves, the comparison between the presence and absence of an encapsulating layer was evaluated with batch MW21 (sharing the same composition as with parylene coated samples, but a worse mobility) and with batch MW41 (with a different TMTES:PS ratio, but with similar transport properties).

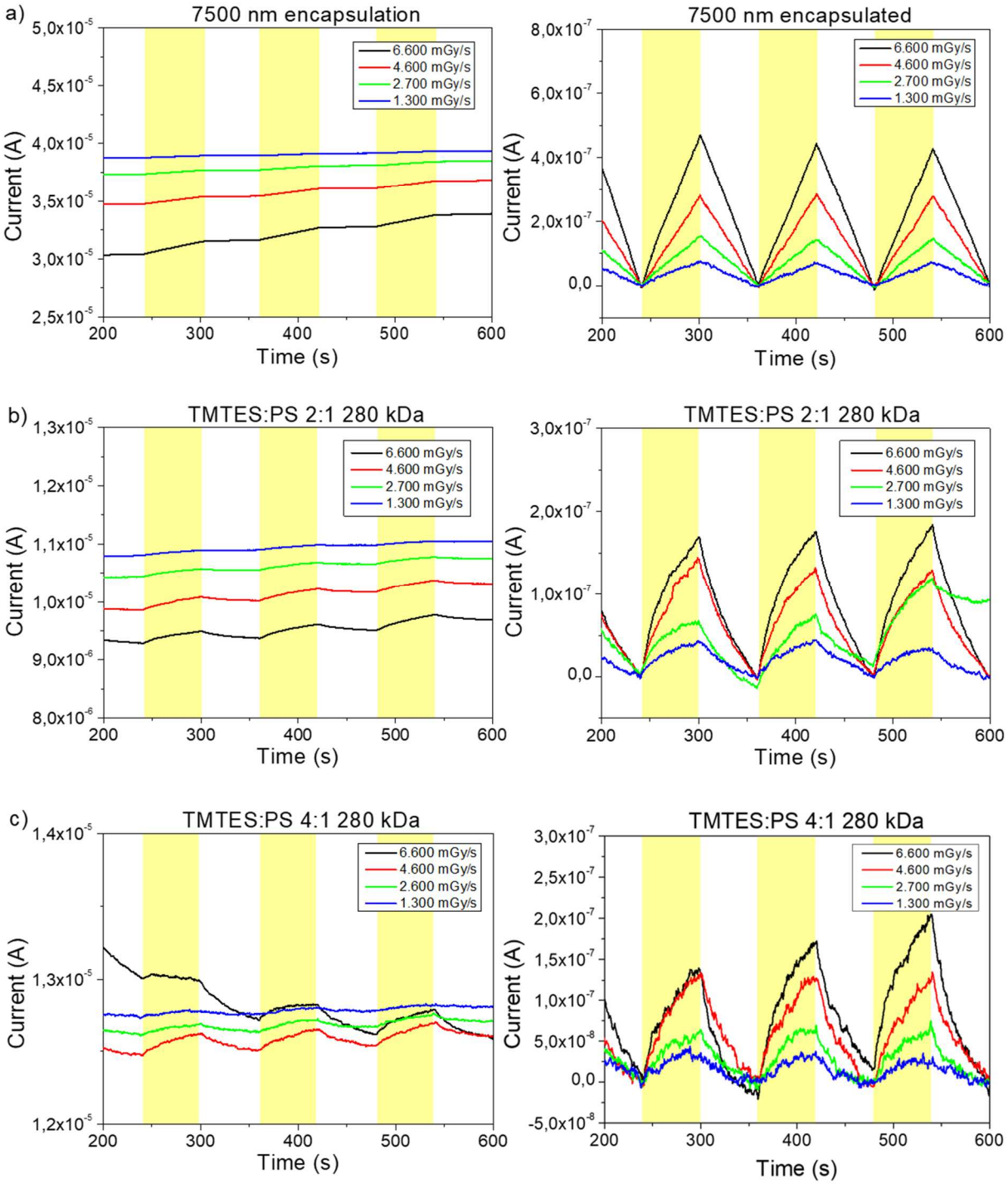


*Fig. 68: From above: a) encapsulated, b) batch MW21 and c) batch MW41 280 kDa molecular weight samples. On the left, it is possible to see the current curves before the normalization, while on the right the normalized currents are shown. The samples were biased at $V_{SD}$=-10 V and the irradiation cycles last 60 s. The light-yellow bands indicate the time intervals during which the samples were irradiated.*

From these graphs, an important difference can be readily seen: the shapes of the curves are much different for parylene samples. Indeed, not normalized currents tend to increase as they are exposed to X-rays, and to recover the pristine value when the radiation is shut down. This is not the case of parylene coated devices, where the current shows longer relaxation time and in the 60 second after the irradiation cycles it stays almost constant. This *integrating* behaviour could be explained by the presence of trapped minority charges in the parylene layer or at the interface between parylene and semiconductor that provokes a persistent doping of the OFET channel and enlarges the relaxation time of the device, and is in good agreement with the findings of the recovery test that were discussed previously. In addition, the presence of parylene is associated with a higher sensitivity, also accounting for the better transport properties that the encapsulated samples and the 4:1 ratio batch show (Tab. 6).

| Sample group | μ ($cm2 \cdot V^{-1}s^{-1}$) | Sensitivity ($\mu C \cdot Gy^{-1}cm^{-2}$) $\bullet 10^3$ | S/μ ($\mu C \cdot V \cdot s \cdot Gy^{-}1 \cdot cm^{-4}$) |
|---|---|---|---|
| Encapsulated | 2.3±0.1 | 13.7±0.9 | 6.0±0.7 |
| 2:1 ratio | 0.8±0.1 | 3.4±0.3 | 4.3±0.9 |
| 4:1 ratio | 2.4±0.1 | 5.4±0.9 | 2.3±0.5 |

*Tab. 6: Electrical and X-ray characterization results for encapsulated samples and batches MW21 and MW41. Reported values are the mean ones for 280 kDa PS molecular weight, and the associated error is the mean standard deviation (or error propagation in the case of the last column. It is possible to see that encapsulated samples show the best sensitivity/mobility ratio.*

Considering the photoconductive gain kinetic model that was cited in the first chapter, it is possible to analyze the shapes of the current curves more in detail. Indeed, a characteristic time study can be performed starting from the sensitivity values, the transport properties and the geometric features of the devices under test (next section).

### *4.5.3 Characteristic times study*

Recalling Eqq. 6-7-8 and the operative definition of sensitivity, this last figure of merit can be used to gather information about the characteristic times of different devices. In our case, the comparison will be performed between the encapsulated samples and the no-encapsulated one (280 kDa PS molecular weight MW41 batch). Looking at the electrical mobility values reported in Tab. 5, the transport properties and $I_{CC}$ of the two can be assumed comparable. In addition, the geometric features and the applied bias were the same in all measurements. Therefore, the transit time differences are only due to the mobility values of the samples. This way, it is possible to use the mobility of the sample together with their sensitivities to find an estimation of the ratio between the two relaxation times which is the main parameters that affect the recovery process after the irradiation cycles (Eq. 16).

$$\frac{Sensitivity_{encapsulated}}{Sensitivity_{no-encapsulated}} = \frac{\tau r_{encapsulated}}{\tau r_{no-encasulated}} \times \frac{\mu_{encapsulated}}{\mu_{no-encapsulated}} \qquad [16]$$

Considering the ratios between the sensitivity values and mobility values reported in Tab. 5, we can calculate the ratio between the recombination time of the parylene-coated sample and no-encapsulated one which results $\tau r_{encapsulated} / \tau r_{no\text{-}encapsulated} = 2.6 \pm 0.8$. This result indicated that the addition of a parylene encapsulation layer enlarges the relaxation time of the detector increasing the gain of the detecting signal and consequently the final sensitivity. This is probably due to the introduction of new trap states for minority carrier which increase the relaxation time and thus the photoconductive gain effect.

# *Conclusion*

In this work, the effects of different TMTES:PS volume ratios and polystyrene molecular weights in the active blend of OFETs on the electric and X-rays detection performances were studied.

The impact of the volume ratio between the active molecule and the polymer confirmed the results obtained in previous works conducted onto other materials, with better performances (both electrical and under X-ray) in the case of low amounts of polystyrene (4:1 and 2:1), while the variation of the polystyrene molecular weight showed no particular influence on the performances of the devices. Thanks to a ToF-SIMS analysis carried out at the University of Roma Tre, it was possible to assess the phase separation of TMTES and polystyrene in all the batches with different ratios, providing an additional proof of the fact that a small amount of this polymer is enough to create a passivation layer for majority carrier trap states at the interface with the dielectric improving the electrical performances of these devices.

In addition, the consequences of the use of an encapsulation layer on top of the OFETs have been evaluated, both in the electric parameters and in the impact on the X-rays detection sensitivity: encapsulated samples showed good transport properties, with $\mu=2.3\pm0.1$ $cm^2 \cdot V^{-1}s^{-1}$, comparable to the highest value for unencapsulated samples ($\mu=2.3\pm0.1$ $cm^2 \cdot V^{-1}s^{-1}$, in the case of 280 kDa molecular weight and 4:1 ratio samples). Also the sensitivity reached the highest recorded value among the tested batches ($S=(13.7\pm0.9)\cdot 10^3$ $\mu C \cdot Gy^{-1}cm^{-2}$). Accounting for the high mobility, the top sensitivity can be traced back to the presence of minority carriers trap states introduced by the addition of the parylene-C encapsulation layer; indeed, according to the kinetic model for the photoconductive gain effect, the relaxation time doubled compared with analogous devices not encapsulated, meaning that the charge carriers recombination time is remarkably higher when parylene is added. In the case of the electric parameters, the addition

of a parylene layer can be associated with a higher stability and with the tendency to retain the values of the electric parameters over time after irradiation.

These results provide a better understanding of the organic blends employed as active layer in X-ray detectors based on OFETs and open new possibilities to better match the active molecules and the blending polymer feature. On the other hand, the study of the encapsulation layer provides an insight on the impact of an additional layer on this kind of devices, which in turn can lead to new ways of improving their resistance to degradation and their integrative response over time.

# *Appendix A*

The extraction of the electric parameters from the transfer curve of an OFET is realized starting from the mobility value: this figure of merit is obtained as the highest slope value calculated from the fit of a fixed number of consecutive current data, which is decided *a priori* in light of the voltage step of the measurement. Once the mobility is determined, the slope and the intercept used are also employed to find the threshold voltage from the same regression line. The subthreshold swing is calculated using the same principle as the mobility, once the data have been turned into a logarithmic scale. In all cases, the electric parameters are determined from the forward sweeps (no major differences are present between the two sweeps, so that this decision has been taken in order to follow a common protocol).

The photocurrent normalization was performed selecting the current data recorded at 240, 360, 480 and 600 seconds after the beginning of the measurement and performing a parabolic fit. The parabola was subtracted to the measured current to obtain the normalized currents, from which the photocurrents are derived. In those cases where the normalized currents showed low noise, the photocurrent calculation was carried out using a script to obtain every photocurrent and provide the mean value with its semidispersion, from which the sensitivity was calculated (and shown in graphs) in OriginLab. In some samples, the normalized currents were very noisy and the photocurrents were determined manually, since writing a script to get rid of the unwanted fluctuations would have been hard to realize and the efforts would have overwhelmed any benefit.

# *Appendix B*

In the following, the average values of all samples characterized in this work are reported in a table for every batch (MW21, MW41, MW12 and P7500). The reported parameters are the average values for every sample, and the associated error is the mean standard deviation (unless just one value is present, in which case the error is its own one).

| Sample, molecular weight | μ ($cm^2 \cdot V^{-1}s^{-1}$) | $V_{Th}$ (V) | SS (V/dec) | Sensitivity ($\mu C \cdot Gy^{-1}cm^{-2}$) $\bullet 10^3$ |
|---|---|---|---|---|
| S11, 280 kDa | 0.9±0.2 | -0.08±0.04 | 0.17±0.01 | 3.3±0.5 |
| S12, 280 kDa | 0.8±0.2 | 0.29±0.09 | 0.20±0.02 | 2.4±0.6 |
| S17, 100 kDa | 0.65±0.02 | 0.2±0.2 | 0.22±0.05 | 2.4±0.2 |
| S18, 100 kDa | 0.81±0.03 | 0.15±0.06 | 0.14±0.01 | 2.8±0.3 |
| S23, 10 kDa | 1.37±0.03 | 0.23±0.08 | 0.10±0.01 | 3.5±0.7 |
| S24, 10 kDa | 1.55±0.08 | 0.5±0.1 | 0.12±0.02 | 2.0±0.6 |

*Table B-1: Electrical and X-ray characterization results for batch MW21.*

| Sample, molecular weight | μ ($cm^2 \cdot V^{-1}s^{-1}$) | $V_{Th}$ (V) | SS (V/dec) | Sensitivity ($\mu C \cdot Gy^{-1}cm^{-2}$) $\bullet 10^3$ |
|---|---|---|---|---|
| S5, 280 kDa | 2.3±0.2 | 0.56±0.08 | 0.43±0.07 | 4.1±0.2 |
| S6, 280 kDa | 2.5±0.1 | 0.70±0.05 | 0.56±0.05 | 9.1±0.1 |
| S11, 100 kDa | 1.33±0.09 | 1.2±0.1 | 1.1±0.1 | 2.1±0.6 |
| S12, 100 kDa | 2.3±0.1 | 0.63±0.04 | 0.37±0.03 | 3.0±0.3 |
| S17, 10 kDa | 2.1±0.4 | 0.86±0.06 | 0.9±0.1 | Negative |
| S18, 10 kDa | 1.6±0.1 | 0.76±0.05 | 1.07±0.03 | 3.0±0.1 |

*Table B-2: Electrical and X-ray characterization results for batch MW41.*

| Sample, molecular weight | μ ($cm^2 \cdot V^{-1}s^{-1}$) | $V_{Th}$ (V) | SS (V/dec) | Sensitivity ($\mu C \cdot Gy^{-1}cm^{-2}$) $\bullet 10^3$ |
|---|---|---|---|---|
| S5, 280 kDa | 0.98±0.5 | 0.23±0.4 | 0.21±0.01 | 1.6±0.1 |
| S6, 280 kDa | 0.83±0.03 | 0.03±0.01 | 0.25±0.01 | 1.8±0.2 |
| S11, 100 kDa | 1.3±0.1 | -0.2±0.1 | 0.26±0.02 | Negative |
| S12, 100 kDa | 1.28±0.09 | 0.01±0.04 | 0.26±0.01 | Negative |
| S17, 10 kDa | 1.8±0.2 | -0.02±0.04 | 0.22±0.01 | Negative |
| S18, 10 kDa | 1.5±0.2 | -0.01±0.05 | 0.24±0.01 | Negative |

*Table B-3: Electrical and X-ray characterization results for batch MW12.*

| Sample | μ ($cm^2 \cdot V^{-1}s^{-1}$) | $V_{Th}$ (V) | SS (V/dec) | Sensitivity ($\mu C \cdot Gy^{-1}cm^{-2}$) $\bullet 10^3$ |
|---|---|---|---|---|
| S1, encapsulated | 2.5±0.1 | 1.99±0.04 | 2.05±0.02 | 13±1 |
| S2, encapsulated | 2.52±0.05 | 1.5±0.1 | 1.6±0.1 | 14.7±0.6 |
| S3, encapsulated | 2.37±0.04 | 1.86±0.08 | 1.86±0.06 | 16.3±0.4 |
| S4, encapsulated | 1.81±0.07 | 1.7±0.1 | 1.7±0.1 | 10.0±0.3 |
| S5, no-encapsulated | 2.8±0.1 | 1.1±0.2 | 0.8±0.2 | 11.3±0.3 |
| S6, no-encapsulated | 2.43±0.07 | 1.0±0.1 | 0.7±0.1 | 2.4±0.2 |
| S7, no-encapsulated | 2.29±0.08 | 1.1±0.1 | 0.8±0.1 | Negative |
| S8, no-encapsulated | 2.76±0.07 | 1.4±0.4 | 0.6±0.1 | 5±3 |

*Table B-4: Electrical and X-ray characterization results for batch P7500.*

# Appendix C

In section 4.2 and 4.3, 5 dynamic responses of different devices have been shown and discussed. As I characterized three batches with three different PS molecular weights each, for a total of 9 distinct compositions, 4 of them have not been shown yet, since they do not provide additional contributions to this research work. The reason for this lies in the fact that the batch MW12 had negative sensitivities in both 100 kDa and 10 kDa molecular weights, so that just batch MW41 has relevant dynamic responses that have not been presented previously (for 100 kDa and 10 kDa molecular weights). These results are shown as follows.

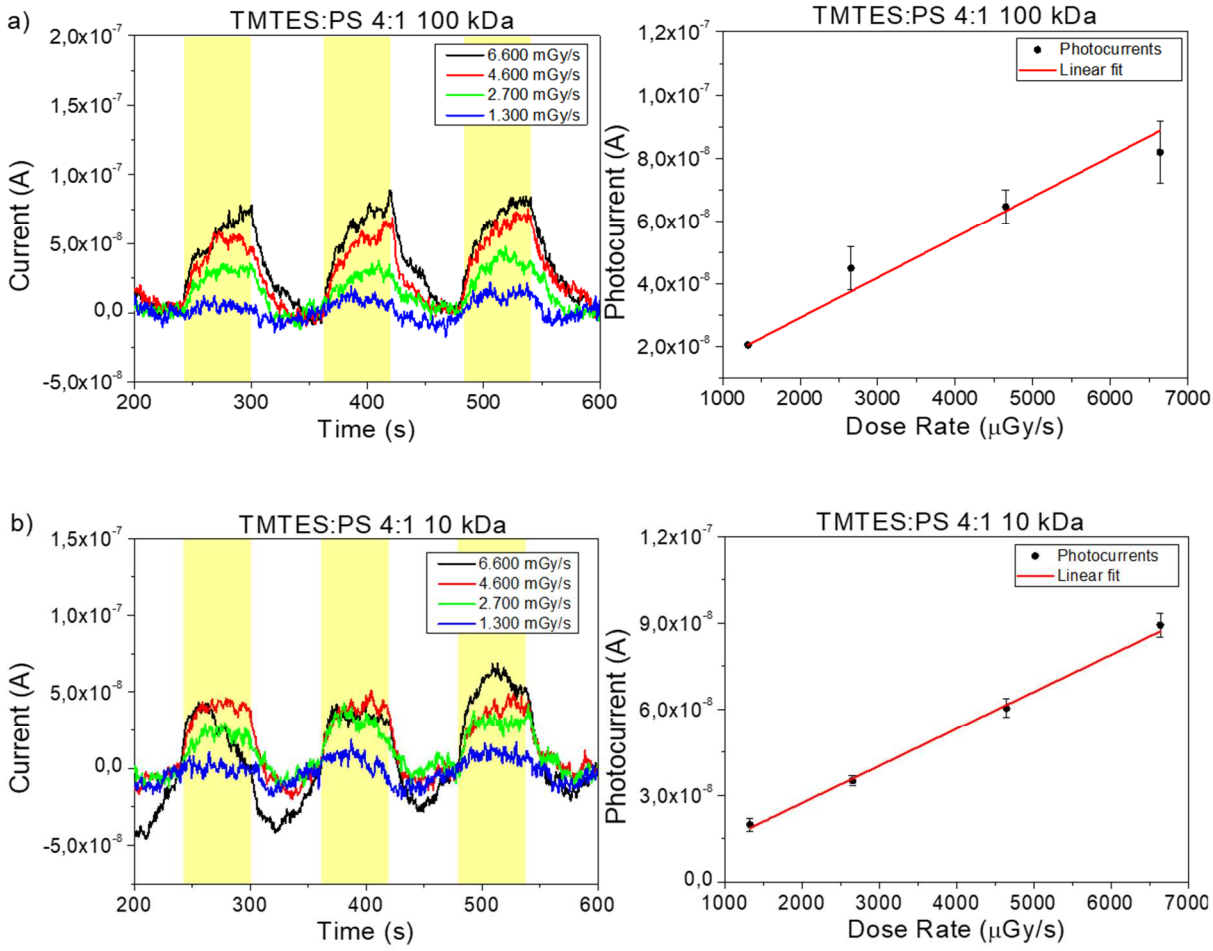


*Fig. C-1: a) 100 kDa and c) 10 kDa PS molecular weight dynamic responses and correspondent sensitivity calculations.*

# References


1. Basiricò, L., Ciavatti, A. & Fraboni, B. Solution-Grown Organic and Perovskite X-Ray Detectors: A New Paradigm for the Direct Detection of Ionizing Radiation. *Advanced Materials Technologies* vol. 6 Preprint at https://doi.org/10.1002/admt.202000475 (2021).

2. Singh, R. & Roy, S. C. Purnima Sinha and her Doctoral Work Under Professor S.N. Bose. *Sci Cult* **85**, 243 (2019).

3. Seibert, J. A. *X-ray imaging physics for nuclear medicine technologists. Part 1: Basic principles of x-ray production*. *Article in Journal of Nuclear Medicine Technology* http://www.snm.org/ce_online (2004).

4. Aquilanti, G., Vaccari, L., Plaisier, J. R. & Goldoni, A. Instrumentation at Synchrotron Radiation Beamlines. in *Synchrotron Radiation* 65–104 (Springer Berlin Heidelberg, 2015). doi:10.1007/978-3-642-55315-8_3.

5. https://www.slideserve.com/anka/synchrotron-radiation-light-sources.

6. Knoll, G. F. *Radiation detection and measurement*. (Wiley, 2000).

7. Jana, A. *et al.* Perovskite: Scintillators, direct detectors, and X-ray imagers. *Materials Today* **55**, 110–136 (2022).

8. Basiricò, L. *et al.* Direct X-ray photoconversion in flexible organic thin film devices operated below 1 v. *Nat Commun* **7**, (2016).

9. Mescher, H. *et al.* Flexible Inkjet-Printed Triple Cation Perovskite X-ray Detectors. *ACS Appl Mater Interfaces* **12**, 15774–15784 (2020).

10. Temiño, I. *et al.* Morphology and mobility as tools to control and unprecedentedly enhance X-ray sensitivity in organic thin-films. *Nat Commun* **11**, (2020).

11. Owens, A. & Peacock, A. Compound semiconductor radiation detectors. *Nucl Instrum Methods Phys Res A* **531**, 18–37 (2004).

12. Fink, J., Krüger, H., Lodomez, P. & Wermes, N. Characterization of charge collection in CdTe and CZT using the transient current technique. *Nucl Instrum Methods Phys Res A* **560**, 435–443 (2006).

13. Spahn, M. X-ray detectors in medical imaging. *Nucl Instrum Methods Phys Res A* **731**, 57–63 (2013).

14. Rao, C. N. R. Perovskites. in *Encyclopedia of Physical Science and Technology* 707–714 (Elsevier, 2003). doi:10.1016/B0-12-227410-5/00554-8.

15. Thirimanne, H. M. *et al.* High sensitivity organic inorganic hybrid X-ray detectors with direct transduction and broadband response. *Nat Commun* **9**, 2926 (2018).

16. Liu, J. *et al.* Flexible, Printable Soft-X-Ray Detectors Based on All-Inorganic Perovskite Quantum Dots. *Advanced Materials* **31**, (2019).

17. Schmidt-Mende, L. *et al.* Roadmap on organic–inorganic hybrid perovskite semiconductors and devices. *APL Mater* **9**, (2021).

18. Stoumpos, C. C. *et al.* Crystal Growth of the Perovskite Semiconductor $CsPbBr_3$ : A New Material for High-Energy Radiation Detection. *Cryst Growth Des* **13**, 2722–2727 (2013).

19. Yakunin, S. *et al.* Detection of X-ray photons by solution-processed lead halide perovskites. *Nat Photonics* **9**, 444–449 (2015).

20. Ciavatti, A. *et al.* Dynamics of direct X-ray detection processes in high-Z Bi2O3 nanoparticles-loaded PFO polymer-based diodes. *Appl Phys Lett* **111**, (2017).

21. Geffroy, B., le Roy, P. & Prat, C. Organic light-emitting diode (OLED) technology: materials, devices and display technologies. *Polym Int* **55**, 572–582 (2006).

22. Pagliaro, M., Ciriminna, R. & Palmisano, G. Flexible Solar Cells. *ChemSusChem* **1**, 880–891 (2008).

23. Lee, M. Y., Lee, H. R., Park, C. H., Han, S. G. & Oh, J. H. Organic Transistor-Based Chemical Sensors for Wearable Bioelectronics. *Acc Chem Res* **51**, 2829–2838 (2018).

24. Ciavatti, A. *et al.* Boosting Direct X-Ray Detection in Organic Thin Films by Small Molecules Tailoring. *Adv Funct Mater* **29**, (2019).

25. Fratelli, I. *et al.* Trap States Ruling Photoconductive Gain in Tissue-Equivalent, Printed Organic X-Ray Detectors. *Adv Mater Technol* (2022) doi:10.1002/admt.202200769.

26. Basirico, L. *et al.* Solid State Organic X-Ray Detectors Based on Rubrene Single Crystals. *IEEE Trans Nucl Sci* **62**, 1791–1797 (2015).

27. Ciavatti, A. *et al.* Toward Low-Voltage and Bendable X-Ray Direct Detectors Based on Organic Semiconducting Single Crystals. *Advanced Materials* **27**, 7213–7220 (2015).

28. Tamayo, A. *et al.* X-ray Detectors With Ultrahigh Sensitivity Employing High Performance Transistors Based on a Fully Organic Small Molecule Semiconductor/Polymer Blend Active Layer. *Adv Electron Mater* **8**, (2022).

29. Diao, Y., Shaw, L., Bao, Z. & Mannsfeld, S. C. B. Morphology control strategies for solution-processed organic semiconductor thin films. *Energy and Environmental Science* vol. 7 2145–2159 Preprint at https://doi.org/10.1039/c4ee00688g (2014).

30. Lamport, Z. A., Haneef, H. F., Anand, S., Waldrip, M. & Jurchescu, O. D. Tutorial: Organic field-effect transistors: Materials, structure and operation. *J Appl Phys* **124**, (2018).

31. Galindo, S., Tamayo, A., Leonardi, F. & Mas-Torrent, M. Control of Polymorphism and Morphology in Solution Sheared Organic Field-Effect Transistors. *Adv Funct Mater* **27**, (2017).

32. Kus, M. *et al.* Synthesis of Nanoparticles. in *Handbook of Nanomaterials for Industrial Applications* 392–429 (Elsevier, 2018). doi:10.1016/B978-0-12-813351-4.00025-0.

33. Pillonnet, G. & Martinez, T. Sub-threshold startup charge pump using depletion MOSFET for a low-voltage harvesting application. in *2015 IEEE Energy Conversion Congress and Exposition (ECCE)* 3143–3147 (IEEE, 2015). doi:10.1109/ECCE.2015.7310100.

34. https://www.electronicshub.org/mosfet/.

35. Wang, Y. *et al.* Encapsulation and Stability Testing of Perovskite Solar Cells for Real Life Applications. *ACS Materials Au* **2**, 215–236 (2022).

36. Kim, S. H. *et al.* Damage-free hybrid encapsulation of organic field-effect transistors to reduce environmental instability. *J Mater Chem* **22**, 7731 (2012).

37. Uddin, A., Upama, M., Yi, H. & Duan, L. Encapsulation of Organic and Perovskite Solar Cells: A Review. *Coatings* **9**, 65 (2019).

38. Shockley, W. A Unipolar 'Field-Effect' Transistor. *Proceedings of the IRE* **40**, 1365–1376 (1952).

39. Temiño, I. *et al.* A Rapid, Low-Cost, and Scalable Technique for Printing State-of-the-Art Organic Field-Effect Transistors. *Adv Mater Technol* **1**, (2016).

40. Paterson, A. F. *et al.* Recent Progress in High-Mobility Organic Transistors: A Reality Check. *Advanced Materials* **30**, (2018).

41. Un, H., Wang, J. & Pei, J. Recent Efforts in Understanding and Improving the Nonideal Behaviors of Organic Field-Effect Transistors. *Advanced Science* **6**, (2019).

42. Bittle, E. G., Basham, J. I., Jackson, T. N., Jurchescu, O. D. & Gundlach, D. J. Mobility overestimation due to gated contacts in organic field-effect transistors. *Nat Commun* **7**, 10908 (2016).

43. Uemura, T. *et al.* On the Extraction of Charge Carrier Mobility in High-Mobility Organic Transistors. *Advanced Materials* **28**, 151–155 (2016).

44. Egginger, M., Bauer, S., Schwödiauer, R., Neugebauer, H. & Sariciftci, N. S. Current versus gate voltage hysteresis in organic field effect transistors. *Monatshefte für Chemie - Chemical Monthly* **140**, 735–750 (2009).

45. Hwang, D. K., Oh, M. S., Hwang, J. M., Kim, J. H. & Im, S. Hysteresis mechanisms of pentacene thin-film transistors with polymer/oxide bilayer gate dielectrics. *Appl Phys Lett* **92**, (2008).

46. Iqbal, H. F. *et al.* Suppressing bias stress degradation in high performance solution processed organic transistors operating in air. *Nat Commun* **12**, 2352 (2021).

47. Boroumand, F. A. *et al.* Direct x-ray detection with conjugated polymer devices. *Appl Phys Lett* **91**, (2007).

48. Intaniwet, A. *et al.* Characterization of thick film poly(triarylamine) semiconductor diodes for direct x-ray detection. *J Appl Phys* **106**, (2009).

49. Intaniwet, A., Mills, C. A., Shkunov, M., Sellin, P. J. & Keddie, J. L. Heavy metallic oxide nanoparticles for enhanced sensitivity in semiconducting polymer x-ray detectors. *Nanotechnology* **23**, 235502 (2012).

50. Thirimanne, H. M. *et al.* High sensitivity organic inorganic hybrid X-ray detectors with direct transduction and broadband response. *Nat Commun* **9**, 2926 (2018).

51. Han, H. *et al.* Enhancement of X-ray detection by single-walled carbon nanotube enriched flexible polymer composite. *Nanoscale Res Lett* **9**, 610 (2014).

52. Fraboni, B., Ciavatti, A., Basiricò, L. & Fraleoni-Morgera, A. Organic semiconducting single crystals as solid-state sensors for ionizing radiation. *Faraday Discuss.* **174**, 219–234 (2014).

53. Lai, S. *et al.* A Highly Sensitive, Direct X-Ray Detector Based on a Low-Voltage Organic Field-Effect Transistor. *Adv Electron Mater* **3**, (2017).

54. Riera-Galindo, S., Leonardi, F., Pfattner, R. & Mas-Torrent, M. Organic Semiconductor/Polymer Blend Films for Organic Field-Effect Transistors. *Adv Mater Technol* **4**, (2019).

55. https://www.ossila.com/en-eu/products/tmtes-pentacene.

56. https://www.sigmaaldrich.com/IT/it/substance/polystyrene123459003536.

57. Tamayo, A. *et al.* Mobility anisotropy in the herringbone structure of asymmetric Ph-BTBT-10 in solution sheared thin film transistors. *J Mater Chem C Mater* **9**, 7186–7193 (2021).

58. Illig, S. *et al.* Reducing dynamic disorder in small-molecule organic semiconductors by suppressing large-amplitude thermal motions. *Nat Commun* **7**, 10736 (2016).

59. Zhao, K. *et al.* Vertical Phase Separation in Small Molecule:Polymer Blend Organic Thin Film Transistors Can Be Dynamically Controlled. *Adv Funct Mater* **26**, 1737–1746 (2016).

60. Rodger, D. C. *Development of Flexible Parylene-Based Microtechnologies for Retinal and Spinal Cord Stimulation and Recording*. (2008).

61. C., D., Li, W., D., J., S., M. & Tai, Y.-C. Flexible Circuit Technologies for Biomedical Applications. in *Advances in Micro/Nano Electromechanical Systems and Fabrication Technologies* (InTech, 2013). doi:10.5772/55308.

62. Chen, C.-L. *et al.* Mechanical and electrical evaluation of parylene-C encapsulated carbon nanotube networks on a flexible substrate. *Appl Phys Lett* **93**, (2008).

63. von Metzen, R. P. & Stieglitz, T. The effects of annealing on mechanical, chemical, and physical properties and structural stability of Parylene C. *Biomed Microdevices* **15**, 727–735 (2013).

64. Kim, M., Mackenzie, D. M. A., Kim, W., Isakov, K. & Lipsanen, H. All-parylene flexible wafer-scale graphene thin film transistor. *Appl Surf Sci* **551**, 149410 (2021).

65. Coelho, B. J. *et al.* Parylene C as a Multipurpose Material for Electronics and Microfluidics. *Polymers (Basel)* **15**, 2277 (2023).

66. Gorham, W. F. A New, General Synthetic Method for the Preparation of Linear Poly- *p* -xylylenes. *J Polym Sci A1* **4**, 3027–3039 (1966).

67. Chiriguayo, M. *B2900A Series Precision Source/Measure Unit*. www.keysight.com.

68. Welker, R. W. Size Analysis and Identification of Particles. in *Developments in Surface Contamination and Cleaning* 179–213 (Elsevier, 2012). doi:10.1016/B978-1-4377-7883-0.00004-3.

69. Benninghoven, A. Chemical Analysis of Inorganic and Organic Surfaces and Thin Films by Static Time-of-Flight Secondary Ion Mass Spectrometry (TOF-SIMS). *Angewandte Chemie International Edition in English* **33**, 1023–1043 (1994).